

AD-A159 202

STRUCTURAL RELIABILITY OF BRITTLE MATERIALS AT HIGH
TEMPERATURES. (U) NATIONAL BUREAU OF STANDARDS
GAITHERSBURG MD INORGANIC MATERI..

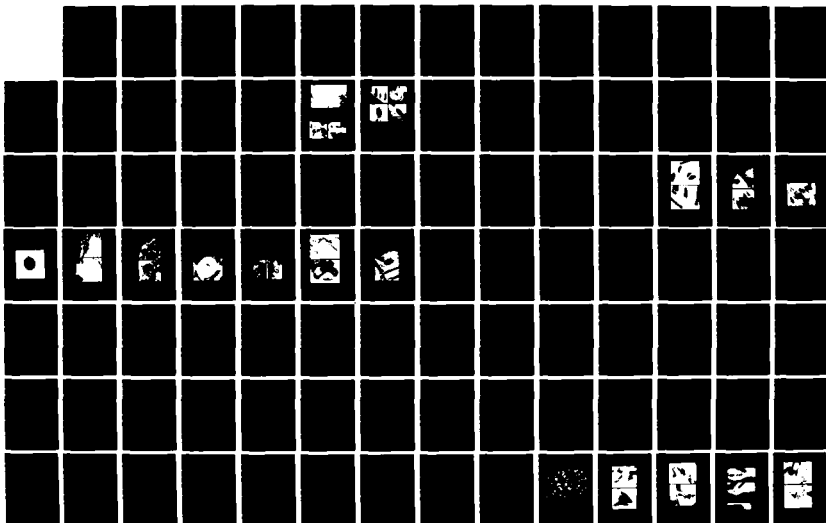
1/3

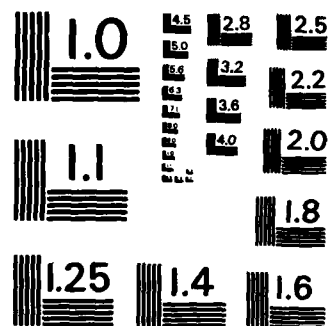
UNCLASSIFIED

S M WIEDERHORN ET AL. 31 DEC 84

F/G 15/7

NL





MICROCOPY RESOLUTION TEST CHART
NATIONAL BUREAU OF STANDARDS-1963-A

STRUCTURAL RELIABILITY OF BRITTLE MATERIALS AT HIGH TEMPERATURES

S. M. WIEDERHORN AND N. J. TIGHE

and

T.-J. CHUANG, K. A. HARDMAN-RHYNE, B. J. HOCKEY,
R. F. KRAUSE, JR., K. JAKUS, and Y. N. LU

TECHNICAL REPORT

AFOSR CONTRACT NO. AFOSR-ISSA-84-00013
NBS PROJECT NO. 4200464

for

AIR FORCE OFFICE OF SCIENTIFIC RESEARCH
WASHINGTON, DC 20322

by

INORGANIC MATERIALS DIVISION
NATIONAL BUREAU OF STANDARDS
GAITHERSBURG, MD 20899



Approved for public release/
distribution unlimited.

December 31, 1984

AD-A159 202

DTIC FILE COPY

UNCLASSIFIED

SECURITY CLASSIFICATION OF THIS PAGE

REPORT DOCUMENTATION PAGE

1a. REPORT SECURITY CLASSIFICATION UNCLASSIFIED		1b. RESTRICTIVE MARKINGS													
2a. SECURITY CLASSIFICATION AUTHORITY		3. DISTRIBUTION/AVAILABILITY OF REPORT Approved for public release; distribution unlimited.													
2b. DECLASSIFICATION/DOWNGRADING SCHEDULE															
4. PERFORMING ORGANIZATION REPORT NUMBER		5. MONITORING ORGANIZATION REPORT NUMBER AFOSR-TR- 85-0686													
6a. NAME OF PERFORMING ORGANIZATION National Bureau of Standards	6b. OFFICE SYMBOL (If applicable)	7a. NAME OF MONITORING ORGANIZATION Air Force Office of Scientific Research													
6c. ADDRESS (City, State and ZIP Code) Inorganic Materials Division Washington DC 20234		7b. ADDRESS (City, State and ZIP Code) Bldg 410 Bolling AFB DC 20332-6448													
8a. NAME OF FUNDING/SPONSORING ORGANIZATION AFOSR	8b. OFFICE SYMBOL (If applicable) NE	9. PROCUREMENT INSTRUMENT IDENTIFICATION NUMBER AFOSR-ISSA-84-00013													
8c. ADDRESS (City, State and ZIP Code) Bldg 410 Bolling AFB DC 20332-6448		10. SOURCE OF FUNDING NOS. <table border="1"><tr><td>PROGRAM ELEMENT NO.</td><td>PROJECT NO.</td><td>TASK NO.</td><td>WORK UNIT NO.</td></tr><tr><td>61102F</td><td>2306</td><td>A2</td><td></td></tr></table>		PROGRAM ELEMENT NO.	PROJECT NO.	TASK NO.	WORK UNIT NO.	61102F	2306	A2					
PROGRAM ELEMENT NO.	PROJECT NO.	TASK NO.	WORK UNIT NO.												
61102F	2306	A2													
11. TITLE (Include Security Classification) STRUCTURAL RELIABILITY OF BRITTLE MATERIALS AT HIGH TEMPERATURES															
12. PERSONAL AUTHOR(S) DR SHELDON M WIEDERHORN															
13a. TYPE OF REPORT ANNUAL	13b. TIME COVERED FROM 01 OCT 83 TO 30 SEP 84	14. DATE OF REPORT (Yr., Mo., Day) 84-12-31	15. PAGE COUNT 196												
16. SUPPLEMENTARY NOTATION															
17. COSATI CODES <table border="1"><tr><td>FIELD</td><td>GROUP</td><td>SUB. GR.</td></tr><tr><td></td><td></td><td></td></tr><tr><td></td><td></td><td></td></tr><tr><td></td><td></td><td></td></tr></table>		FIELD	GROUP	SUB. GR.										18. SUBJECT TERMS (Continue on reverse if necessary and identify by block number) yttria-doped hot pressed silicon nitride, alpha-silicon carbide, and a glass-bonded aluminum oxide.	
FIELD	GROUP	SUB. GR.													
19. ABSTRACT (Continue on reverse if necessary and identify by block number) See attached															
20. DISTRIBUTION/AVAILABILITY OF ABSTRACT UNCLASSIFIED/UNLIMITED <input checked="" type="checkbox"/> SAME AS RPT. <input type="checkbox"/> DTIC USERS <input type="checkbox"/>		21. ABSTRACT SECURITY CLASSIFICATION UNCLASSIFIED													
22a. NAME OF RESPONSIBLE INDIVIDUAL JOSEPH W HAGER, Maj, USAF		22b. TELEPHONE NUMBER (Include Area Code) (202) 767-4933	22c. OFFICE SYMBOL NE												

Work during the past year was conducted on yttria-doped hot-pressed silicon nitride, alpha-silicon carbide, and a glass-bonded aluminum oxide.(1) The first two materials were selected for study because of their potential for high temperature structural application, whereas the latter material was selected as a model material to investigate the creep-rupture behavior of two phase ceramics. During the past year our work emphasized the microstructural analysis of these materials and the effect of microstructure on component lifetime. A study has also been started on the effect of temperature on the strength of a commercial grade of partially stabilized zirconium oxide. The brief summary presented below gives our major findings on each of these materials. Full papers for each study are included in this report.

(1) In order to expand our effort on this project, portions of the work on these materials were co-sponsored by the Department of Energy.

Rept. Date verified per to them.

JC

A-1



STRUCTURAL RELIABILITY OF BRITTLE MATERIALS AT HIGH TEMPERATURES

	Page No.
Introduction.....	1
Motivation.....	1
Summary of Progress During the Past Year.....	4

Publications During the Past Year

Microstructural Analysis of Creep Failure in Si_3N_4 and SiC	11
Characteristic Cavity and Microcrack Distributions in $\alpha\text{-SiC}$, Si_3N_4 and ZrO_2	17
Creep and Fracture of Vitreous Bonded Aluminum Oxide.....	45
Estimation of Power-Law Creep Parameters from Bend Test Data..	101
Structural Reliability of Ceramic Materials.....	143

AIR FORCE OFFICE OF SCIENTIFIC RESEARCH (AFOSR)
NOTICE OF AWARD
This award was made possible by the generous support of the
Department of Defense.
MATTHEW J. ...
Chief, Technical Information Division

STRUCTURAL RELIABILITY OF BRITTLE MATERIALS AT HIGH TEMPERATURES

Introduction

This research is directed towards the development of engineering techniques to assess the performance and reliability of structural ceramics at high temperatures. Long term strength data is being collected on typical structural ceramics (i.e. Si_3N_4 , SiC , Al_2O_3), that have been exposed to thermal and mechanical loads at elevated temperatures. The importance of creep crack growth, cavitation and flaw generation to long term structural reliability is being assessed. Results are presented in terms of structural reliability maps which exhibit failure mechanisms in terms of time-dependent, probability density functions of strength. The importance of these structural reliability maps to engineering design will be demonstrated.

Motivation

Modern structural ceramics are intended for use in applications such as heat engines and heat exchangers, in which mechanical and thermal loading are expected to result in a gradual decay of the mechanical strength of these materials. A decay in strength also occurs as a result of exposure to hostile environments at elevated temperatures, which results in both localized and generalized chemical corrosion of ceramics. Although materials scientists and engineers are aware of the long term susceptibility of ceramic materials to strength degradation, the engineering techniques for addressing time-dependent strength degradation at elevated temperatures are limited. The approaches that are used to improve lifetime employ empirically developed safety factors, or fracture

mechanics based crack growth theories. Whereas both of these approaches are of value to the prediction of structural reliability, experience in high temperature heat engine programs indicates that more effective lifetime prediction techniques are needed to assure the structural reliability of ceramics in modern applications.

Over the past three years, a new approach has been taken to the structural design of ceramic materials at elevated temperatures. The approach stresses probabilistic aspects of fracture by providing a description of the time evolution of strength in statistical terms. The method provides a way of collecting and presenting strength data in terms of the time evolution of the probability density function for strength. Since the method incorporates the theory of fracture mechanics into its structure, it is consistent with the earlier fracture mechanics based theories of structural reliability. The main output of the method is a diagram that illustrates strength behavior of a material as a function of time. This type of diagram is of value to the designer because it not only represents the strength as a function of time, but also illustrates the degradation processes that occur at any point in time. These diagrams can be used as a simple map of environmental-stress conditions to be avoided by the engineer in designing structural ceramics.

To date, diagrams of this type have been obtained for two grades of hot-pressed silicon nitride and one grade of silicon carbide. An example of one of these diagrams is shown in figure 1 for α -SiC. At applied stresses that lie below the apparent threshold for strength degradation, specimens become stronger with time, eventually increasing their strength by approximately 30 percent as a consequence of high temperature exposure. At applied stresses that lie above the threshold, failure occurs after a

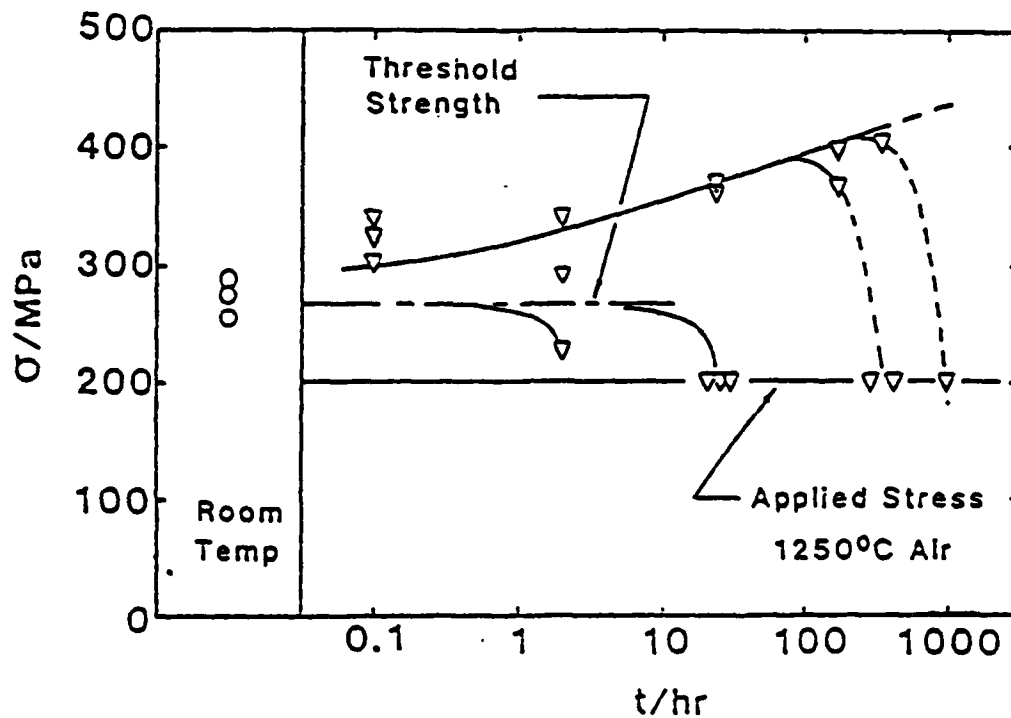


Fig. 1. Strength of a sintered alpha silicon carbide as a function of time for an applied flexural stress of 200 MPa. Test temperature of 1250°C.

period of time. To fully understand the type of mechanical behavior shown in figure 1, it is necessary to explore the microstructure of the material and to determine how microstructure affects the mechanical behavior of the material as a function of time at temperature. Once this has been accomplished, mechanisms of strength degradation can be determined and used to label the reliability diagram, as has been done for hot pressed silicon nitride. Thus, mechanical testing and microstructural analysis must be done in tandem in order to fully elucidate the mechanical behavior of structural ceramics at elevated temperatures.

The primary objective of this project is to develop reliability diagrams for typical structural ceramics (i.e. Si_3N_4 , SiC , Al_2O_3 , ZrO_2). The dependence of these diagrams on temperature and applied stress will be explored, and the various regions of behavior on each diagram will be elucidated by microstructural analysis. Finally, in order to extrapolate from one temperature and applied stress to another, a theoretical basis for these diagrams will have to be developed, paying particular attention to the various regions of strength degradation on these diagrams, and to the boundaries between the regions.

Summary of Progress During the Past Year

Work during the past year was conducted on yttria-doped hot-pressed silicon nitride, α -silicon carbide, and a glass-bonded aluminum oxide.¹ The first two materials were selected for study because of their potential for high temperature structural application, whereas the latter material was selected as a model material to investigate the creep-rupture behavior

¹In order to expand our effort on this project, portions of the work on these materials were co-sponsored by the Department of Energy.

of two phase ceramics. During the past year our work emphasized the microstructural analysis of these materials and the effect of microstructure on component lifetime. A study has also been started on the effect of temperature on the strength of a commercial grade of partially stabilized zirconium oxide. The brief summary presented below gives our major findings on each of these materials. Full papers for each study are included in this report.

Microstructural Analysis of α -SiC, Si_3N_4 , and ZrO_2

Results of a study on the effect of microstructure on the mechanical behavior of structural ceramics are summarized in the first two papers of this report. The first paper, "Characteristic Cavity and Microcrack Distributions in α -SiC, Si_3N_4 and ZrO_2 ", by N. J. Tighe, K. A. Hardman-Rhyne of the National Bureau of Standards and Y. N. Lu of the Shanghai Institute of Testing Technology, explores the application of transmission electron microscopy and small angle neutron scattering as methods of observing microcracks and cavities in ceramics. Electron microscopy is used to identify defects in terms of size, chemical composition, crystallographic structure, morphology, and orientation. Small angle neutron scattering is used to classify scattering centers by size distribution for particle sizes from 2 to 100 nm. These of microstructural characterizations are used to identify the active flaw populations that result in strength degradation.

Studies on microstructural analysis an α -SiC suggest that microcracks occur in fibrous carbon inclusions that are originally present in the material as a result of processing. These inclusions are substantial in

size and may be the source of early failure in α -SiC. Long term annealing which tends to modify these inclusions may be one factor in accounting for the improvement in the strength after exposure at elevated temperature.

Microstructural analysis of ceramic specimens that were subjected to creep for extended periods are discussed in the above paper and in the second paper "Microstructural analysis of creep Failure in Si_3N_4 and SiC," by N. J. Tighe included in this report. It is shown that cavitation in two grades of hot-pressed silicon nitride (NC 132 and NCX 34) occurs by grain boundary slip at elevated temperatures. The yttria-doped silicon nitride is more resistant to high temperature slip than the magnesium-oxide doped material because a more refractory intergranular crystalline phase has replaced the glass at the grain boundaries. Nevertheless, crack formation occurs at a temperature of approximately 50 to 100°C higher in the yttria doped material. The mechanism of creep rupture in the yttria doped material results from bulk diffusion and the growth of lenticular cracks in the manner first described by Chuang and Rice. In the α -SiC, the graphitic inclusions discussed above were a source of dislocation activity, which eventually resulted in failure as a consequence of microstructural deformation. The failure mechanism is similar to that suggested by Petch in his classic mechanism of deformation fracture. This mechanism of microcrack generation and crack growth is believed to be the cause of the time dependent failure observed for the α -SiC after long periods of exposure under load at elevated temperatures.

Creep and Creep Fracture of Vitreous Bonded Aluminum Oxide

Glass-bonded aluminum oxide made by the Coors Co. (AD-96) was selected as a model material to study the creep and creep rupture behavior of two-phase ceramic materials. Because most ceramic materials under consideration for heat engine materials are in fact two-phase materials, it was considered important to select a relatively simple material whose chemistry was understood and whose microstructure could be easily controlled so that the parameters that determine two phase deformation and fracture could be studied. Aluminum oxide-glass composites were selected for study because: (1) they are relatively well understood from a thermodynamic point of view; (2) they are chemically stable so that oxidation can be eliminated as an important factor in our investigation; and (3) glass-aluminum oxide composites are easy to manufacture, or can be purchased as more or less standard commercial materials.

The third paper of this report, "Creep and Fracture of Vitreous Bonded Aluminum Oxide," by S. M. Wiederhorn, B. J. Hockey and R. F. Krause, Jr. of the National Bureau of Standards and K. Jakus of the University of Massachusetts, summarizes much of the work conducted during the past year on vitreous bonded aluminum oxide. The most significant observation of the study was the occurrence of a stress driven devitrification along the cross-section of the bend specimens. The compressive portion of the specimens were similar to the annealed portion of the specimens in both composition and in microstructure. By contrast, the tensile section contained a highly devitrified glass phase along the grain boundaries. Based on the glass composition alone, the viscosity of the tensile side of the specimen is predicted to be three times that of the compressive side of the specimen. Extensive devitrification of the

glass in the grain boundaries should further increase the effective viscosity of the tensile side of the specimens. This finding of a stress-driven compositional change within ceramics has important implications both with regard to structural design and standard tests for property measurements.

Our studies of the deformation of glass bonded ceramic materials at elevated temperatures indicates a need for relating creep data to the state of stress in the component that is being deformed. Relations between different types of loading are needed because creep deformation in real structural materials at elevated temperatures is likely to be complex and to consist of mixed loading states. Furthermore, as creep occurs, the state of stress gradually changes as a function of time, depending on the nature of the creep. To fully utilize the techniques of lifetime prediction that are being developed, the importance of state-of-stress to the creep behavior must be analyzed.

The fourth paper of this report, "Estimation of Power-Law Creep parameters from Bend test Data," by Tze-jer Chuang, deals with the relationship between bending, tensile and compressive creep data. Governing equations are derived for the location of the neutral axis of a beam under bending stresses. In this treatment, the neutral axis does not necessarily pass through the centroid of the cross section. The creep response is expressed in terms of both the curvature rate and the load-point displacement rate, which are functions of the applied moment and the power-law creep parameters obtained from both tensile and compressive creep experiments. The results show that the conventional

method overestimates the creep rate in compression, and underestimates the creep rate in tension by at least two orders of magnitude, indicating the need for using the more accurate analysis presented in the above paper.

Review Paper on Techniques of Structural Reliability

The fifth paper in this report was given as an invited paper at the conference, "Ceramics, Jerusalem '84," held December, 16-20, 1984 in Jerusalem, Israel. The paper has been accepted by the Journal for Materials Science and Engineering, and will be published in the March issue of that Journal. Entitled "Structural Reliability of Ceramic Materials," and authored by S. M. Wiederhorn and E. R. Fuller, Jr., the paper reviews the effect of material properties on the structural reliability of ceramics at both low and elevated temperatures. At low temperatures, the paper concludes that reliability can be based on flaw statistics and characterization of rates of flaw growth. Most of these methods are well developed and have been used for a number of years to assure the reliability of ceramics in structural applications. By contrast, methods of assessing reliability are not as well developed for high temperature applications, especially at low levels of applied load, failure occurs by creep rupture. Because failure by creep rupture is not yet well characterized theoretically, lifetimes are given only in terms of parametric representations of the controlling variables.

MICROSTRUCTURAL ANALYSIS OF CREEP FAILURE IN Si_3N_4 AND SiC

N.J. Tighe
National Bureau of Standards
Gaithersburg, MD 20899

05
PREVIOUS PAGE
IS BLANK

(THIS PAGE IS BLANK)

Failure Analysis in Polymers, Ceramics, and Composites

MICROSTRUCTURAL ANALYSIS OF CREEP FAILURE IN Si_3N_4 AND SiC

N. J. Tighe

Advanced ceramics such as silicon nitride and silicon carbide are being used in high-temperature, high-stress heat-engine applications where catastrophic failure must be avoided. It is necessary to develop the required design parameters and to predict lifetimes for these materials. Therefore extensive fracture mechanics studies are being carried out and the failure mechanisms are being identified in terms of the appropriate thermal and mechanical stress environments.^{1,2} Identification of the microstructural elements that cause failure is being carried out by analytical scanning transmission electron microscopy (STEM). Silicon carbide and silicon nitride fail by mechanisms that involve crack propagation from pre-existing flaws or from flaws that develop during the exposure to a simulated service environment. The pre-existing flaw population consists of inclusions, pores, and surface preparation damage; the flaw population that develops during exposure includes cavities, oxidation pits, microcracks, and reaction products from bonding phases and inclusions. Silicon nitride and silicon carbide are compounds of several crystalline and amorphous phases and the identification of the microstructural elements that relate to the failure mechanisms requires considerable structural and chemical analysis. Examination of fracture interfaces by light microscopy and by scanning electron microscopy can locate the fracture initiation site and show the path of the crack across the interface. In order to identify the specific flaw population that is responsible for the failure, the higher resolution analytical capabilities of the STEM are used to examine the test specimens. The effectiveness of the STEM techniques for failure analysis is demonstrated with examples from recent fracture mechanics test programs.

Experimental

The microstructural elements that affect failure during long-term exposure experiments on silicon nitride and silicon carbide are: (a) amorphous or crystalline bonding phases, (b) inclusions and pores within grains and at triple junctions, and (c) cracks and defects introduced by surface grinding. Static load experiments were done with four-point bend bars at temperatures up to 1500 C for times up to 1000 h. Specimens fail by premature fracture as a result of crack growth or by excessive bending as a result of creep. The experiments were used to develop reliability maps that show the stress-time evolution of strength. Specimens were broken at temperature during the course of the experiments in order to obtain strength distributions at specific time intervals for the reliability assessment. The microstructural elements that were related to strength changes and to failures were identified from specimens selected from specific regions of the reliability maps.

Specimens for the STEM examination were prepared by slicing of sections from cross sections and from tensile and compressive sides of the test bars with a diamond saw. The sections were ground to approximately 100 μm -thick slices, and 3mm disks were cut and ion thinned to electron transparency. The ion thinning was carried out from one or both sides, depending on the information required from the specimen. The relatively thick slices were used in order to eliminate confusion between damage associated with specimen preparation and damage associated with the deformation from the static load tests. The oxide scale was removed from the tensile and compressive surfaces by careful polishing or by ion sputtering. Silicon nitride foils were coated with carbon to prevent charging but the coating was not needed on

The author is at the National Bureau of Standards, Washington, DC 20234. The work was supported in part by the U.S. Air Force Office of Scientific Research and by the U.S. Army Materials and Mechanics Research Center under contract DOE-1A-DE-A101-77-CS5-1017.

silicon carbide foils. The micrographs in Fig. 1 are examples of crack growth information that was obtained from surface and subsurface examination. The specimen is a hot pressed silicon nitride that showed creep cracking at 1400 C. The conventional TEM³ showed extensive grain boundary separation and oxide along grain boundary interfaces that is characteristic of grain boundary sliding mechanism of creep. Examination of the surface with secondary electrons in an STEM showed the path of primary crack from the thinned region to edge of the disk and the arrays of smaller cracks and cavities associated with creep. The amorphous phase softened at the test temperature and was pulled across the crack from between the grain boundaries as the specimen bent. The tungsten inclusions contained in the specimen were identified and then associated with cavities and surface pits by imaging with the back-scattered electrons. The amorphous phase was shown to be a magnesium silicate glass⁴ by element analysis with the use of EDS and EELS and diffraction analysis. Such a comprehensive analysis of a single specimen demonstrates the approach used for failure analysis.

The micrographs in Fig. 2 are examples of the identification of the nucleation and growth of cavities during creep of yttria-doped silicon nitride.⁵ This ceramic has a crystalline yttrium silicate bonding phase rather than an amorphous phase as in the previous example. The extent of the cavitation decreased with distance from the tensile surface to the neutral axis and these changes were revealed when serial sections were made. The progression in Fig. 2 shows the extensive grain-boundary cracks at the tensile surface, the nucleation and growth stage a few micrometers below the tensile surface, and the initial diffusion growth of the yttria phase into a crack-like configuration. Diffraction analysis shows the changing yttria phase.

The flaw population responsible for the changes in strength and failures in alpha silicon carbide and static load experiments is identified in the examples shown in Fig. 3. The as-sintered silicon carbide was found to have graphitic inclusions at triple junctions and within grains. These graphitic inclusions had a fibrous texture from which elliptical diffraction patterns could be formed. The inclusions were well bonded to the silicon carbide grains and had an amorphous background with Si and Ca present. The carbon was identified by EELS. There was considerable microcracking near grain boundaries and along faults in the silicon carbide. Boron was found by small-angle neutron scattering (SANS) and by EELS analysis. The microcracks were not found in annealed samples. In samples from the static load experiments the microscopy analysis showed that the graphitic inclusions caused several reactions. At the surface, they oxidized and produced cavities. Below the tensile surface they interacted with the stress field around them and caused cracks within grains and some dislocation activity. The presence of the graphitic inclusions in the alpha silicon carbide had not been anticipated or identified from regular SEM analysis. The complete analytical capabilities of the STEM were required to identify the inclusions and to indicate their role in the strength degradation and failure process.

Conclusions

The results of the STEM analysis of silicon nitride and silicon carbide provided the information on failure mechanisms that was required to predict lifetimes from fracture mechanics tests carried out in high-temperature, high-stress conditions.

References

1. N. J. Tighe and S. M. Wiederhorn, "Effects of oxidation on the reliability of silicon nitride," in R. C. Bradt et al., Eds., *Fracture Mechanics of Ceramics*, New York: Plenum, 1983, 403-423.
2. S. M. Wiederhorn and N. J. Tighe, "Structural reliability of yttria-doped hot-pressed silicon nitride at elevated temperatures," *J. Amer. Ceram. Soc.* 66: 884-889, 1983.
3. N. J. Tighe, "The structure of slow-crack interfaces in silicon nitride," *J. Mat. Sci.* 13: 1781-1786, 1978.
4. D. R. Clarke, "Grain boundary phases in a hot-pressed MgO fluxed silicon nitride," *J. Amer. Ceram. Soc.* 60: 491-495, 1977.
5. N. J. Tighe, S. M. Wiederhorn, T.-J. Chuang, and C. L. McDaniel, "Creep cavitation and crack growth in silicon nitride," in R. Tressler, Ed., *Plastic Deformation of Ceramics*, in press.

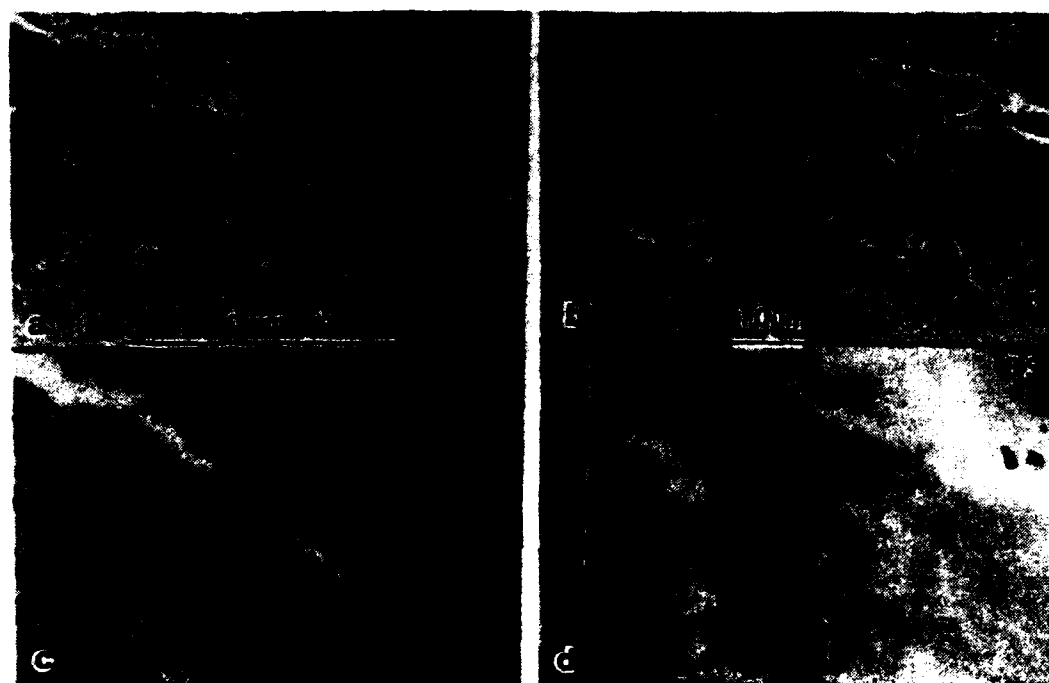


FIG. 1.--Microstructural characteristics of creep in specimen tested at 1400 C in air: (a) and (b) secondary-electron images of primary crack; (c) backscattered electron image of tungsten and iron based particles as dark images.



FIG. 2.--Microstructural characteristics of creep cavitation in yttria-doped silicon nitride after 117 h at 1300 C with 350 MPa load: (a) cavitation along grain boundaries approximately 5 μm beneath tensile surface; (b) crack-like diffusional zone and grain boundary crack approximately 30 μm beneath tensile surface.

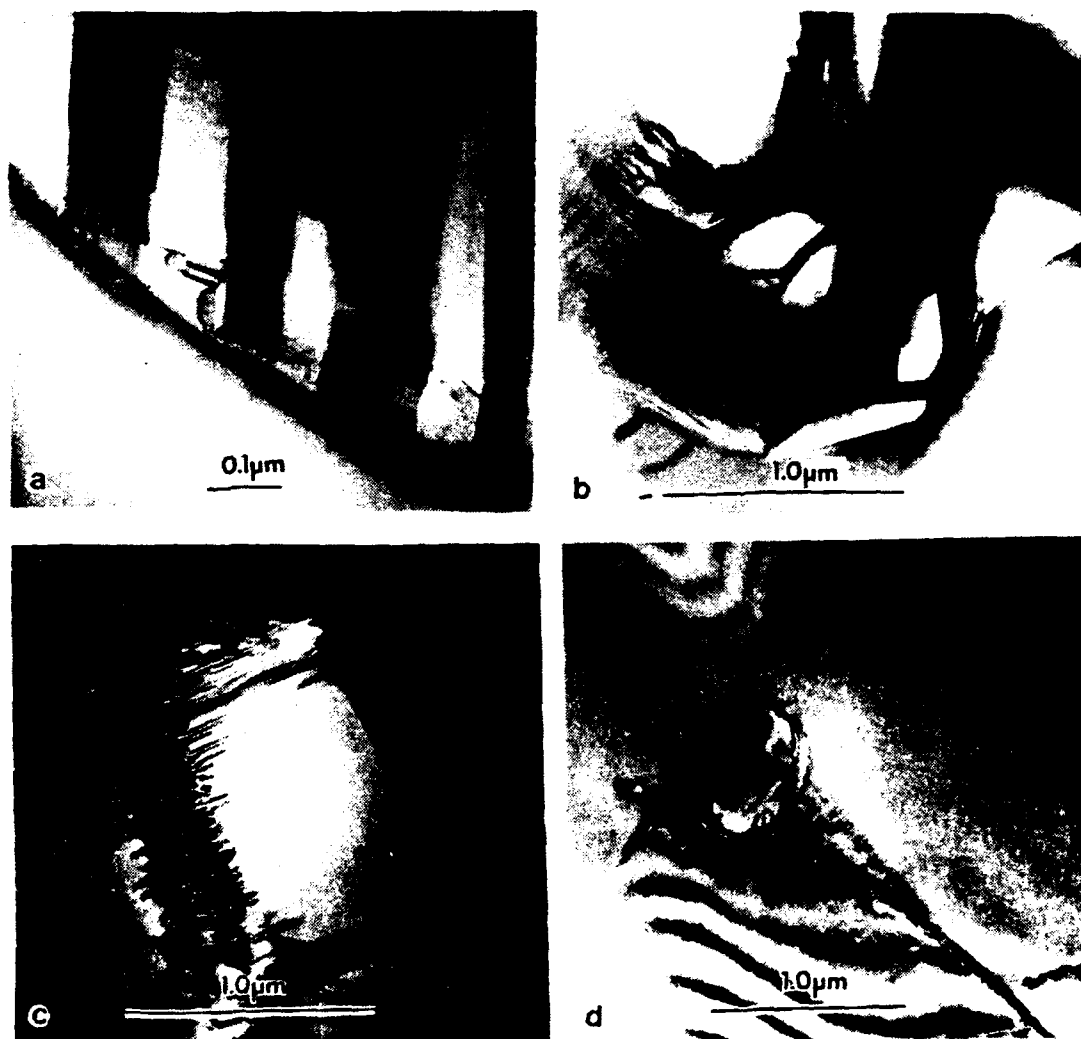


FIG. 5.--Microstructural elements in silicon carbide: (a) microcracks near grain boundary in as-sintered sample; (b) fibrous graphitic phase in as-received sample; (c) faults and initial grinding damage near tensile surface of specimen after 300 h at 1300 C; (d) crack associated with graphitic inclusion in 300h specimen.

CHARACTERISTIC CAVITY AND MICROCRACK DISTRIBUTIONS IN
α SiC, Si₃N₄ AND ZrO₂

N.J. Tighe, K.A. Hardman-Rhyne
National Bureau of Standards
Gaithersburg, MD 20899

and

Y.N. Lu
Shanghai Institute of Testing Technology
Shanghai, China

(THIS PAGE IS BLANK)

CHARACTERISTIC CAVITY AND MICROCRACK DISTRIBUTIONS IN
 α SiC, Si₃N₄ and ZrO₂

N. J. Tighe, K. A. Hardman-Rhyne

NATIONAL BUREAU OF STANDARDS
GAITHERSBURG, MARYLAND 20899

and

Y. N. Lu

SHANGHAI INSTITUTE OF TESTING TECHNOLOGY
SHANGHAI, CHINA

Cavities and microcracks comprise important failure related microstructural elements of the flaw population in advanced high temperature ceramics. These flaws are present in the as-processed materials and are produced also during high temperature exposures under various stress conditions. Porosity of itself does not necessarily cause weakening in a specific ceramic. In fact, the existence of microcracks has been related to toughening mechanisms in ceramics such as zirconia [1,2] and alumina-zirconia [2]. There is a certain vagueness to the terms "cavities and microcracks" and visualization of the exact flaw configurations must be made before empirical calculations for failure and lifetime predictions that are based on this type of flaw population can be validated completely. In the specific case of crack-like cavities produced by diffusional processes there is some agreement between the experimental observations and the theoretical calculations [3]. The purpose of this paper is to present results of scanning transmission electron microscopy (STEM) and small angle neutron scattering (SANS) as methods of observing microcracks and cavities and determining their spacial distribution. The electron microscopy techniques identify defects in terms of size, chemical composition, crystallographic structure,

morphology, and orientation. The small angle neutron scattering technique can scan a bulk sample in order to classify scattering centers by size distribution with particle sizes from 2 to 100 nm. The microstructural characterization is necessary in order to identify the active flaw population and to develop nondestructive evaluation procedures.

In this paper examples demonstrating the application of the techniques are taken from work on SiC, Si₃N₄ and ZrO₂. The specimens were chosen from sets of silicon nitride and silicon carbide samples that had been tested at high temperature under static load conditions or under thermal cycling conditions to obtain mechanical property data for various heat engine programs. The zirconia samples were chosen from samples that were ready for mechanical testing in the NBS laboratory. The SiC and Si₃N₄ test bars were examined first by SANS and then sectioned for examination by electron microscopy. This procedure was followed in order to ensure that the same flaw population was observed with the two techniques. The zirconia bars were examined only by electron microscopy. Thin foils were made for electron microscopy by mechanical thinning followed by ion sputtering. Several foils were made from each test bar in order to probe the flaw distribution throughout the sample.

Experimental Procedures

The small angle neutron diffraction instrument at NBS has been described in detail [4] and a short description of experimental procedures is presented here in order to acquaint the reader with the methodology. Figure 1 is a diagram of the major features of the instrument. The neutron source is the 20 MW NBS research reactor. The neutron wavelength λ , can be varied from 0.4 to 1.5 nm by selecting the appropriate speed of

a rotating helical-channel velocity selector. The longer wavelengths ($> 1 \mu\text{m}$) are useful in diffraction measurements where larger size ($> 0.5 \text{ nm}$) particles or voids are being examined and where multiple Bragg scattering from the crystal structure of the material is to be avoided.

There are two types of collimating apertures which define the beam direction and divergence. One type consists of a pair of cadmium pin hole irises, one after the velocity selector and another before the sample. The other collimation system is designed for higher resolution measurements and consists of a set of channels in cadmium masks which effectively converge the neutron beam to a point at the center of the detector. The multiple sample chamber is computer controlled, and can be used under vacuum. Single samples can be studied as a function of temperature from below 4K to 1600K. Sample sizes are usually 1.0 to 2.5 cm are detected on a 64 cm x 64 cm position-sensitive proportional counter divided into 128 columns and 128 rows with a spatial resolution of 8 mm in each direction. The angle between the incident beam and the scattered beam is the scattering angle ϵ . The magnitude of the scattering vector Q in the small angle limit is $Q = k\epsilon$, where $k = 2\pi/\lambda$.

Diffraction experiments probe for microstructural phenomena in the range of 1 to 100 nm. For this case the SANS detector is usually centered directly in the incident beam. To minimize multiple scattering events the sample thickness is usually kept in the 2 to 6 mm range. It is also desirable to use materials with a minimum of incoherent scattering and absorption. An example of single particle diffraction is shown in Fig. 2. Since the constant scattering intensity contours are generally circular, the intensity data can be circularly averaged and plotted as a function of

the scattering vector, Q (see the right side of Fig. 2). The small- Q range of the data is generally called the Guinier region, and the large- Q data are called the Porod region. The shape of the scattering curve is wavelength independent when single particle scattering is dominant.

The electron microscopy was carried out using a scanning transmission electron microscope equipped with a non-dispersive X-ray detector, an electron energy loss spectrometer, a secondary electron detector and a back scattered electron detector. With this high resolution analytical electron microscope the surface and subsurface structures were imaged and the morphology, structure, and composition of the sample areas were determined.

Materials

Hot pressed silicon nitride samples were obtained from two sources: (a) tensile specimens from tests of Govila [5]; (b) four point bend specimens from tests at NBS [6]. The tensile specimens had a dog-bone shape and were six inches long with a one inch wide grip area and a 1/8 inch square reduced cross-section. The specimen was tested at 1204°C with a constant loading rate and it fractured after 21 hours at an applied stress of 132.5 MPa. The test terminated in the primary creep regime by brittle fracture. The wide portion of the specimen was used for the initial SANS experiment; and a thin section was made from the reduced cross-section. In order to identify the cavities and microcracks that resulted from creep, thin foils were made from some of the NBS specimens [6] that had been held under constant load for up to 1000 hours at temperatures up to 1400 °C.

The sintered alpha silicon carbide [7] samples used for this program were obtained from two sources: (a) a set of bars from thermal cycling tests that lasted 3500 hours during which the bars were cycled from 25 °C to 1370 °C [8]; and (b) bars that were used to obtain interrupted static load data [9].

The zirconia samples were partially stabilized by additions of magnesia [10]. Samples from the as-ground bars and from bars annealed for 100 hours at 1000 °C were examined by scanning and transmission electron microscopy [11].

Microstructural elements that contribute to reliable structural ceramics were identified by comparing microstructures in both as-received and exposed ceramics. It is well known for example that artifacts can be introduced during preparation of the specimens. Therefore, strain induced defects that occur during the grinding must be identified and distinguished from the strain induced defects that result from the deformation and exposure experiments. Sections were made from different areas of the four-point bend bars: from the fracture face, from the outer and inner portions of the compression and tension sides and from the cross-section through the test bars. Surfaces were examined in the as-reacted condition; and, for certain samples some of the oxide scale was removed by ion bombardment. The effects of polishing the surfaces and grinding the surfaces on phase transformations in the zirconia samples was assessed by examining the samples in the TEM as well as by X-ray powder diffraction. The zirconia samples were particularly difficult to prepare because the strain induced transformation in the tetragonal phase caused severe buckling of the thin foil sample and loss of thinned area. In

order to prevent excessive buckling, discs at least 100 μm were used and some of the ground or polished surface was removed by ion thinning. Samples as thin as 50 μm were curved and were not usable.

Experimental Results

Silicon Carbide

The as-sintered α SiC examined in the present experiments were polycrystalline compacts of 4H and 6H polytype SiC grains with carbon and boron inclusions. We found that the carbon phase existed as fibers in the open triple junctions and as particles within grains. The faults that are characteristic of the different polytypes and are parallel to the basal plane. Examples of these faults will be seen in many of the micrographs in this paper.

Four of the α SiC samples from the thermal cycling experiments were examined with small angle neutron scattering techniques and their designations are listed as follows:

SiC-1 α SiC base material as-received

SiC-2 α SiC exposed to 2200 $^{\circ}\text{F}$ for 1050 hours

SiC-3 α SiC held at 2500 $^{\circ}\text{F}$ for 1050 hours

SiC-4 α SiC held at 2500 $^{\circ}\text{F}$ for 3500 hours

In all four cases the neutron scattering was isotropic and the data were circularly averaged. This averaged intensity is plotted as a function of Q in figure 3. The difference in the intensities for SiC-1 in the

figure results from data that were collected for two different time periods. The error bars are drawn or are smaller than the symbols. Little difference is seen in the scattering curves of SiC-2 and SiC-3 suggesting that the cyclic heating between room temperature and 2200 °F had little effect on the population of neutron scatters. The data are analyzed by subtracting the intensities of the heat treated samples from the base sample SiC-1 to obtain an I_{diff} where:

$$I_{diff}(Q) = I_{SiC}(Q) - I_{healed}(Q)$$

Mathematical fits of the wave equations to the data were made using both spheres and randomly oriented thin disk models [12]. An example of the fit is shown in figure 3c where the I_{diff} data for SiC-1 to SiC-3 at $\lambda = 0.75$ nm is shown as squares and the Guinier model fit is shown as a solid line. The error bars are given or are less than the size of the symbol used.

It is clear from the plots that the baseline α SiC sample has a higher intensity than the other samples. This intensity reflects the presence of microcracks and cavities as the source of the increase in neutron scattering of SiC-1. Estimates of the microcrack size and density were made from the fit of these experimental points to the neutron scattering equations.

The as-received material (SiC-1) was found to contain a high volume of penny shaped microcracks approximately 21 nm diameter. The exposed SiC-2 showed a low density of this sized microcracks. Thus the thermal shock environment apparently healed the original microcracks and did not introduce additional cracks of the same size. This finding was contrary

to expectations but was confirmed by examination of the samples in the scanning transmission electron microscope. It is assumed that the α SiC grains remain the same throughout the heat treatments although the boron and phosphorous inclusions can react at high temperatures. Such changes would be averaged in the SANS data. At present there is no way to separate the effects on neutron scattering of the microcracks, cavities, and inclusions that are found in the silicon carbide samples.

The graphite inclusions that are shown in the electron micrographs of figure 4 had not been identified previously as inclusions in alpha silicon carbide. These graphite inclusions occur throughout the samples and have two forms: fiber bundles that fill the triple junction pores (figure 4A), and grains with oriented fiber compacts within the silicon carbide matrix (figure 4B). The fiber bundles are similar to the polyacrylonitrile-based carbon fibers that are stress graphitized at temperatures up to 2800 °C [13-15].

Thus the thin foil examination showed that the arrays of microcracks are present in the graphite inclusions rather than in the silicon carbide grains and confirmed the SANS observations. The microcracks are seen near the C-SiC interfaces and along the fiber bundles in the compact grains. There are pores and cavities within the random fiber bundles as shown in figure 4B. From the electron diffraction patterns taken of the graphite fibers it was found that the fiber axes are usually normal to the $\langle 0001 \rangle$ as found in the simple carbon fibers. The carbon fiber bundles are randomly oriented within the sample (figure 4C) and as such may act as fiber composite elements. The role of the carbon fibers with regard to strength and toughness is being assessed using interrupted static load tests [9].

The decrease in microcracking that was found in the small angle neutron scattering experiments could be accounted for by healing of the cracks in the graphite inclusions and by enlargement of the micropores that are present in carbon fibers in triple junctions as a result of oxidation of the carbon fibers during. The triple junctions shown in figure 5A are near a surface and show some remnant fiber structure and a film of amorphous oxide. Figure 5B shows a healed microcrack that extends from the grain boundary into the silicon carbide grain.

The boron in the silicon carbide specimens was identified from neutron activation analysis [16]. The presence of boron in the samples was confirmed using the electron energy loss spectrometer on the scanning transmission electron microscope. However, there was insufficient resolution to quantify the amounts. The boron may be resident in the carbon fiber areas.

Silicon Nitride

Transmission electron microscope examination of the magnesia and the yttria-doped hot-pressed silicon nitride samples showed that particles of tungsten carbide and iron are distributed throughout the material as illustrated in figure 6 [6]. These impurities are derived from the tungsten carbide grinding balls that are used during powder processing of the raw materials. Their presence is well-documented, and, although they do not affect adversely the room temperature mechanical properties they do influence the high temperature mechanical properties by acting as reactive sites for cavitation and as stress-risers [6].

The small-angle neutron scattering experiment was carried out on one of the samples from the NBS collection. The sanograph shown in figure 7 was from the creep sample and shows intensive scattering from particles. The drawing of the sanograph contours was shown and discussed earlier with figure 2A. The curve that was fitted to the measured intensity values is shown in figure 2B. The best fit to the curve of the scattering intensity vs Q data shows that the average scattering particle size is near 20 nm. This size is close to the small iron particles shown in figure 7. The larger tungsten carbide particles and clusters of particles are not measured using the SANS technique and can be detected by light microscopy and by transmission scanning electron microscopy.

In order to identify the cavities and microcracks that could be related to high temperature deformation, some thin foils were made from some of the specimens from the creep tests carried out at NBS [6]. Microcracks typical of creep in magnesia-doped silicon nitride are shown in figure 8. This figure shows both the surface displacement and extension of the glass grain boundary phase across the crack interfaces. Additional small microcracks along grain boundaries are visible in both the secondary electron image and in the transmission image. In the yttria-doped silicon nitride the creep process had a different mechanism because the bonding phase is crystalline (yttrium silicate) and is controlled by the diffusion between the bonding phase and the silicon nitride grains [6]. It was found (see figures 9 and 10) that the microcrack and cavity distribution varied with distance from the tensile and compression surfaces of the bent bars in both the amorphous bonded silicon nitride and the crystalline bonded silicon nitride. Therefore in

order to carry out a successful small angle neutron scattering experiment the sample material should be free of scattering centers such as tungsten and the sample should be from a tensile or compression test.

Zirconia

The proposed use of partially stabilized zirconia as a structural ceramic exposed to thermal cycling and to thermal and mechanical stress requires some means of observing the development of microcracks during these processes. Our assessment of the small angle neutron scattering technique with silicon nitride and silicon carbide indicates that it would be useful for analysis of microcracking in zirconia materials. The initial studies of the possible microcrack populations has been carried out using light microscopy and scanning and electron microscopy [11]. Some of the electron microscopy results are included in this paper because of the general interest in zirconia expressed at this meeting.

The samples were chosen from commercial samples that were partially stabilized with magnesia additions. Examples of the form and distributions of pores and microcracks in these materials are shown in figures 11 and 12. As seen in these pictures the pores occur along grain boundaries and within grains and have a broad range of sizes and shapes. Regions of excessive porosity such as that shown in figure 11 could cause the low flexure strengths in some tested bars. The pore shown in figure 12B appears to be similar to pores in figure 12A and is within a grain of cubic and tetragonal ZrO_2 . The particles in the pore were identified from electron diffraction and from energy dispersive x-ray spectroscopy as silicon. Microcracks were found in both as-received samples and in the

samples heated 100 h at 1000 °C at the interfaces between the twinned monoclinic plates and the grain boundaries as shown in figure 13. Such microcracks are of a size that could be detected by SANS.

Summary

The combining of scanning transmission electron microscopy and small angle neutron scattering is shown to be a useful approach for examining the cavity and microcrack populations in the structural ceramics SiC, and Si₃N₄. In order to develop the SANS technique to be an effective non-destructive technique it is apparent that calibration materials must be carefully selected to contain an identifiable cavity and microcrack population without the complications of extraneous defects. Partially stabilized zirconia samples are suggested as candidate materials for future work.

Acknowledgement

The work was supported in part by the Army Materials and Mechanics Research Center and by the Air Force Office of Scientific Research. One of the authors (Y.N. Lu) was supported by a grant from the United Nations Industrial Development Organization.

References

1. D.J. Green, P.S. Nicholson and J.D. Embury, Fracture Toughness of a Partially Stabilized ZrO₂ in the System CaO-ZrO₂, J. Am. Ceram. Soc. 56, 619-623 (1973).
2. N. Claussen and J. Steeb, Toughening of Ceramic Al₂O₃ Composites by Oriented Nucleation of Microcracks, J. Am. Ceram. Soc. 59, 457-458 (1976).
3. T.-J. Chuang, N.J. Tighe and S.M. Wiederhorn, Submicro crack growth of Y₂O₃-doped Silicon Nitride at Temperature. Sixth International Conference on Fracture, New Delhi, India, to be published.

4. C.J. Glinka, SANS Facility at National Bureau of Standards, AIP Conference Proceedings No. 89, J. Faber, ed. Neutron Scattering, 1981, p. 395.
5. R.K. Govila, Uniaxial Tensile and Flexural Stress Rupture Strength of Hot-Pressed Si_3N_4 , J. Am. Ceram. Soc. 65, 15-21 (1982).
6. N.J. Tighe, S.M. Wiederhorn, T.-J. Chuang and C.L. McDaniel, Creep Cavitation and Crack Growth in Silicon Nitride, in Deformation of Ceramic Materials, R.E. Tressler and R.C. Bradt, ed., Plenum Press, 587-605 (1984).
7. Y. Murata and R.H. Smoak, Densification of Silicon Carbide by the Addition of BN, BP and B_4C and Correlation to Their Solid Solubilities in International Symposium of Factors in Densification and Sintering of Oxide and Non-oxide Ceramics, Hakane, Japan, p. 382-399 (1978).
8. K.W. Benn and W.D. Carruthers, 3500 Hour Durability Testing of Commercial Ceramic Materials, NASA CR-159785, Intrim Report, July 1980.
9. E.R. Fuller, L. Chuck, C.L. McDaniel and N.J. Tighe (to be published).
10. R.C. Garvie, J. Phys. Chem. 82, 218-224 (1978).
11. Y.N. Lu, The Features of Microstructure and Microcracks in Partially Stabilized Zirconia Alloys, to be published NBSIR (1985).
12. J.R. Weertman, Nondestructive Evaluations: Microstructural Characterization and Reliability Strategies, ed. O. Buck and S.M. Wolf, Am. Inst. of Mining, Metallurgy and Petroleum Engineers, New York, p. 147-168 (1981).
13. D.J. Johnson, The Microstructure of Various Carbon Fibers, International Conference on Carbon Fibers, London 1971, p. 8/1-85, Gresham Press, Surrey.
14. A. Fourdeux, R. Perret and W. Ruland, General Structural Features of Carbon Fibers in International Conference on Carbon Fibers, London, 1971, p. 9/1-9/10, Gresham Press, Surrey.
15. F.A. Khoury and E.A. Boucher, On the Fine Structure of Carbon Fibers, 28th Annual Proceedings EMSA, 1970, Calitor's Publ., Baton Rouge.
16. G. Downing (private communication).

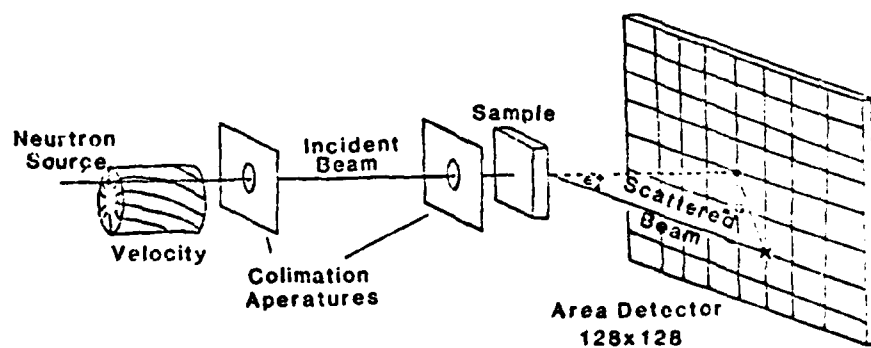


Figure 1. Schematic drawing of the major components of the small angle neutron scattering apparatus.

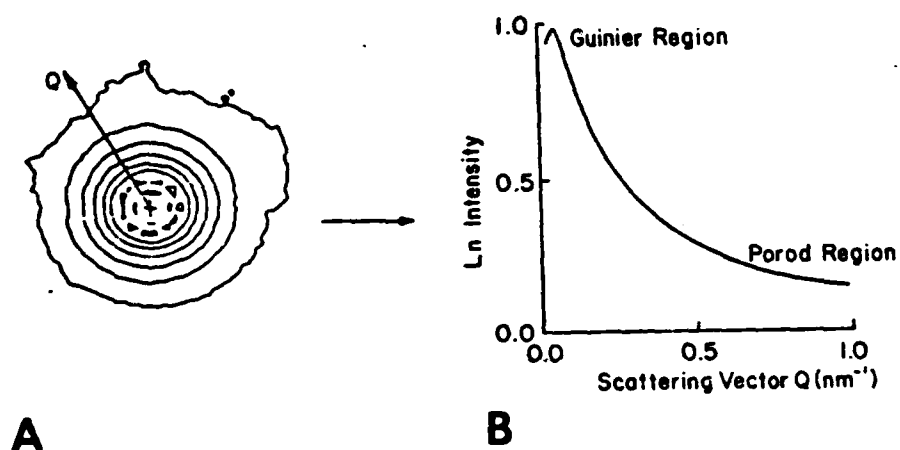


Figure 2. Schematic drawings of single particle diffraction data from (A) the two dimensional detector showing the center of the incident neutron beam (+) and the scattering vector Q ; and (B) the circularly averaged intensity as a function of the scattering vector Q . (Data were obtained from a Si_3N_4 specimen).

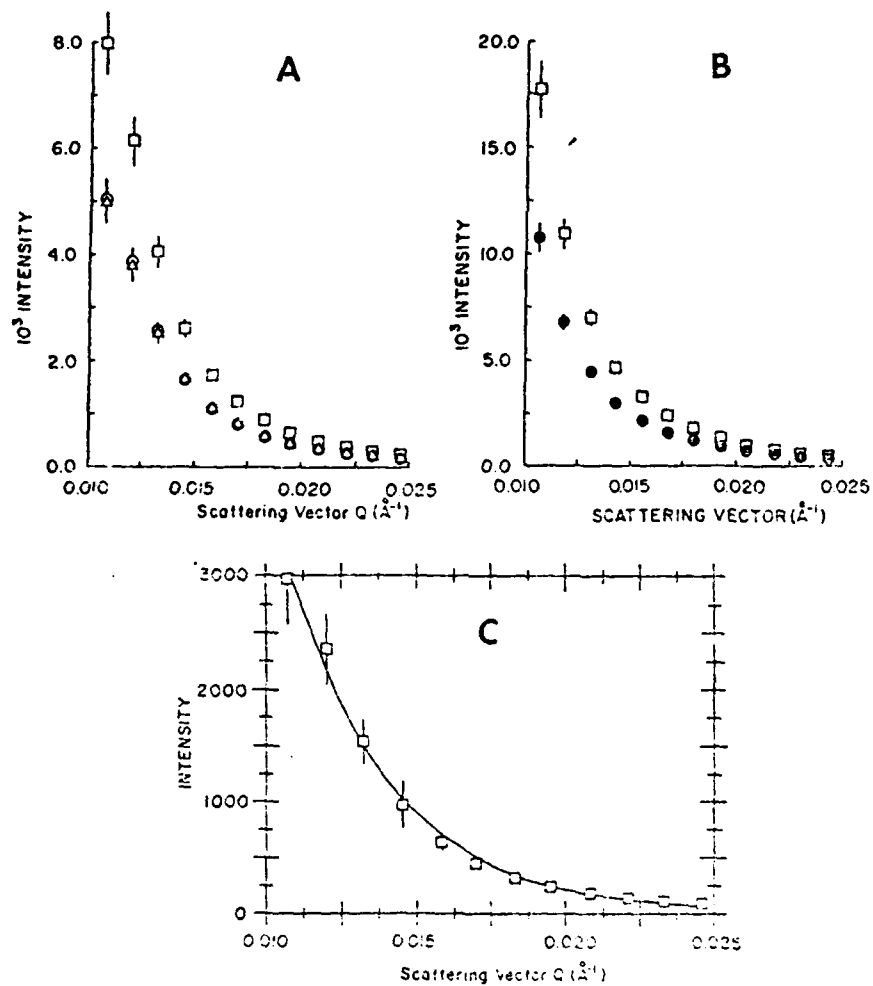


Figure 3. Plots of scattered intensity vs scattering vector for the SiC samples (A) \square SiC-1, \circ SiC-2, \triangle SiC-3; (B) \square SiC-1, \bullet SiC-4; (C) \square (SiC-1 - SiC-3).



Figure 4. Graphite inclusions in α SiC (a) fibrous form found at triple junctions of grain boundaries; (b) compact morphology found within and between grains of SiC.

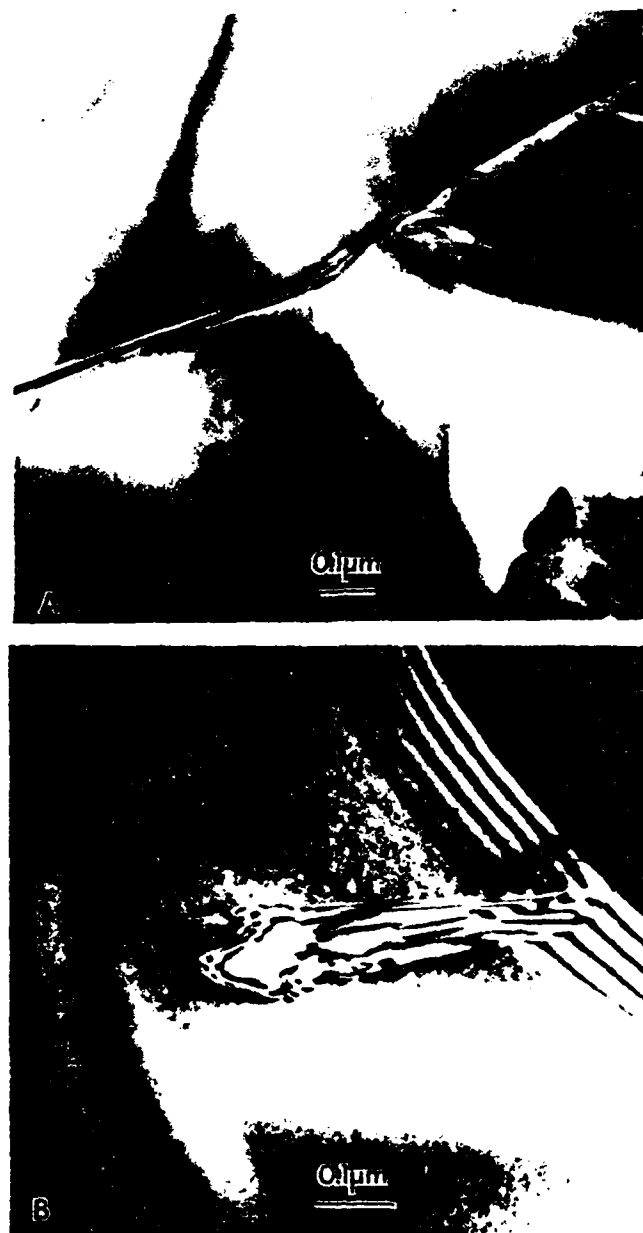


Figure 5. Alpha SiC after 3500 h thermal cycle test showing (a) triple junction with amorphous film and remnant of carbon fibers; (b) healed microcrack in SiC grain.



Figure 6. Hot-pressed Si₃N₄ + MgO showing Fe and WC inclusions along grain boundaries and at triple junctions.

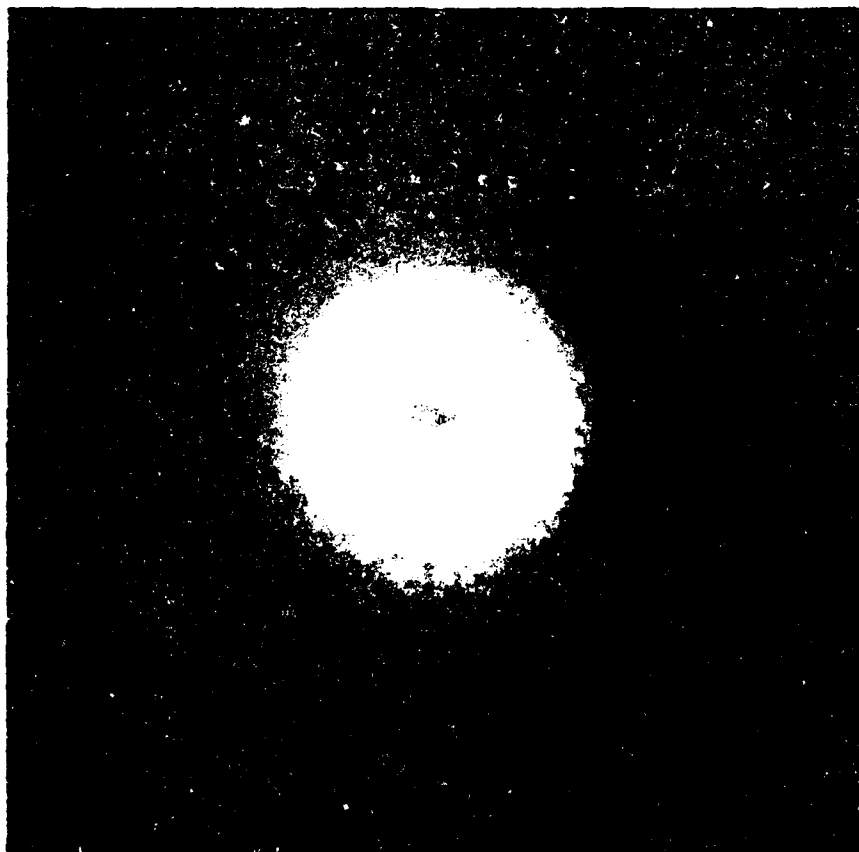


Figure 7. Sonograph taken of small angle neutron data image displayed on the computer terminal.

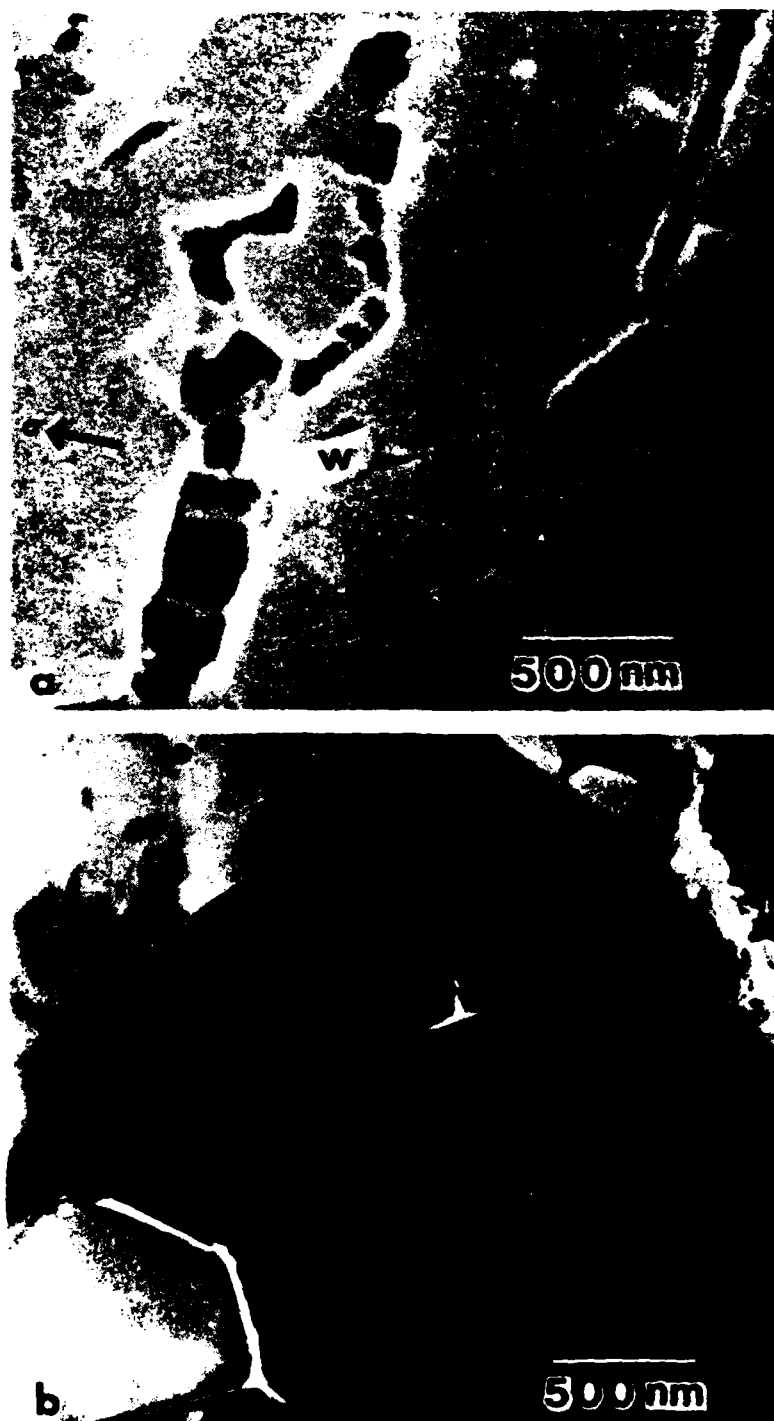


Figure 8. Thin foil of $\text{Si}_3\text{N}_4 + \text{MgO}$ specimen bent at 1400°C showing creep cracks along the interface with the amorphous grain boundary phase stretched across the interfaces; (b) grain boundary cracks as imaged by transmission electron microscopy in the same region.

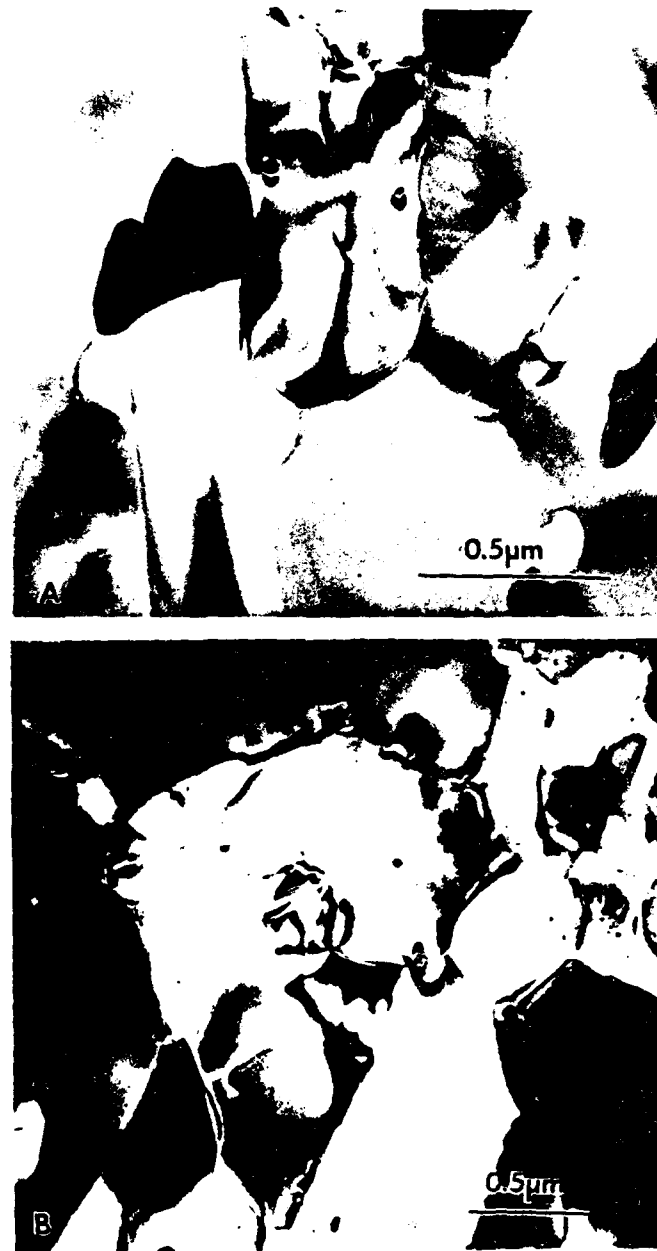


Figure 9. Hot-pressed $\text{Si}_3\text{N}_4 + 8\% \text{Y}_2\text{O}_3$ bent at 1400°C during 168 h showing microstructure near the (a) tension and (b) compression surfaces. The large pores remain where the yttria phase oxidized. Compression side shows strain contours at mid-points of grain boundaries and diffusion tunnels from WC particle movement.



Figure 10. Microstructure in $\text{Si}_3\text{N}_4 + \text{Y}_2\text{O}_3$ specimen approximately 10 μm below the tensile surface showing crack-like diffusional cavities along grain boundaries, spherical cavity at mid-grain boundary and triple junction pore where yttrium silicate phase oxidized.

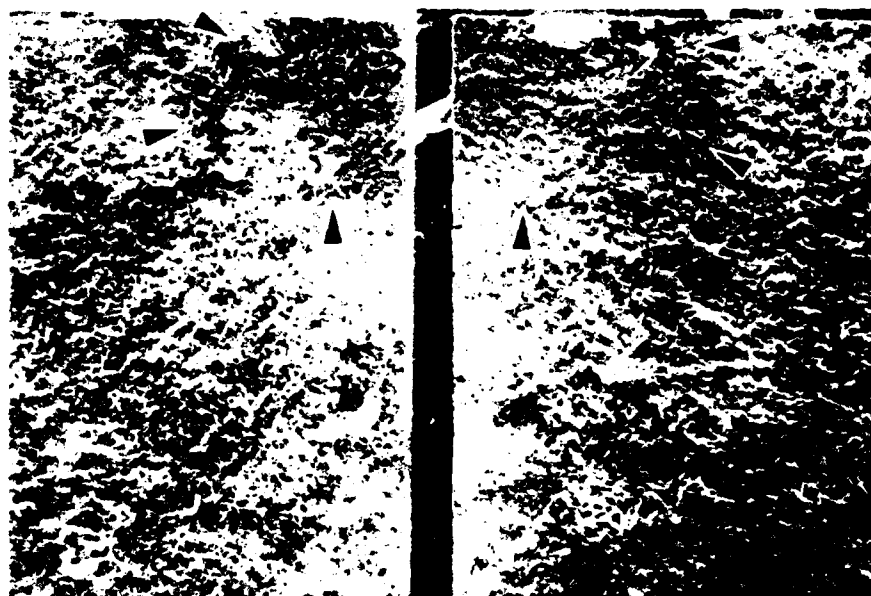


Figure 11. Fracture interfaces in MgO stabilized ZrO_2 test bar fractured at 300 MPa at 1000°C.

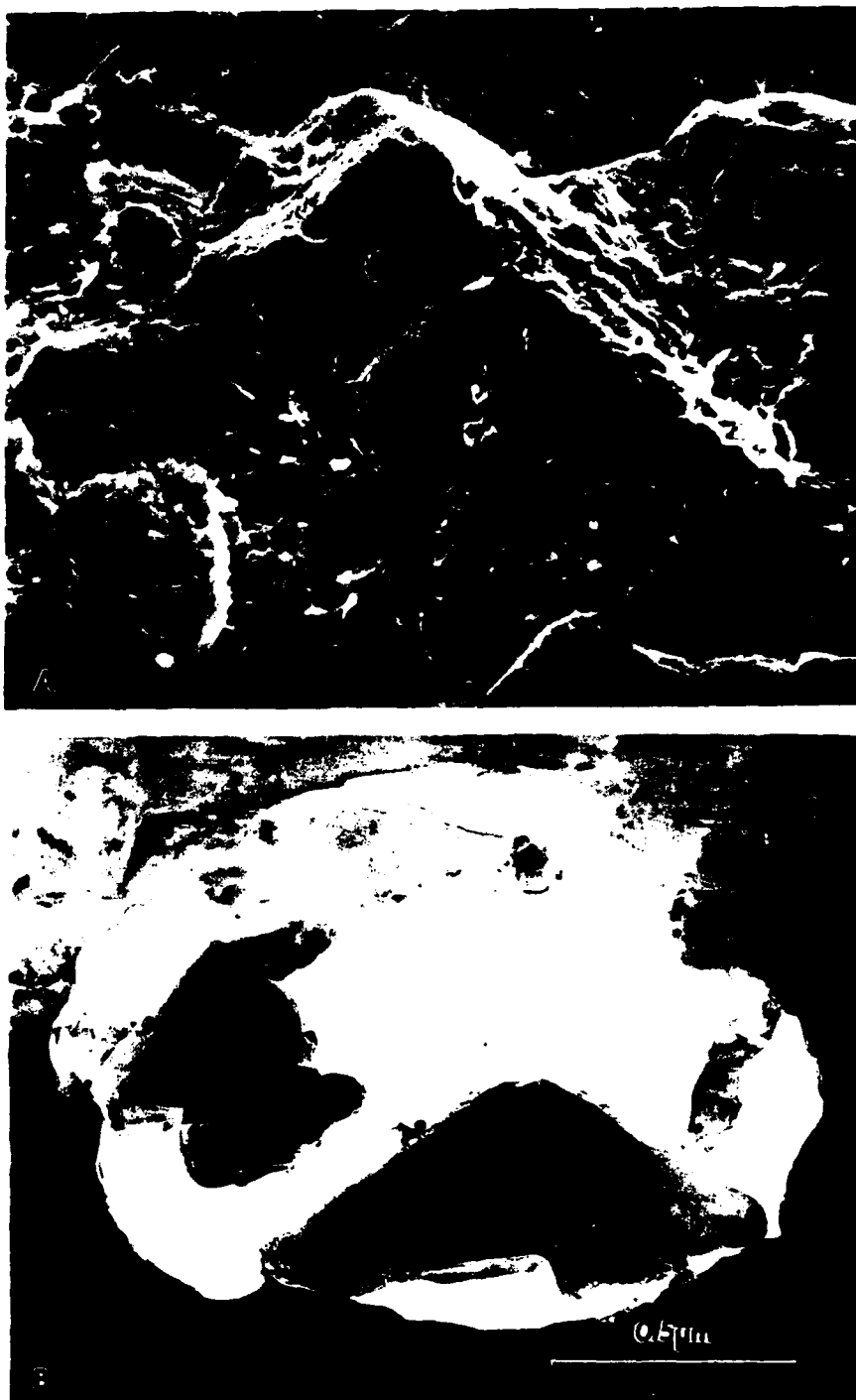


Figure 12. MgO-doped ZrO_2 fracture interface showing (a) pore distribution, (b) transmission electron micrograph of pore containing Si particles. Grain has plates of tetragonal phase.



Figure 13. Microcracks at interfaces of twin boundaries and adjacent grains in magnesia stabilized zirconia.

CREEP AND FRACTURE OF VITREOUS BONDED ALUMINUM OXIDE

S.M. Wiederhorn, B.J. Hockey and R.F. Krause, Jr.
National Bureau of Standards
Gaithersburg, MD 20899

and

K. Jakus
University of Massachusetts
Amherst, MA

(THIS PAGE IS BLANK)

CREEP AND FRACTURE OF VITREOUS BONDED ALUMINUM OXIDE

ABSTRACT

Creep and creep-rupture behavior of a commercial grade of a glass-bonded, 96 percent aluminum oxide was characterized as a function of temperature and applied stress. The creep data were fit to the classical empirical relation usually used to describe this phenomenon. The apparent activation enthalpy, $\Delta H = 926 \text{ kJ/mol}$, and the stress exponent, $n = 4.8$, lie at the high end of the range reported for two phase materials, primarily as a result of structural modifications that occur during creep. A stress-modified Monkman-Grant relationship was fitted to the creep-rupture data to give a stress exponent of -4.2 . None of the available theories of creep-rupture provided a satisfactory description of the present set of data.

Analytical electron microscopy was used to characterize the composition and structure of this material. In the as-received material the intergranular phase was a glass of nearly uniform composition. During high temperature exposure, devitrification of the glass resulted in the formation of various crystalline phases within the intergranular region of the material. Devitrification depended on both the proximity to the surface, where it was most pronounced, and on the state of stress. In this regard, flexural creep samples exhibited extensive crystallization within the tensile region of the flexural specimens, but little crystallization within the compressive cross section. From the composition of the retained glass, estimates of the viscosity of the glass

at the grain boundaries were made and used, in combination with microstructural information, to compare the creep behavior with available theories of creep. The results of this paper are consistent with percolation and solution precipitation mechanisms of creep deformation. By contrast, cavitation did not seem to play a major role in the creep deformation process. After extended periods of time, however, cavitation and delamination of two grain junctions provided the nucleating sites for crack growth and fracture.

1. Introduction

Current interest in the mechanical behavior of multiphase ceramics has its origin in the potential use of these materials in high temperature structural applications. In the automotive industry, for example, two phase ceramics such as sintered silicon nitride and glass-bonded cordierite are being used as structural materials for combustors, turbines, turbochargers and heat regenerators [1]. In the power industry two phase materials are being considered for heat recuperators and for linings in slagging gasifiers [2]. In these applications, the mechanical response of the ceramic to external forces depends on the microstructure, in particular on the refractoriness and chemical activity of the phases that make up the ceramic. Most high temperature structural ceramics consist of highly refractory grains bonded by a less refractory vitreous intergranular phase. Therefore, creep and creep rupture of these materials depends primarily on the physical and chemical properties of the vitreous phase and on the amount and distribution of the vitreous phase within the ceramic structure.

Because of the importance of the intergranular vitreous phase to the structural integrity of high temperature ceramics, most recent studies on these materials have concentrated on characterizing the behavior of the vitreous phase as a means of understanding the behavior of the ceramic composite. Thus, Lange and his co-workers [3] have shown how the compressive creep behavior of silicon nitride can be modified by changing the composition and volume fraction of the glassy phase within hot-pressed silicon nitride. These authors also demonstrated that high temperature exposure, which removes glass modifiers from the vitreous matrix, also greatly reduces the susceptibility of the hot-pressed silicon nitride to creep [4]. These findings reinforced earlier findings of Kossowsky, Miller and Diaz [5], who showed that glass modifiers, such as calcium, reduce the viscosity of glass and therefore increase the susceptibility of hot-pressed silicon nitride to creep. Similar findings were made by others on porcelains [6], fire bricks [7] and on glass ceramics [8].

Despite our general understanding of the importance of glass composition and structure to creep and fracture, it is only now with the development of high resolution analytical microscopy that the chemical composition of the glass bonding phase can be determined. Evaluation of the glass composition opens the possibility of estimating physical properties of the glass matrix, such as diffusivity or viscosity which are required for the critical evaluation of most theories of creep and creep rupture. By analyzing the composition of the vitreous matrix, these physical properties can be either determined experimentally on a similar

composition of glass, or estimated theoretically, and a direct comparison between these theories of creep and creep-rupture, and experimental creep and creep-rupture data can be made.

In this paper analytical electron microscopy is used to elucidate the creep and creep-rupture behavior of a commercial grade of vitreous bonded aluminum oxide. The chemical composition of the glass bonding phase is determined before and after static annealing and creep deformation. From the chemical compositions, theoretical estimates of the viscosity of the glasses are made in order to compare creep and creep-rupture theory with experimental data. The electron microscope is also used in a more classical way: as a method of identifying changes in the microstructure that occur during creep. Using these methods, the creep rate is shown to be determined by the viscosity of the glass, suggesting that viscous flow and/or solution precipitation contribute to the creep process. Although cavitation is not observed to occur homogeneously in our specimens, cavitation at select boundaries followed by crack growth is believed to be important in later stages of the creep process.

2. Experimental Procedure

Creep and creep rupture experiments were conducted on a commercial grade of vitreous bonded aluminum oxide, Coors AD-96,^{1/} reported to contain 96 percent aluminum oxide. Experiments were conducted using 4-point bending as a test technique. This technique was selected for ease of testing and for the fact that specimens for the electron microscope could be obtained from the tensile and compressive portions of the same

^{1/} Identification of this material is not to be construed as endorsement by the National Bureau of Standards.

specimen, thus excluding thermal history and extent of strain in comparative analysis. Creep-test specimens, 3 mm high and 5 mm wide were loaded on a bending fixture of silicon carbide with outer and inner loading points of 40 mm and 10 mm respectively. Approximately one-half the specimens were polished on the tensile surface to permit identification of incipient failure sites and crack nuclei as they formed during creep. Dead weight loads from 40 to 100 N were applied via a lubricated rubber diaphragm air cylinder, which, in combination with a two-step, continuous leak pressure regulator, was capable of maintaining the applied load to within ± 1.5 N. Stress and strain were calculated by the procedure given in reference 9, assuming a stress exponent of unity. No further corrections to the estimated stresses and strains were made in the present paper.

The loading point displacement during creep was monitored by a linear voltage-displacement-transducer (LVDT) that was attached to the upper ram of the test equipment. The loading point displacement of specimens was measured to within ± 2 μ m. To enhance the long term accuracy of the displacement readings, a block of sintered silicon carbide, of the same grade as that used for the rams, was used in one of the three test stations in each furnace. Since the block did not undergo creep at the loads and temperatures used in the present study, any displacement measured by the LVDT on the block reflected changes in the test facility due to electronic drift or to fluctuations in the ambient temperature. These displacement fluctuations were subtracted from the displacements measured on the specimens in the other two stations of the same furnace, so as to minimize errors due to electronic drift or to differential thermal expansion of the test fixture. Even though two specimens were

tested in the same furnace for each run, the failure of one specimen was never observed to affect the other in the course of our investigation, primarily because pneumatic bellows and rubber shock absorbers were used to restrain propagation of stress waves.^{2/}

Recognizing that phase changes often occur in ceramics during extended high-temperature exposure [6,7], most specimens were annealed at 1050°C for a period of 96 hours before testing to stabilize the ceramic against composition or structural changes that might influence the creep behavior. Since most of the creep studies on this program were typically less than 100 hour duration, it was hoped that this annealing period would be sufficient to insure a constant structure for the present investigation. Despite this precaution, some phase changes were observed during creep. The affect of annealing on both creep and microstructure represents an important aspect of our results and accordingly will be discussed extensively below.

To establish the temperature range to be investigated, a stepped-temperature creep test [10] was conducted using an initial applied stress of 60 MPa, which was approximately one-third of the reported breaking stress at 1000°C. In this test, a constant load was applied to the specimen, and the temperature was increased at various time intervals until either failure occurred, or deformation was so severe that further creep was pointless. Significant creep activity for this material starts at approximately 950°C; at 1050°C the creep of the ceramic is relatively rapid, failure occurring in approximately 24 hours at approximately 0.14%

^{2/} Bellows are a non-inertial method of loading the specimens, and the air gaps in the bellows do not permit the passage of a stress wave. Hence, when a specimen breaks, the stress waves resulting from the fracture are largely dissipated before reaching the second specimen.

strain. Based on these results, experiments were conducted at temperatures ranging from 980 to 1100°C, and at loads ranging from 40 to 100 MPa.

Specimens for examination by transmission electron microscopy (TEM) were obtained from the deformed bend bars using standard sectioning, polishing and ion-milling techniques. Two types of sections were used in these studies, figure 1. Specimens with the major plane of the foil parallel to the plane of maximum tensile or compressive stress (a in figure 1) were used to analyze the near surface regions of the specimen, i.e. from 0 to 50 μm from the external surface. Specimens with the plane of the foil perpendicular to the bending axes (b in figure 1) were used to examine changes in composition and structure at greater distances (0.2 to 1 mm) from the tensile or compressive surfaces of the creep specimens. This orientation was selected to examine the ceramic structure as a function of distance from the tensile and compressive surfaces of the bend bars.

3. Experimental Results

3.1 Microstructure

A representative view of the material used in this study is shown in figure 2. The material consists principally of aluminum oxide grains (A) bonded by an intergranular matrix phase (M). Interspersed throughout the material there are also abnormally large grains of spinel (MgAl_2O_4), S, ranging in size from 20 to 40 microns, and irregularly shaped pores of microscopic (5 to 10 microns) dimensions. Using the line intercept method, the mean grain size of Al_2O_3 was determined to be 8 microns, but ranged from -3 to 20 microns. The volume fraction of intergranular matrix

phase, which was located primarily at multi-grain junctions, was roughly 10 percent. The porosity of the material was also roughly 10 percent by volume.

In applying TEM, major emphasis was placed on determining the structure and chemical composition of the intergranular matrix phase. Chemical compositions were determined by energy dispersive x-ray analysis (EDX) using the ratio method in the thin-foil approximation [11] after background subtraction by linear extrapolation. The required K-values for the various oxides³ were determined from spectra obtained from two glass standards (Table 1), which were also prepared by ion-milling. In all cases, spectra from either the standards or the unknowns were taken under similar conditions (beam current, beam size, angle of tilt, etc.), a precaution necessitated by the presence of sodium in both the glass bonding phase and in one of the crystalline products of devitrification. The highly volatile nature of sodium during electron irradiation, moreover, placed severe restrictions on the imposed electron beam flux and duration of exposure. Most generally, this precluded the use of a focused probe regardless of other operating conditions and required the use of defocused beams of (typically) 400 μm or greater in diameter. While many grain boundary widths were considerably smaller than this limiting probe size, most joined continuously with triple junctions of larger dimensions. As a check on spacial resolution, "hole count" spectra-obtained from etched out grain boundaries and triple junctions showed only an insignificant Al intensity enhancement while differences in the elemental

³/ It was assumed that all constituents were present as stoichiometric oxides.

composition of the various intergranular phases allowed for a ready check on possible "overlap". In all cases, chemical compositions are given in terms of average values obtained from at least ten determinations.

Transmission electron microscopy provided not only a more detailed view of the microstructure, but also revealed that pronounced changes occur within the intergranular bonding phase due to prolonged static annealing and creep. In the as-received material, the intergranular bonding phase was found to consist entirely of a glass, figure 3. EDX analyses of the glass found at triple junctions (figure 3a), two-grain boundaries (figure 3b), and larger multi-grain junctions or "pockets" gave a fairly uniform composition listed in Table 2. Though not particularly evident in figure 3, most Al_2O_3 grains were separated by a glass film which, due to the irregular morphology of the Al_2O_3 grains, ranged in thickness from roughly 10 nm to upwards of several tenths of a micron. In this regard, the relatively wide, glassy grain-boundary region - as well as the apparent Al_2O_3 surface faceting - seen in figure 3b was not uncommon. The results thus indicate that, in the as-received condition, the binding phase can be regarded as a continuously-linked, glassy structure.

Upon prolonged annealing (1050°C, 96 hours), pronounced changes were found within the binding phase due to partial devitrification of the glass. Specifically, devitrification results in the formation of various crystalline phases and, as a consequence, changes the volume fraction and composition of the retained glassy phase. Although devitrification occurs throughout the samples, it is most pronounced within the surface regions. Accordingly, results obtained from the interior and from the surface regions of bulk, annealed samples are described separately. Within the interior of annealed samples, analytical electron microscopy revealed only

the presence of two different magnesia alumino-silicate phases within the binder phase: one having an average composition of $4\text{MgO} \cdot \text{Al}_2\text{O}_3 \cdot 4\text{SiO}_2$ and isomorphic with orthorhombic enstatite (MgSiO_3); the other having an average composition of $2\text{MgO} \cdot 2\text{Al}_2\text{O}_3 \cdot \text{SiO}_2$ and isomorphic with monoclinic sapphirine ($7\text{MgO} \cdot 9\text{Al}_2\text{O}_3 \cdot 3\text{SiO}_2$). Moreover, small crystallites of one or both of these phases were found within many, but not all, of the larger triple junctions or multi-grain "pockets" (figure 4a), and never within two-grain boundaries. Because of this, devitrification results in only a minor decrease in the volume fraction of the glassy phase, (estimated at less than 10%). This however, is sufficient to produce a significant change in glass composition which from Table 2 is seen to be nearly depleted in MgO. Here it is important to note that the observed change in glass composition was uniform throughout the interior of annealed samples, regardless of whether localized crystallization had occurred.

As indicated earlier, devitrification was especially pronounced within the surface regions, where it is estimated that from 50 to 75% of the intergranular glassy phase devitrified during annealing. Although enhanced formation of both magnesio-alumino-silicate crystalline phases at the surface played a role in reducing the volume fraction of glass, the reduction of glass fraction was primarily related to the formation of a triclinic, sodium-calcium alumino-silicate phase identified by electron diffraction and chemical analyses (Table 2) as intermediate plagioclase.^{4/} Unlike the magnesio-alumino silicate phases, the intermediate plagioclase

^{4/} The chemical composition of members of the plagioclase series is generally given in terms of its pure end members anorthite (An), $\text{CaAl}_2\text{Si}_2\text{O}_8$ and albite (Ab), $\text{NaAlSi}_3\text{O}_8$. On this basis, the average composition listed in Table 2 corresponds to 50% Ab-50% An, although considerable variations in compositions and a systematic calcium deficiency was observed.

formed more uniformly throughout the intergranular regions and often resulted in the (apparent) complete crystallization of two-grain boundaries and multi-grain junctions (figure 4b). Moreover, the additional crystallization of plagioclase within the surface regions results in a retained glass phase composition, Table 2, which is more silica-like, and hence, is different from the glass phase found within the interior.

To a large extent, analytical electron microscopy results for annealed samples provide a basis for summarizing the differences in microstructures found within samples that were preannealed at 1050° and then were deformed in creep to -0.1% strain at an applied stress of 60 MPa. Again particular emphasis is placed on the intergranular regions, since this is where deformation occurs. With reference to figure 1, samples taken from within 100 microns of the tensile and compressive surfaces of deformed samples were virtually indistinguishable from each other and from those from the surfaces of statically annealed samples. In each, the intergranular binder phase was largely crystalline (again estimated as up to 75% of binder phase volume), due to the formation magnesio-alumino-silicates and intermediate plagioclase. From Table 2, the compositions of retained glass in the surface intergranular regions was also quite similar. Tensile surface sections were, however, marked by the occasional presence of stoichiometric, orthorhombic cordierite and, in samples where the original surface was retained, by the presence of discrete magnesio-alumino-silicate crystallites along the periphery of two-grain boundaries and multi-grain junctions. By scanning electron microscopy these crystallites were determined to lie on the surface, thus indicating a transfer of material from the interior to the tensile surface.

Further examination of deformed samples, using longitudinal cross-sections (figure 1), provided clear evidence that the stresses developed during testing have a significant effect on the devitrification process and hence, the structure and composition of the intergranular binding phase. Within the tensile regions, extensive devitrification of the glass binder phase resulting in 50-70% crystallization, extended to distances of approximately one-fourth the sample thickness (the limit of observations). In contrast, the degree of devitrification diminished rapidly below the compressive surface, and, at a depth corresponding to one-tenth the sample thickness, the binder phase was essentially glassy. Within the compressive regions, the structure and composition of the binder phase was, in fact, nearly identical to that found within the interior of bulk annealed samples; whereas, within the subsurface tensile region, it closely resembled that found at the surface. Again the large differences in both volume fractions and composition (Table 2) of intergranular glass that develops within creep samples could be related to the preferential crystallization of intermediate plagioclase within the grain boundaries throughout the tensile regions, figure 5.

Creep samples were also examined for evidence of void or cavity formation within the intergranular phase. In contrast to earlier results for hot-pressed silicon nitride (tested in both tension and compression) [3,5,12-14] and for a glass-bonded alumina (tested in compression) [15], definitive evidence for wide-spread cavitation was not found.^{5/} Nevertheless, observations on tensile surface regions by SEM, figure 6a,

^{5/} While cavity-like holes were often found within multi-grain junctions even in thick regions of TEM samples, they were similarly present in tested and un-tested samples and are, therefore, attributed to preferential ion-thinning.

clearly showed intergranular cavitation, though it was generally restricted to the neighborhood of well developed creep cracks. In addition, transmission electron microscopy studies on similar tensile surface sections revealed occasional evidence of grain boundary delamination in the form of narrow plate-like cavities, figure 6b. While it appears clear that grain boundary delamination eventually leads to the formation of fully developed cracks that are responsible for creep rupture, the necessary conditions and processes involved in crack formation remain the object of continuing study.

3.2 Creep Data

Examples of creep data obtained in the present experiment are illustrated in figures 7 and 8. There was little indication of stage 3 creep prior to failure in any of the creep tests. Failure often occurred without any change in the creep rate, suggesting that a second process, such as rapid crack growth, abruptly cuts-off the normal creep process in these specimens. Sometimes a slight increase in the creep rate is observed just before failure, but the sort of creep-rate enhancement often reported for structural metals does not occur for this ceramic. This slight increase in creep rate is probably due to an increase in specimen compliance resulting from rapid crack growth.

Considerable run-to-run scatter was observed in the failure times for a given test condition even when specimens were tested simultaneously in the same furnace. Scatter in the failure times by as much as a factor of three were not uncommon. By contrast, the minimum creep rate for a given test condition was relatively constant from run to run. Finally, annealing has an enormous effect on the creep behavior of this material.

The annealing treatment of 96 hours at -1050°C , decreased the creep rate and increased the lifetime by a factor of almost 100 (figure 7). As will be discussed below, this decrease in the creep rate can be directly attributed to devitrification and to the changes in the volume fraction and the viscosity of the glass at grain boundaries.

The creep data illustrated in figures 7 and 8 may be summarized by expressing the minimum strain rate, $\dot{\epsilon}$, as a function of applied stress, σ , and temperature, T :

$$\dot{\epsilon} = A (\sigma/\sigma_0)^n \exp (-\Delta H/RT) \quad (1)$$

where R is the gas constant and A , n and ΔH are empirically determined constants. The constant A has units of hr^{-1} and the normalization constant, σ_0 , for the stress has units of MPa. In the present experiment, the constants A , n and ΔH were determined by a least squares fit of eq. 1 to 28 sets of the experimental data. The values of these constants and their standard deviations are: $\ln A = 53.6 \pm 5.0$; $n = 4.85 \pm 0.45$; $\Delta H = 926 \pm 58 \text{ kJ/mol}$. The standard deviation of the fit was approximately ± 0.45 .

3.3 Creep Rupture Behavior

The creep-rupture data obtained in the present experiment are summarized in figure 9 where the logarithm of the minimum creep rate is plotted as a function of the logarithm of the rupture time. As can be seen from this figure, there is a negative correlation between the minimum

strain rate and the time to failure. If the failure time is expressed as a power function of the minimum strain rate, then the data shown in figure 9 can be expressed by the following equation:

$$t \dot{\epsilon}^a = b \quad (2)$$

where the constants and their standard deviations, $a = 1.10 \pm 0.11$ and $\ln b = -8.97 \pm 0.13$, were obtained by a linear regression analysis of $\ln t$ upon $\ln \dot{\epsilon}$ for 21 sets of data. The standard deviation of the fit was approximately 0.72. Equation 2 is the Monkman-Grant [16] equation, first used to describe the creep of metals. The exponent, a , in this equation is not significantly different from 1, the value usually used to describe creep.

The variance of the data about the regression line in figure 9, can be reduced significantly if temperature and/or applied stress are introduced as variables. This is illustrated in figure 10 where the data from figure 9 have been replotted and identified as either constant temperature (figure 10a) or constant stress (figure 10b) data. In both representations, the data is observed to be layered: the data lie on straight lines of either constant temperature or constant stress. Furthermore, it can be seen that the scatter of the data about the lines, in either representation, appears to be less than that given by the Monkman-Grant relation, indicating the importance of temperature and stress as experimental variables.

The introduction of temperature and applied stress into the analysis can be quantified by assuming that the creep rupture data fit an empirical equation of the following type:

$$t \dot{\epsilon}^a = B \sigma^m \exp (-\Delta H'/RT) \quad (3)$$

By taking the natural logarithm of both sides of the above equation, the equation can be linearized and the constants, a , B , m and $\Delta H'$ can be determined by a linear regression analysis of the data. The results of this analysis are given in Table 3. A large and significant dependence of $t \dot{\epsilon}$ on applied stress and temperature indicates that some of the variance in figure 9 can be attributed to a variation in these two parameters. In fact, the standard deviation of the fit, ± 0.34 , is reduced by a factor of approximately 2 by taking temperature and stress into account.

3.4 Strain at Failure

Another relationship that can be obtained from the creep rupture data is the maximum strain to failure. In the metals literature, the assumption of a constant maximum strain to failure is often used as a criteria for failure [17]. The unmodified Monkman-Grant relation, equation 2, for example, is essentially a constant strain to failure criterion. By plotting the strain to failure as a function of other test variables, it should be possible to provide additional data for comparing creep and creep-rupture data with theory.

In figure 11, the strain to failure is plotted as a function of the applied stress. Although the scatter of the data is considerable, the figure suggests a negative correlation between these two variables, so that as the stress applied to the specimen is decreased, the failure strain is observed to increase. This correlation is supported by data collected on two other specimens loaded at 40 MPa and 1044°C for a period

of 350 hours. Although they did not fail, strain on the specimens at the time the tests were discontinued were 0.17 and 0.21 percent, which were greater than any of the failure strains indicated in figure 11.

4.0 Discussion

4.1 Grain Boundary Viscosity

In the temperature range used in the present investigation all but a few high silica glasses behave as viscous liquids. Therefore, the glasses at grain boundaries in the present study are also most likely to be liquid, and liquid enhanced creep undoubtedly dominates the creep results presented in this paper. In all of the theories developed to describe the effect of intergranular liquids on creep deformation, the viscosity of the liquid is an important variable, which should be evaluated to fully understand the creep process. Therefore, in this section the viscosity of the intergranular glass is calculated from its composition. In the next section, these calculated viscosities are used to evaluate mechanisms of creep.

The viscosities of the vitreous grain boundary phases were estimated from the compositions given in Table 3, by using empirical equations developed by Urbain for this purpose [18]. The Urbain equations were developed from experimental data on a series of calcia-alumina-silicate glass melts and were tested on a number of slags and glasses for which the equations give values of viscosity that agreed with experimental measurements to within a factor of 5 [19]. The equations were, however, developed for the low viscosity range $<10^4$ Pa·s, so that agreement between these equations and experimental data is not expected over the entire range of viscosities.

Before using the Urbain equations on the present set of data, the equations were applied to commercial glasses with known compositions and viscosities. The glasses selected for comparison were made by the Corning Glass Company and have the composition indicated in Table 1 [20]. The calculated and experimental values of the viscosity for the C0080 glass, figure 12, agree to within an order of magnitude for the viscosity range 10^{11} Pa·s (530°C) to 10^2 Pa·s (1000°C), which was almost the entire practical range of viscosities for annealing and forming for this glass. For the C1720, figure 12, an order of magnitude agreement between calculated and measured viscosity is obtained for viscosities lying between 10^7 Pa·s (900°C) and 1 Pa·s (1200°C). This agreement between calculated and measured viscosities is considered reasonable for the present study.

The viscosities of the glass compositions given in Table 3 are shown in figure 13. The figure demonstrates the rather sizeable affect of annealing and deformation on the viscosities of these glasses. At any given temperature, changes by a factor of ten in viscosity are observed as a consequence of annealing and creep deformation. This increase in glass viscosity should reduce the creep rate of the annealed specimens by a commensurate amount, because the creep rate is inversely proportional to the viscosity in most theories of creep. Similarly, the additional factor of ~ 10 increase in the glass viscosity in both the tensile and compressive surfaces of the annealed specimens suggests that the surface of the specimens are more resistant to creep than the body of the specimens. This findings raises the possibility of surface embrittlement as a consequence of devitrification during annealing.

The difference in composition of the glass in the tensile and compressive cross sections suggests a difference in viscosity of the glasses in these cross-sections. Using Urbain's formulation, the viscosity of the glass in the tensile cross-section is calculated to be approximately a factor of three greater than that in the compressive cross-section. The presence of crystalline material at the grain boundaries of the tensile cross section magnifies the viscosity difference even further, so that the effective viscosity of grain boundaries that have been devitrified will be greater than that indicated by the viscosity of the glass alone. Thus, the effective viscosity of the material at the grain boundaries in the tensile cross section should be more than a factor of three greater than the effective viscosity of the material at the grain boundaries of the compressive cross section.

These effects of composition on viscosity have interesting implications with regard to effects of the state-of-stress on the creep rate. If the effective grain boundary viscosity were the sole determinate of creep rate, then one would expect tensile specimens to be more creep resistant than compressive test specimens, for an equivalent temperature and applied stress. In fact, experimental studies on this subject reach the opposite conclusion; creep occurs more easily in tension than in compression [21]. Therefore, while grain boundary viscosity is important, it is not the only physical or structural parameter determining the creep rate. The overall rheology of the test specimen, vis-a-vis, the state of stress must also be considered. Creep no doubt depends on details of the microstructure such as level of agglomeration, level of homogeneity and amount of direct contact between grains of the microstructure. These effects of microstructure have not yet been considered for ceramic

materials. In fact, most theories of creep assume a homogeneous microstructure, an assumption that is clearly not consistent with the structure of most materials investigated. Thus, while intergranular viscosity is probably of paramount importance in determining the creep rate of a component subjected to a particular state of stress, other factors must be considered when the state of stress is a variable.

The effect of devitrification on the creep rate can be quantified by comparing the creep rate of the annealed specimens with that of the as-received specimens. At 1044°C, and an initial applied load of 60 MPa, a 100-fold decrease in the creep rate is observed upon annealing the specimens. Based on most theories of creep, this result suggests a factor of 100 decrease in the effective grain boundary viscosity. Since the viscosity of the glass at the grain boundaries decreases by only a factor of 10 due to annealing, a change in glass composition alone cannot explain the decrease in creep rate. Crystallization of the grain boundaries effectively increases the average viscosity of the grain boundary phase by another factor of 10, and in this way, decreases the creep rate of the specimens.

4.2 Models of Creep

The simplest model of liquid enhanced creep is that of lubricated flow wherein the grain boundary glass behaves as a lubricant, reducing the friction between grains. For an applied deviatoric stress, $\bar{\sigma}$, the creep rate $\dot{\epsilon}$ is given as a function of grain size, d , grain boundary thickness, w , and viscosity, η [22]:

$$\dot{\epsilon} = \alpha (w/(w + d)) (\bar{\sigma}/\eta) \quad (4)$$

where α is a constant having a value of approximately 1/3. Substituting $\bar{\sigma} = 40$ MPa, $d = 8 \mu\text{m}$, $\eta = 10^6$ Pa·s (the value for the annealed specimen at 1040°C) into equation 1, we obtain a calculated value of the grain boundary thickness, w , of 1.8×10^{-15} m for a creep rate of $3 \times 10^{-9} \text{ s}^{-1}$ (60 MPa applied stress, 1040°C). This estimated value of w is, of course, sub-atomic indicating that frictional forces at grain boundaries provide almost no impediment to the creep process. Therefore, lubricated flow cannot possibly be an acceptable mechanism for the creep results in the present study. As noted by others [22, 23], lubricated flow is probably never an explanation for liquid enhanced creep because the mechanism does not take into account the complexity of the microstructure for most materials. Grains that form the microstructure do not lie in ordered planes, as assumed in the model of lubricated flow. When subjected to stress, grains tend to lock-up as the solid is deformed, greatly increasing the forces required to maintain a given rate of creep. In this way, the material work hardens. For flow to continue, i.e. for the grains to slide over one another, an increase in the volume, a dilatation, must occur [24, 25]. Therefore, if liquid lubrication were the only possible process, creep would become more and more difficult as the strain increased and the creep would eventually stop. In fact, creep continues because there are mechanisms of accommodations that relieve the stresses caused by the volume expansion. In the order to be discussed below these mechanisms include: (1) fluid flow or percolation; (2) pressure solution or solution precipitation; and (3) grain boundary cavitation.

Percolation, or fluid flow, was first mentioned as a mechanism of accommodation by Reynolds [24], and later by Frank [25]. The effect of fluid flow on creep was quantified by Drucker [26] and by Lange [23], who calculated the rate of creep resulting from the localized flow of liquid from the compressive to the tensile surfaces of individual grains. The equation developed by Drucker for the strain rate is

$$\dot{\epsilon} = (\sigma/\eta\sqrt{3})(w/d)^3, \quad (5)$$

where σ is the applied tensile or compressive stress. The model assumes the grains lie in a two dimensional hexagonal array and that flow is homogeneous throughout the material. Substituting experimental values of η (10^6 Pa·s), σ (60 MPa) and d (8 μm) into this equation yields the following relation between $\dot{\epsilon}$ and w : $\dot{\epsilon}/w^3 = 6.7 \times 10^{16} \text{ s}^{-1} \text{ m}^{-3}$, from which a grain boundary thickness of 3.5 nm is calculated for a creep rate of $3 \times 10^{-9} \text{ s}^{-1}$ at 1044°C. This value of the grain boundary thickness lies at the lower end of the range normally observed for glass bonded aluminum oxide, which suggests a significant resistance to fluid flow only occurs along the narrowest boundaries of the composite. During deformation, glass flows easily from pores or external surfaces along triple junctions and therefore wide grain boundaries offer little resistance to fluid flow. By contrast fluid flow along narrow grain boundaries is difficult, so that the local stresses will be greatest along these boundaries. Because of these preferred paths for fluid flow, deformation of polyphase materials is most likely nonhomogeneous. Devitrification increases the difficulty of fluid flow by increasing the effective grain boundary viscosity by a

factor of approximately 10 over that calculated for the glass in the annealed specimens. This increase in viscosity should increase the estimate of the grain boundary thickness by a factor of approximately two.

Turning now to solution precipitation as a means of liquid enhanced creep, two types of mechanisms have been suggested. In one, the grains of the solid are in firm contact and the driving forces for solution and precipitation result from the high stress that occur at contact points [22, 27]. The creep rate can then be limited either by the kinetics of solution and precipitation, or by the rate of transport from regions of high to regions of low stress, the transport processes being driven by the gradient of the chemical potential, and its dependence on pressure. These mechanisms were discounted in the present experiment because no evidence of intergranular contact was found in microstructural analyses of deformed specimens. If contact sites were present they would appear as well-defined regions of strain contrast, as has been reported by Lange et al. [29] in TEM studies of hot-pressed silicon nitride. Similar patterns of strain contrast due to intergranular contact have been observed in hot-pressed silicon nitride in our own laboratory [30]. In the glass-bonded aluminum oxide, however, no such strain contrast was observed at grain boundaries in the present study. Therefore, either the contact sites were not there, or they were so widely spaced that their observation would have been rare. In this section we assume that the grains were not in contact, and that each grain of solid was completely surrounded by glass.

When glass forms a continuous phase around the grains, then stress gradients within the glass result from the high viscosity of the glass, which resists the imposed forces and prevents the grains from touching.

Solution reprecipitation for this situation has been analyzed by a number of investigators [31-34], and creep equations similar to the following one by Rutter [33] have been reported for transport limited processes:

$$\dot{\epsilon} = 32 \sigma V C_0 D w / N_0 kT \rho d^3 \quad (6)$$

where V is the molar volume of the solid (Al_2O_3), C_0 is the concentration (mass/volume) of the diffusing species in the solution, D is the diffusivity, N_0 is Avogadro's constant, k is Boltzmann's constant and ρ is the density of the solid.

In our treatment of creep by solution precipitation, the diffusivity must be estimated in order to evaluate the creep rate. Usually, the Stokes-Einstein relation ($D = kT/6\eta r$) is used in solution precipitation theories to estimate the diffusivity in terms of the liquid viscosity, η , and the radius, r , of the diffusing species. Whereas the Stokes-Einstein relation works well for liquid metals and molten salts, problems are encountered in its application to liquids, such as glasses and polymeric melts, that have a network structure [37]. In these structures, most atoms diffuse through the network. By contrast viscous flow is determined primarily by the structure of the network, i.e. by breaking of network bonds, so that the two processes may not be closely related, and consequently, errors in estimating the diffusivity can be large [34, 35]. Thus, before using the Stokes-Einstein relation, its potential for error should be recognized and if possible the equation should be assessed on known sets of data.

In the present investigation the transport of aluminum ion, Al^{+3} , probably controls aluminum oxide diffusion, because its rate of diffusion is much less than that of oxygen, O^{-2} , in silicate melts [37,38]. To test the applicability of the Stokes-Einstein relation to Al^{+3} , experimental parameters for viscosity and diffusivity assembled by Cooper and Kingery [36] were used. At 1400 °C the diffusivity of Al^{+3} is $\sim 2.6 \times 10^{-7} \text{ cm}^2/\text{s}$, while the viscosity is 23.3 poise (2.33 Pa·s), from which an ionic radius of 0.02 nm is calculated. This value is about a factor of 2.5 smaller than that (0.05 nm) estimated by Pauling [39] from wave mechanics considerations. The diffusivity and the viscosity also appear to have similar temperature dependencies ($\Delta H = -272 \text{ kJ/mol}$ for diffusion and -229 kJ/mol for viscous flow). Based on this comparison, the Stokes-Einstein relation is expected to give an order-of-magnitude estimate for the diffusivity of Al^{+3} in the temperature range used for the present study.

Substituting the Stokes-Einstein equation into equation 6, the following relation is obtained for the creep rate:

$$\dot{\epsilon} = 32 \sigma V C_0 w / 6 N_0 \eta r \rho d^3 \quad (7)$$

Using appropriate experimental values ($V = 25.5 \times 10^{-6} \text{ m}^3/\text{mol}$; $C_0 = 0.625 \times 10^3 \text{ kg/m}^3$; $r = 0.02 \text{ nm}$; $\rho = 4 \times 10^3 \text{ kg/m}^3$) in equation 7, the relation between $\dot{\epsilon}$ and w is given by $\dot{\epsilon}/w = 8.7 \times 10^{-2} \text{ s}^{-1} \text{ m}^{-1}$, from which a grain boundary thickness of 34 nm is calculated for an initial applied stress of 60 MPa at a temperature of 1044 °C. This grain boundary thickness lies within the range of values observed in the present experiment. In view of the assumptions made in obtaining this number, the fact that this estimate of grain boundary thickness is an order of magnitude greater than that for

percolation for the same experimental parameters, cannot be considered significant. Within the accuracy of the models and the material property estimates, therefore, the solution precipitation and the percolation models of creep must be considered competitive.

Nucleation and growth of cavities within grain boundaries provides a third mechanism by which work-hardening resulting from the dilatant behavior of the polycrystalline solid can be relieved. Cavitation is commonly observed as a means of accommodation in metals and has been reported in a number of studies for ceramics tested in tension, bending and compression [3, 5, 12-15, 19]. Since homogeneous cavitation was not observed in the present study it must be concluded that cavity formation and growth did not play a major role during creep deformation. This conclusion is very different from that reached by Clarke [15], who found that high temperature deformation of glass bonded alumina was dominated by cavitation within the glass phase. The reasons for the difference between our results and Clarke's results are not fully understood at the present time, but may reside in differences in the composition and viscosity of the glasses used in the two studies. Although the two studies were conducted over roughly the same temperature range, the viscosity of the glass bonding phase in Clarke's study was approximately two orders of magnitude less than that in our own study. In fact, the viscosity of the glass used by Clarke was similar to that of the glass in the unannealed specimens in our study. Further studies are indicated to clarify the role of cavitation in the creep process, and the conditions under which cavitation occurs in two phase ceramics.

Although extensive cavity nucleation, of the type reported in the creep-rupture literature, was not observed in the present study, isolated and fairly widely spaced grain boundary delaminations were observed. The delaminations occurred at the tensile surface where the stresses were highest and where the surfaces were embrittled by extensive devitrification of glass at the grain boundaries. These delaminations form preferentially at two grain boundaries where, according to percolation theories of creep, the stresses are highest. These delaminations are probably the precursors of cracks that nucleate in the tensile surface of the specimen and grow to critical size during the course of the creep experiment. The contributions of grain boundary delaminations and their subsequent growth to failure are the subjects of a companion paper to be published by the authors on this material.

4.3 Creep and Creep-Rupture Phenomenology

Although the initial purpose of this study was to estimate the creep behavior of a two-phase ceramic from an analysis of the microstructure of the ceramic, the extensive collection of creep and creep-rupture data presented in this paper warrants some brief comment on the data and its comparison with other data of the same type. In this section discussion is limited to vitreous bonded oxides, including refractories, porcelains and glass ceramics, which are closest in structure to the material used in the present study.

4.3.1 Stress Exponent

The creep data collected in the present paper were found to fit the classical power law creep expression given by equation 1. Both the power law exponent, $n = 4.85$, and the apparent activation enthalpy, $\Delta H = 926$ kJ/mol, lie at the high end of values reported for creep processes. Literature values of n range from -1 to 6 depending on the material tested and the level of stress [6, 7, 21, 40, 41]. The value of n tends to increase as the stress is increased, but does not appear to depend on the sign of the applied stress: i.e. whether the applied stress is tensile or compressive [19]. In view of these comments, the value of n obtained in the present experiment is not unusual even though it lies at the high end of the range of values.

Since most theories of creep are linear in applied stress ($n = 1$) they cannot be used in unaltered form to explain non-linear aspects of creep, or creep-rupture. Most often, investigators have suggested cavitation, or microcrack formation as the primary explanation for a high creep exponent [3, 21]. As cavities are formed the applied stress is transferred from the cavitated to the uncavitated portion of the specimen, and the creep rate increases as a result of the both cavity nucleation and cavity growth. Since the rate of nucleation and growth of cavities is basically a non-linear function of applied stress [13], the creep process is also non-linear function of stress. Thus, Morrel and Ashbee [21], Lange et al. [3], Clarke [15], and others have used cavitation as a means of explaining the non-linear dependence of creep on stress.

In the present experiment, no evidence of cavitation at grain boundaries was obtained and therefore, it is difficult to explain the non-linear creep behavior by cavitation. Instead other time dependent

processes such as devitrification and premature termination of the creep process by fracture are probably responsible for the observations. The importance of crystallization or devitrification was first noted by Norton [6] in a study of the tensile creep of porcelain. Devitrification increases the effective viscosity of the grain boundary phase and hence increases the resistance of two phase material to creep deformation. Norton noted that when crystallization has sufficient time to occur, as when the applied loads are low, then the changes in the microstructure increase the amount of work hardening and reduce the apparent steady state creep rate. The converse is true at high loads, when creep is rapid and devitrification does not have sufficient time to occur. In this case, the apparent steady state creep rate is higher than would be determined from a linear dependence of creep rate on applied load.

In addition to the structural effects discussed above, premature termination of the creep process by specimen fracture can also play a role in establishing a high value of the creep exponent n . When crack nucleation and crack growth are strongly dependent on the applied stress, then the time to failure may depend on the applied stress in a way that is independent of the creep process. At high levels of applied load, failure is likely to occur in an early stage (i.e. stage 1) of the creep process, so that the creep rate will be greater than that obtained if creep were not interrupted by fracture. By contrast, failure at low levels of applied stress is likely to occur much later in the creep process (i.e. stage 2) so that the two measured creep rates will not correspond to the same portion of the creep curve. The net effect of representing such a set of data by the equation 1 is to obtain a non-linear dependence of creep rate on applied stress.

In the present experiment both devitrification and premature specimen failure played a role in establishing the high value of n . Creep occurs initially in a "crack-free" condition; the specimen deforms, work hardens, and then at some point in time, grain boundary delamination results in crack formation and eventually in specimen failure. The minimum creep rate achieved during each run depends both on the devitrification process, and on the crack nucleation and growth process, both of which lead to a non-linear dependence of the creep rate on applied stress.

4.3.2 Apparent Activation Enthalpy

Based on the discussions in sections 4.1 and 4.2, the temperature dependence of the creep rate might be expected to be determined primarily by the glass viscosity, and the dependence of the glass viscosity on composition. For the glass compositions given in Table 2, the apparent activation enthalpy for viscous flow is estimated to be ~ 330 kJ/mol. This estimate can be increased somewhat by taking into account changes in glass composition that result from changes in temperature. The magnitude of this effect is inferred from the net change in composition due to annealing. From figure 13 annealing results in approximately two orders of magnitude increase in viscosity, which should increase the estimated value of the apparent activation enthalpy for viscous flow from ~ 330 kJ/mol to ~ 550 kJ/mol, a value that is clearly not enough to explain the high apparent activation enthalpy, 926 kJ/mol, for creep in the present experiment.

This lack of agreement between the estimated and measured activation enthalpies clearly indicate that factors other than glass viscosity play a role in establishing the temperature dependence of the creep process.

Grain boundary devitrification may be one such factor, since it is known to occur during creep and should have a dramatic influence on the effective viscosity of the grain boundaries. If grain boundary devitrification is important, then the enthalpy of solution of grain boundary phases will contribute to the apparent activation enthalpy of the creep process. The importance of the heat of solution to the creep process has been suggested by Raj and Morgan [42] for a number of high temperature processes in hot-pressed silicon nitride and has been applied by Wang and Raj [43] to explain the high activation energies (~ 700 kJ/mol) for the creep of glass ceramics. The heat of solution is also important when solution precipitation occurs during creep. Further studies will be required to fully elucidate the importance of grain-boundary devitrification to the creep of multiphase ceramics.

4.3.3 Creep Rupture

The creep-rupture data shown in figures 10-11 were found to fit the modified Monkman-Grant relation given by equation 3. This equation was selected to represent the creep-rupture data because theoretical work by Evans and Blumenthal [44, 45] have been represented in this format. Furthermore, the creep-rupture experiments presented by Johnson et al. [46] on direct bonded aluminum oxide have been shown to fit this type of equation. In this regard, it may be significant that the stress exponent of $t \dot{\epsilon}$ obtained by Johnson et al., -6 ± 2 , is close to the value obtained in our own experiments, -4.2 ± 0.9 , despite the great difference in the microstructure of two materials.

Most theories that have been developed to describe the creep rupture of polycrystalline systems assume a rather simple microstructure. For two phase ceramics, the microstructure is usually viewed as a collection of equiaxed grains separated by a viscous fluid [13, 44, 47]. For this type of material, models of crack nucleation, crack coalescence and crack growth have been developed. Generally, these predict a small dependence of $t \dot{\epsilon}$ on applied stress. To be more specific, $t \dot{\epsilon}$ for nucleation controlled creep-rupture is predicted to be stress independent. In view of this prediction, crack nucleation can not be considered rate limiting in the present study. For crack growth controlled fracture, $t \dot{\epsilon}$ is proportional to σ^{n-p} , where n is the stress exponent for creep and p is the stress exponent for crack growth.^{6/} From theoretical considerations, Tsai and Raj [47] suggest $p \leq 4$ for crack propagation in two phase materials. Combining $p = 4$ with the value of $n = 4.85$, measured in the present paper, yields a value for the stress exponent of $t \dot{\epsilon}$, 0.85, which is not consistent with the experimental results of the present paper. Thus, crack growth alone, cannot be used to rationalize the present set of creep rupture data. The remaining theory of creep rupture, the coalescence theory, is not sufficiently developed to be compared with the present set of data [49].

From the above discussion we must conclude that the theories of two phase creep fracture that have been developed to date are not able to explain the stress dependence of $t \dot{\epsilon}$ for the current set of data. In

^{6/} This relation is obtained by assuming that creep and crack growth are independent processes, so that the time-to-failure, t , is given by $t = B s P^{-2} \sigma^{-P}$ [48] and the creep rate is given by equation 1. By combining equation 1 with the equation for t , the relation between $t \dot{\epsilon}$ and σ is obtained. The idea of simultaneous creep and crack growth was first presented by Lange [50].

view of the complexity of the material used in the present investigation, this finding is not, perhaps, surprising. Alteration of the material by stress-dependent devitrification undoubtedly plays a role in both the nucleation and crack growth process. Additional theoretical work is clearly needed to model the effect of devitrification on crack growth and crack nucleation. In addition, microscopic studies will be needed to elucidate the importance of nucleation and of subcritical crack growth to the failure process.

5.0 Summary

This paper presents the results of an investigation of the creep and creep rupture of a commercial grade of glass bonded aluminum oxide. Analytical electron microscopy was used to evaluate the chemical composition of glass at the grain boundaries, and the variation composition of the glass with exposure to elevated temperature and creep deformation. The type and degree of precipitation that occurred during creep clearly appeared to be stress dependent. The glass at grain boundaries in the tensile cross-section of the test specimens was approximately 3 times as viscous as the glass in the compressive section of the test specimen. This finding is consistent with the pattern of devitrification observed in these specimens. Devitrification was heaviest at the tensile surface, which suggests an embrittlement of the surface compared to rest of the specimen cross section.

The viscosity of the glass at the grain boundaries was estimated from its chemical composition and was used to compare the measured creep rates in the present study with models that have been developed to describe

creep in two phase ceramics. The creep mechanism that most closely represent our results are the viscous flow (percolation) theory first and solution precipitation both of which were suggested by a number of authors. Cavitation was discounted because of the lack of evidence for homogeneous cavitation in the tensile portions of the bend specimens. During later stages of creep, however, grain-boundary delaminations at the tensile surfaces are believed to be the origins of cracks that are eventually responsible for the failure of these specimens. Additional studies were recommended to clarify the relative importance of crack nucleation and crack growth to the creep-rupture process.

Acknowledgements: This work was jointly supported by the Department of Energy (Fossil Energy Program) and by the Department of Defense (Air Force Office of Scientific Research).

REFERENCES

1. Ceramics for High-Performance Applications III, Reliability, E.M. Lence, R.N. Katz and J.J. Burke, eds., Plenum Press, New York (1983).
2. Proc. of the Educational Symposium on Refractories in Slagging Environments, published in: Ceramic Engineering and Science Proceedings, Vol. 2 [11-12] (1981).
3. F.F. Lange, B.I. Davis and D.R. Clarke, "Compressive Creep of $\text{Si}_3\text{N}_4/\text{MgO}$ Alloys: Pt. 1 Effect of Composition," J. Mater. Sci. 15, 601-10 (1980).
4. F.F. Lange, B.I. Davis and D.R. Clarke, "Compressive Creep of $\text{Si}_3\text{N}_4/\text{MgO}$ Alloys: Pt. 3 Effect of Oxidation Induced Compositional Change," J. Mater. Sci. 15, 616-18 (1980).

5. R. Kossowsky, D.G. Miller and E.S. Diaz, "Tensile and Creep Strengths of Hot-Pressed Si_3N_4 ," J. Mater. Sci. 10, 983-97 (1975).
6. F.H. Norton, "The Flow of Ceramic Bodies at Elevated Temperatures," J. Am. Ceram. Soc. 19 [5], 129-34 (1936).
7. C.D. Hulse and J.A. Pask "Analysis of Deformation of a Fireclay Refractory," J. Am. Ceram. Soc. 49 [6], 312-18 (1966).
8. K. James and K.H.G. Ashbee, "Plasticity of Hot Glass-Ceramics," Prog. Mat. Sci. 21, 1-60 (1975).
9. G.W. Hollenberg, G.R. Terwilliger and R.S. Gordon, "Calculation of Stress and Strains in Four-Point Bending Creep Tests,," J. Am. Ceram. Soc. 54, 196-199 (1971).
10. G. Quinn and R. Katz, "Stepped Temperature Stress-Rupture Testing of Silicon Based Ceramics," Am. Ceram. Soc. Bull., 57 [11] 1057-58 (1978).
11. G. Cliff and G.H. Lorimer, "The Quantitative Analysis of Thin Specimens," J. Microscopy, 103, 203-207 (1975).
12. M.H. Lewis, B.S.B. Karunaratne, J. Meridith and C. Pickering, pp. 365-79 in Creep and Fracture of Engineering Materials and Structures, B. Whilshire and D.R.J. Owens, eds. Pineridge Press, Swansea (1981).
13. J.E. Marion, A.G. Evans, M.D. Drory and D.R. Clarke, "High Temperature Failure Initiation in Liquid Phase Sintered Materials," Acta Met. 31 [10], 1445-57 (1983).
14. N.J. Tighe, S.M. Wiederhorn, T.-J. Chuang and C.L. McDaniel, "Creep Cavitation and Crack Growth in Silicon Nitride," pp. 587-604 in Deformation of Ceramic Materials II, Materials Science Research, Vol. 18, R.E. Tressler and R.C. Bradt, eds. Plenum Press, New York (1984).
15. D.R. Clarke, "High Temperature Deformation of a Polycrystalline Alumina Containing an Intergranular Glass Phase," J. Mat. Sci., in press.
16. F.C. Monkman and N.J. Grant, "An Empirical Relationship between Rupture Life and Minimum Creep Rate in Creep-Rupture Tests," Proc. ASTM 56, 593-620 (1956).
17. R.W. Hertzberg, Deformation and Fracture Mechanics of Engineering Materials, John Wiley & Sons, New York (1976).
18. G. Urbain, F. Cambier, M.Deletter and M.R. Anseau, "Viscosity of Silicate Melts," Trans. J. Br. Ceram. Soc. 80, 139-41 (1981).

19. R.C. Streeter, E.K. Diehl and H.H. Schobert, "Measurement and Prediction of Low-Rank Coal Slag Viscosity," Am. Chem. Soc. Fuel Division Reprints, 28 [4], 174-195 (1983).
20. J.R. Hutchins, III and R.V. Harrington, "Glass," pp. 533-604 in Kirk-Othmer: Encyclopedia of Chemical Technology, 2nd Edition, V. 10, John Wiley & Sons Inc., New York (1966).
21. R. Morrell and K.H.G. Ashbee, "High Temperature Creep of Lithium Zinc Silicate Glass Ceramics: Pt 1. General Behavior and Creep Mechanisms," J. Mater. Sci. 8, 1253-70 (1973).
22. G.M. Pharr and M.F. Ashby, "On Creep Enhanced by a Liquid Phase," Acta Met. 31, 129-38 (1983).
23. F.F. Lange, "Non-Elastic Deformation of Polycrystals with a Liquid Boundary Phase," pp. 361-381 in Deformation of Ceramic Materials, R.C. Bradt and R.E. Tressler, eds. Plenum Press, New York (1975).
24. O. Reynolds, "On the Dilatancy of Media Composed of Rigid Particles in Contact, with Experimental Illustrations," Phil. Mag. 20, 469-81 (1885).
25. F.C. Frank, "On Dilatancy in Relation to Seismic Sources," Rev. Geophysics, 3, 485 (1965).
26. D.C. Drucker, "Engineering and Continuum Aspects of High-Strength Materials," pp. 795-833 in High Strength Materials, V.F. Zackay, ed., John Wiley and Sons, Inc., New York (1965).
27. R. Raj, "Creep in Polycrystalline Aggregates by Matter Transport Through a Liquid Phase," J. Geophys. Res. 87 [B6], 4731-39 (1982).
28. R. Raj and C.K. Chyung, "Solution-Precipitation Creep in Glass Ceramics," Acta Met. 29, 159-66 (1981).
29. F.F. Lange, D.R. Clarke and B.I. Davis, "Compressive Creep of $\text{Si}_3\text{N}_4/\text{MgO}$ Alloys: Part 2 Source of Viscoelastic Effect," J. Mater. Sci. 15, 611-15 (1980).
30. N.J. Tighe, unpublished data.
31. D.W. Durney, "Solution-transfer, an Important Geological Deformation Mechanism," Nature, 235, 315-16 (1972).
32. D.W. Durney, "Pressure Solution and Crystallization Deformation," Phil. Trans. R. Soc. A283, 229-40 (1976).
33. E.H. Rutter, "The Kinetics of Rock Deformation by Pressure Solution," Phil. Trans. R. Soc. Lond. A283, 203-219 (1976).
34. R.L. Stocker and M.F. Ashby, "On the Rheology of the Upper Mantle," Rev. Geophys. and Space Phys. 11, 391-421 (1973).

35. E.T. Turkdogan, *Physicochemical Properties of Molten Slags and Glasses*, The Metals Society, London (1983).
36. R.H. Doremus, "Diffusion in Non-Crystalline Silicates," pp. 1-71 in *Modern Aspects of the Vitreous State*, Vol. 2, J.D. Mackenzie, ed., Butterworths, London (1962).
37. R. Terai and R. Hayanik, "Ionic Diffusion in Glasses," *J. Non-Cryst. Solids*, 18, 217-64 (1975).
38. A.R. Cooper, Jr. and W.D. Kingery, "Dissolution in Ceramic Systems: I. Molecular Diffusion, Natural Convection, and Force Convection Studies of Sapphire Dissolution in Calcium Aluminum Silicate," *J. Am. Ceram. Soc.* 47 [1], 37-43 (1964).
39. L. Pauling, *Nature of the Chemical Bond*, 3rd ed., Cornell University Press, Ithaca (1960).
40. F.H. Clews, H.M. Richardson and A.T. Green, "The Behavior of Refractory Materials under Stress at High Temperatures," *Trans. Brit. Ceram. Soc.* 15, 161-76 (1945).
41. S.E. Bold and G.W. Groves, "Tensile Creep and High-Temperature Fracture in a $\text{Li}_2\text{O}-\text{Al}_2\text{O}_3-4\text{SiO}_2$ Glass-Ceramic," *J. Mater. Sci.* 13, 611-19 (1978).
42. R. Raj and P.E.D. Morgan, "Activation Energies for Densification, Creep and Grain-Boundary Sliding in Nitrogen Ceramics," *J. Am. Ceram. Soc.* 64 [10], C-143-C-145 (1981).
43. J.-G. Wang and R. Raj, "Mechanisms of Superplastic Flow in a Fine-Grained Ceramic Containing some Liquid Phase," *J. Am. Ceram. Soc.* 67[63], 399-409 (1984).
44. A.G. Evans and W. Blumenthal, "High Temperature Failure in Ceramics," pp. 423-48 in *Fracture Mechanics of Ceramics*, Vol. 6, R.C. Bradt, A.G. Evans, D.P.H. Hasselman and F.F. Lange, eds., Plenum Press, New York (1983).
45. A.G. Evans and W. Blumenthal, "High Temperature Failure Mechanisms in Ceramic Polycrystals," pp. 487-505 in *Deformation of Ceramic Materials II: Materials Science Research*, Vol. 18, R.E. Tressler and R.C. Bradt, eds., Plenum Press, New York (1984).
46. S.M. Johnson, B.J. Dalgleish, and A.G. Evans, "The High Temperature Failure of Polycrystalline Alumina, Part III: High Temperature Time-to-Failure," *J. Am. Ceram. Soc.* 67, 759-63 (1984).
47. R.L. Tsai and R. Raj, "Creep Fracture in Ceramics Containing Small Amounts of a Liquid Phase," *Acta Met.* 30, 1043-58 (1982).
48. J.E. Ritter, Jr., "Engineering Design and Fatigue Failure of Brittle Materials," pp. 667-86 in *Fracture Mechanics of Ceramics*, Vol. 4, R.C. Bradt, D.P.H. Hasselman and F.F. Lange, eds., Plenum Press, New York (1978).

49. A.G. Evans and A. Rana, "High Temperature Failure Mechanisms in Ceramics, "Acta Met. 28, 129-41 (1980).
50. F.F. Lange, "Interrelations Between Creep and Slow Crack Growth for Tensile Loading Conditions," Int. J. Fracture, 12, 739-44 (1976).

Table 1. Glasses Used for Calibration Purposes in the Present Study

Glass	Component (wt fraction)							
	SiO ₂	Al ₂ O ₃	B ₂ O ₃	FeO	Na ₂ O	K ₂ O	MgO	CaO
Soda-Lime Silica	0.72	0.02	-	-	0.14	0.01	0.04	0.07
K-412*	0.45	0.09	-	0.10	-	-	0.19	0.15
C1720#	0.62	0.17	0.05	-	0.01	-	0.07	0.08
C0080#	0.73	0.01	-	-	0.17	-	0.04	0.05

* NBS Standard Reference Material, SRM 470. Compositions in the standard are reported to better than two significant figures.

Corning Glass Co. See ref. 20 for the compositions. The use of this glass does not imply endorsement by the National Bureau of Standards.

Table 2. Chemical Analysis of Residual Glass at Grain Boundaries of AD-96 Aluminum Oxide

Treatment	Composition (Mol %)				
	Na ₂ O	MgO	CaO	Al ₂ O ₃	SiO ₂
As-Received	5.03 (1.25)*	11.21 (1.63)	2.77 (0.37)	16.11 (0.91)	64.88 (2.33)
Annealed [#] (Unstressed Mtl)	5.05 (0.86)	3.37 (0.35)	3.72 (0.44)	16.09 (0.76)	71.78 (1.80)
Annealed (100 μm Thin Section)	4.41 (1.85)	2.50 (0.76)	0.66 (0.16)	14.60 (0.96)	77.78 (3.13)
Tensile Surface	3.52 (1.44)	2.74 (0.39)	0.65 (0.12)	13.42 (0.45)	79.67 (1.49)
Tensile Surface	3.66 (1.09)	2.62 (0.04)	0.92 (0.17)	14.13 (0.63)	78.52 (1.65)
Compressive Surface	3.61 (0.67)	3.02 (0.65)	0.92 (0.13)	14.70 (0.47)	77.75 (1.42)
Tensile Section	2.83 (1.73)	3.03 (0.82)	1.97 (0.55)	15.26 (0.90)	76.96 (2.36)
Compressive Section	3.24 (1.78)	3.31 (0.72)	3.44 (0.40)	16.48 (1.17)	73.59 (2.46)

* The standard deviation of each measurement is given in parenthesis.

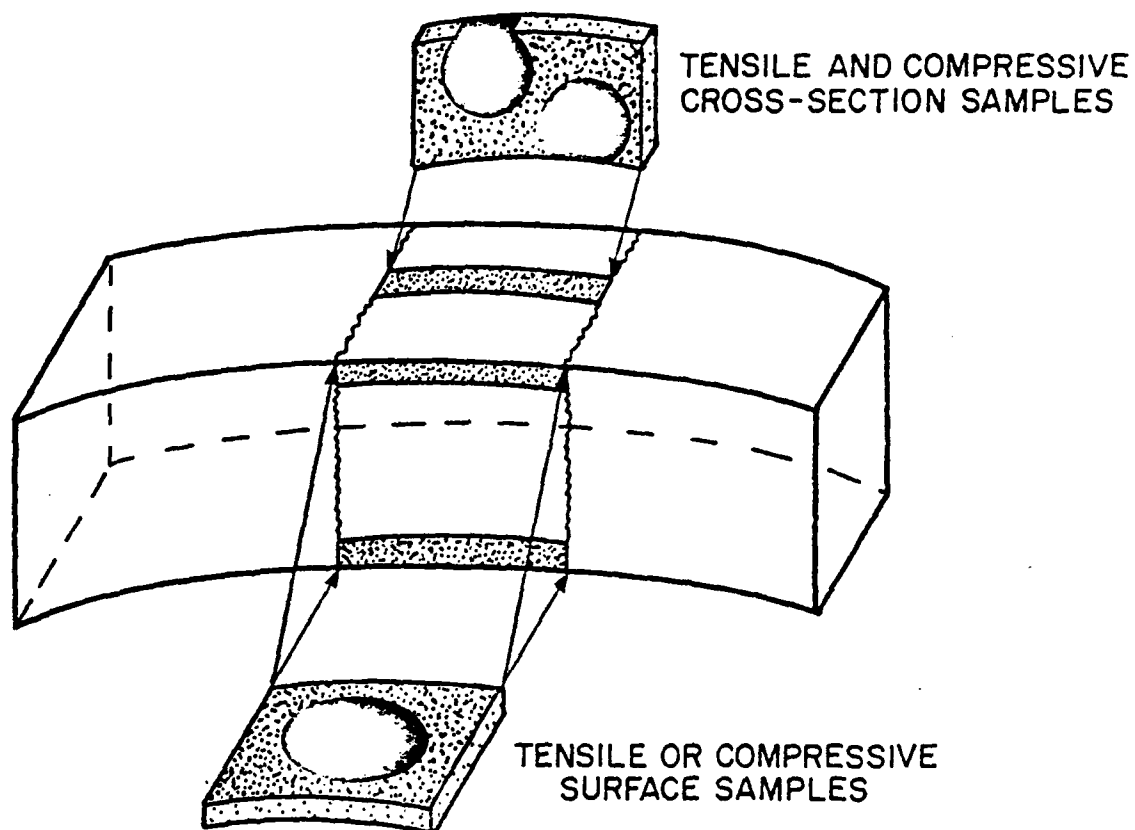
[#] Annealed for 96 hours at 1044°C, then subjected to creep for ~50 hours at an initial applied stress of 60 MPa. The unstressed material was taken from the end of the specimen.

Table 3. Summary of Creep-Rupture Data*

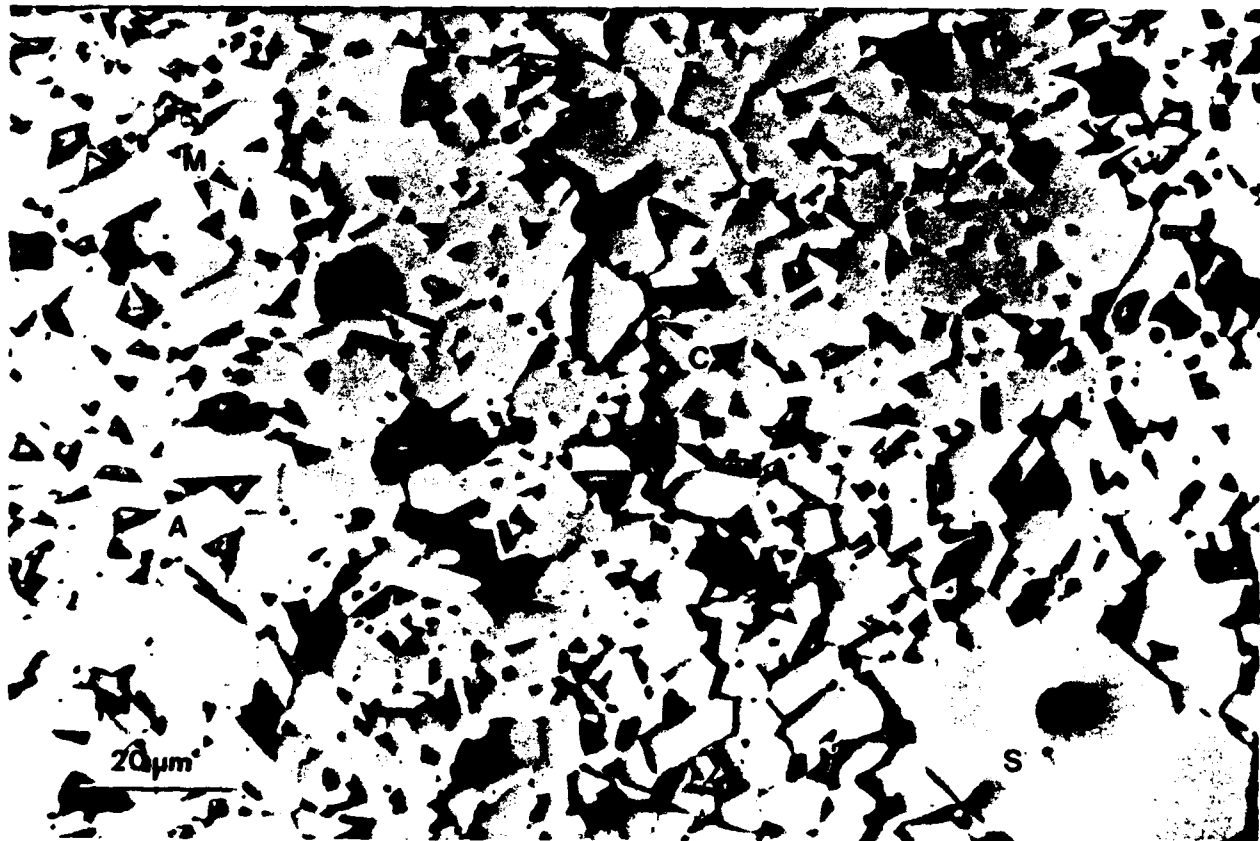
ln B	a	m	$\Delta H'$ (kJ/mol)	Standard Deviation of Fit	Degrees of Freedom
-7.95 (0.16)**	1 (assumed)	0 (assumed)	0 (assumed)	0.71	20
-8.97 (0.13)	1.1 (0.1)	0 (assumed)	0 (assumed)	0.72	19
-7.6 (3.6)	1 (assumed)	-4.2 (0.56)	195 (54.0)	0.334	18
-8.0 (7.9)	1.0 (0.1)	-4.2 (0.94)	200 (141.3)	0.344	17

* Data fit to the logarithmic form of equation 3:
 $\ln t = \ln B - a \ln \dot{\epsilon} + m \ln \sigma - \Delta H/RT$.

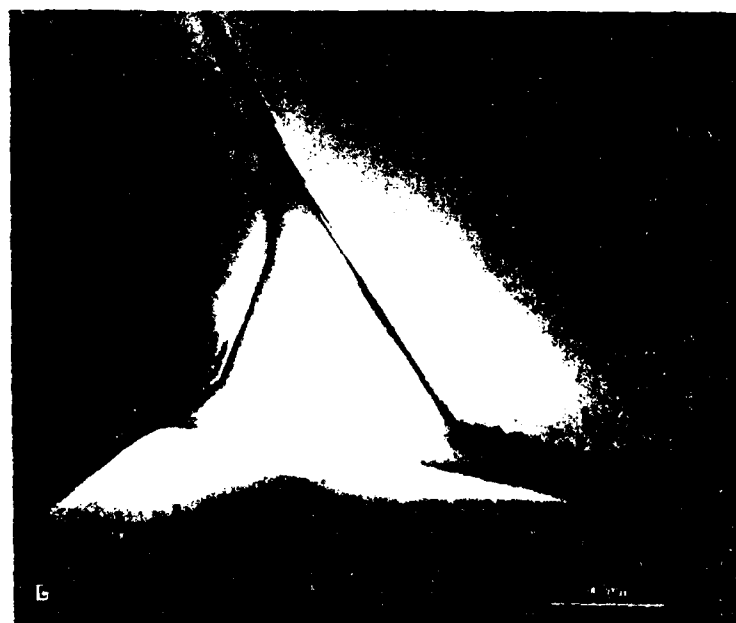
** Standard deviation of the constants.



1. Schematic diagram of bend bar showing regions from which thin sections were prepared for examination by transmission electron microscopy.



2. Light micrograph of longitudinal cross-section from creep sample. Relief polishing distinguishes intergranular phase (M) from aluminum oxide grains (A) and abnormally large spinel grains (S). Also evident are large pores, inherent to the material. Arrow indicates tensile creep crack that extends part way through sample. Note crack path is entirely intergranular.



3. TEM illustrating microstructure of vitreous bonded alumina in as-received condition. (a) Representative view showing non-uniform morphology of aluminum oxide grains and glassy binder phase at triple junctions. (b) Enlarged view of structureless glassy phase at triple junction and between widely separated grains. Surface faceting of aluminum oxide grains evident in (b) was characteristic feature of vitreous bonded material.



4. TEM: (a) Discrete crystallites of magnesio-alumino-silicate phases (see text for description) produced within multi-grain junction after prolonged heat treatment at 1050°C. Nature and extent of crystallization typifies partial devitrification of glassy binder phase that occurs within interior of bulk samples. (b) Fully crystallized intergranular structure typically produced within near surface regions after similar heat treatment. More complete devitrification is related to additional formation of intermediate plagioclase. As described in text, (a) is also typical of compressive subsurface regions and (b) typical of tensile subsurface regions after flexural creep.



5. TEM: Examples of crystallized grain boundary structures, invariably intermediate plagioclase, produced within tensile regions of flexural creep samples.



6. (a) SEM illustrating cavitation at grain boundaries and triple junctions in vicinity of developing creep crack on tensile surface.
 (b) TEM showing plate-like cavities at inclined grain boundary after creep deformation. Formation and growth of such cavities is considered responsible for intergranular creep crack extension.

AD-A159 202

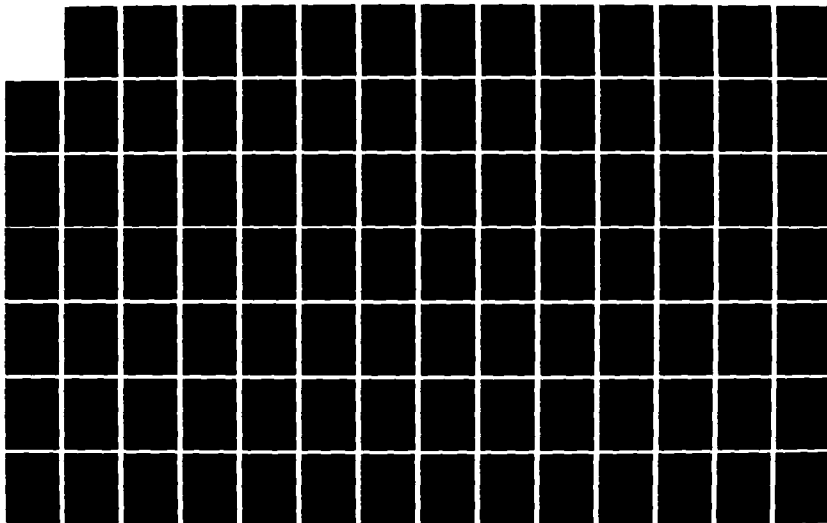
STRUCTURAL RELIABILITY OF BRITTLE MATERIALS AT HIGH
TEMPERATURES. (U) NATIONAL BUREAU OF STANDARDS

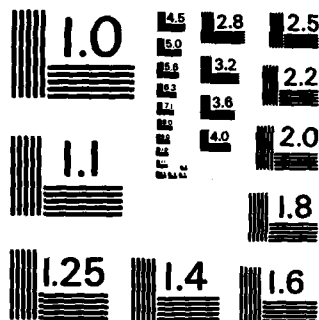
GAITHERSBURG MD INORGANIC MATERI..

UNCLASSIFIED S M WIEDERHORN ET AL. 31 DEC 84

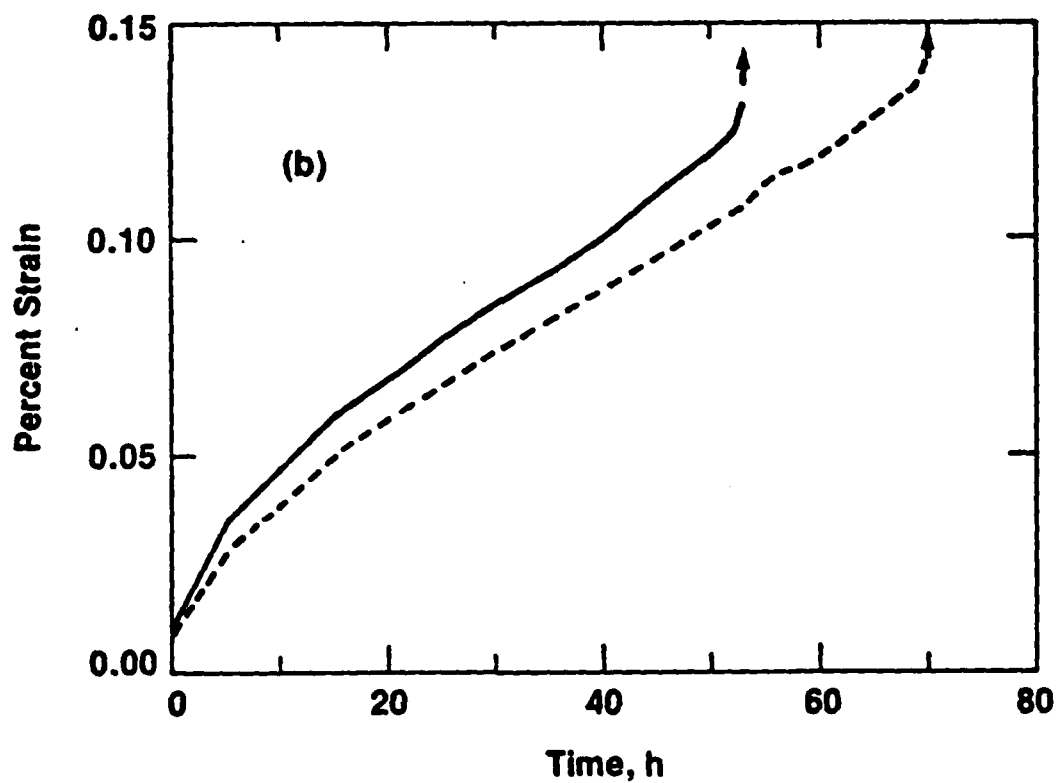
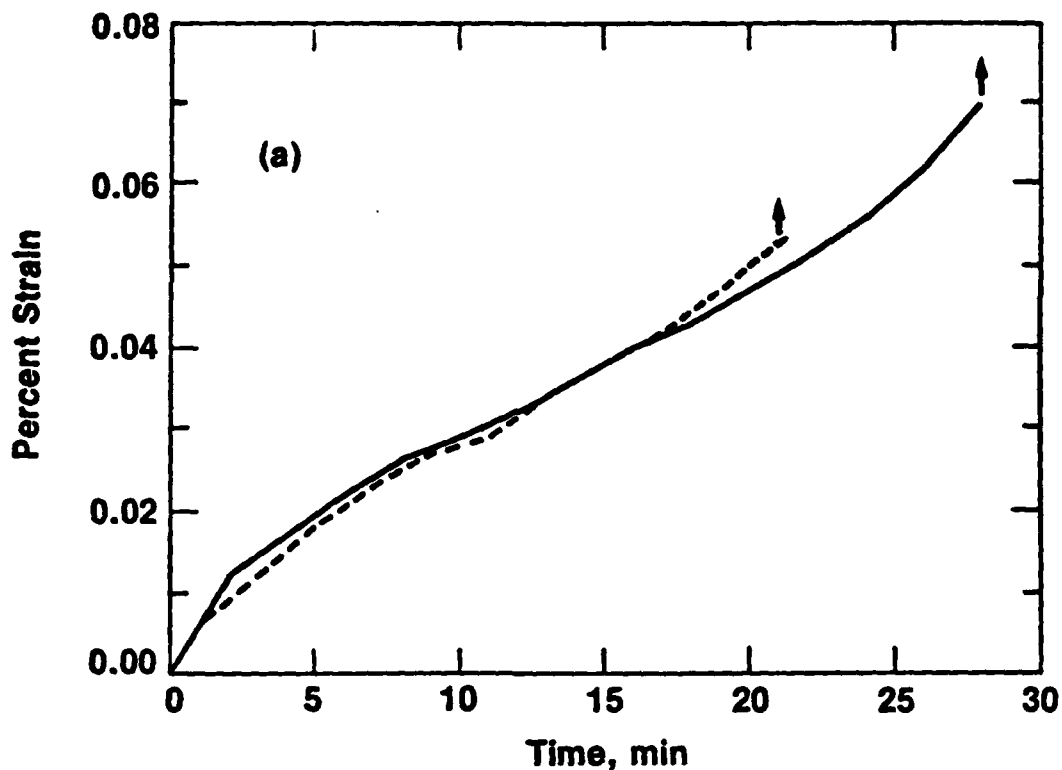
F/G 15/7

ML

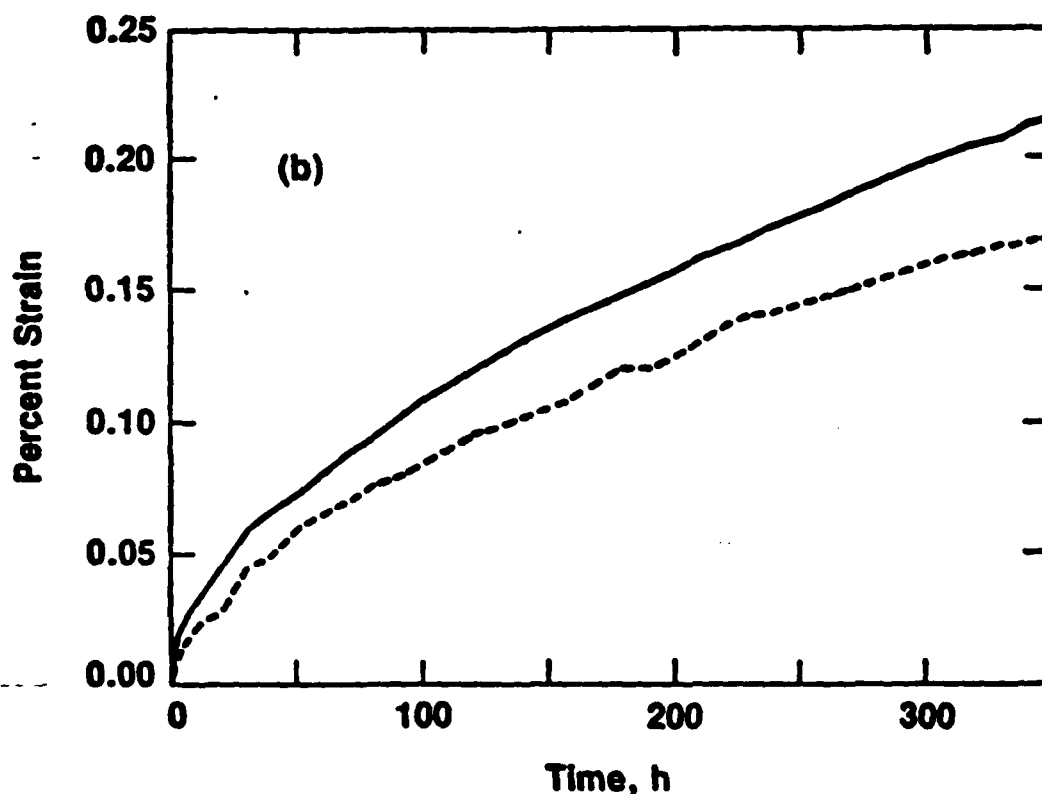
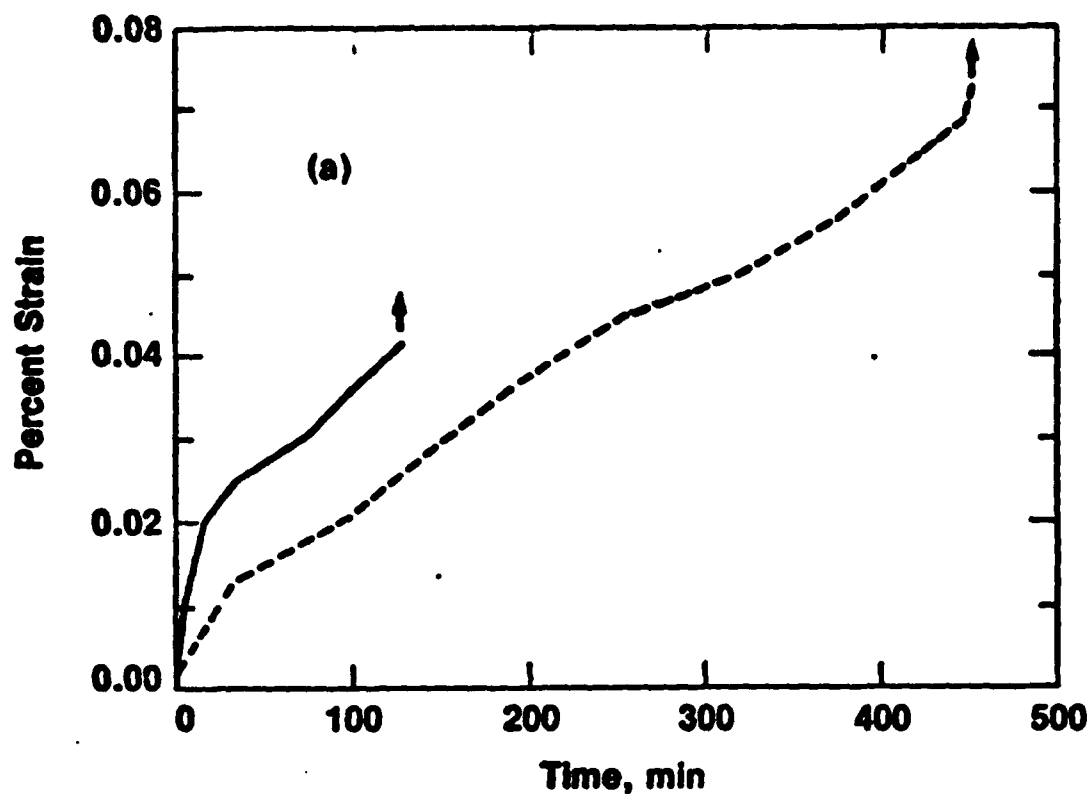




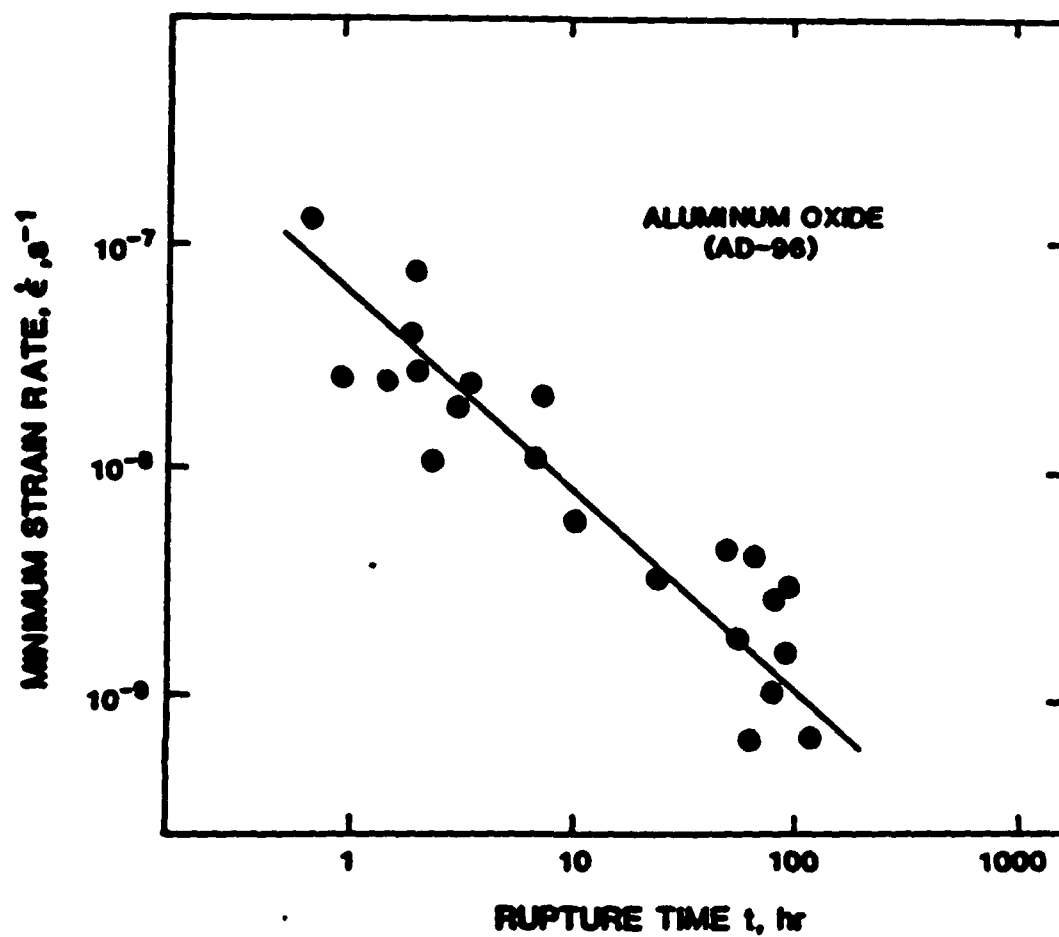
MICROCOPY RESOLUTION TEST CHART
NATIONAL BUREAU OF STANDARDS-1963-A



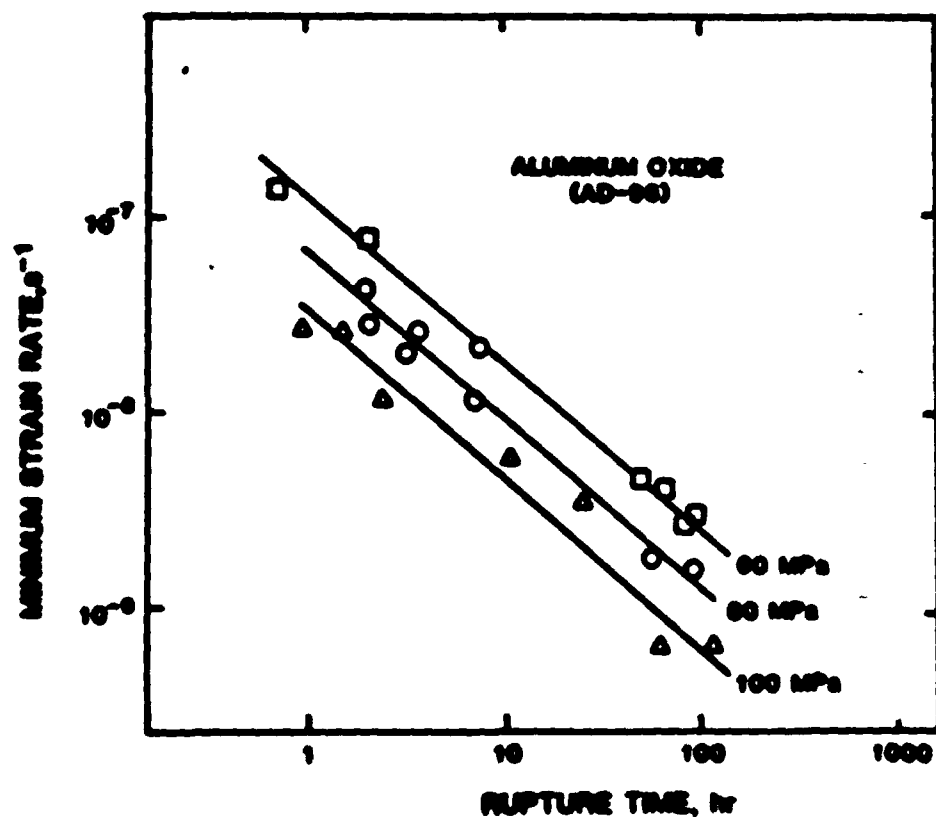
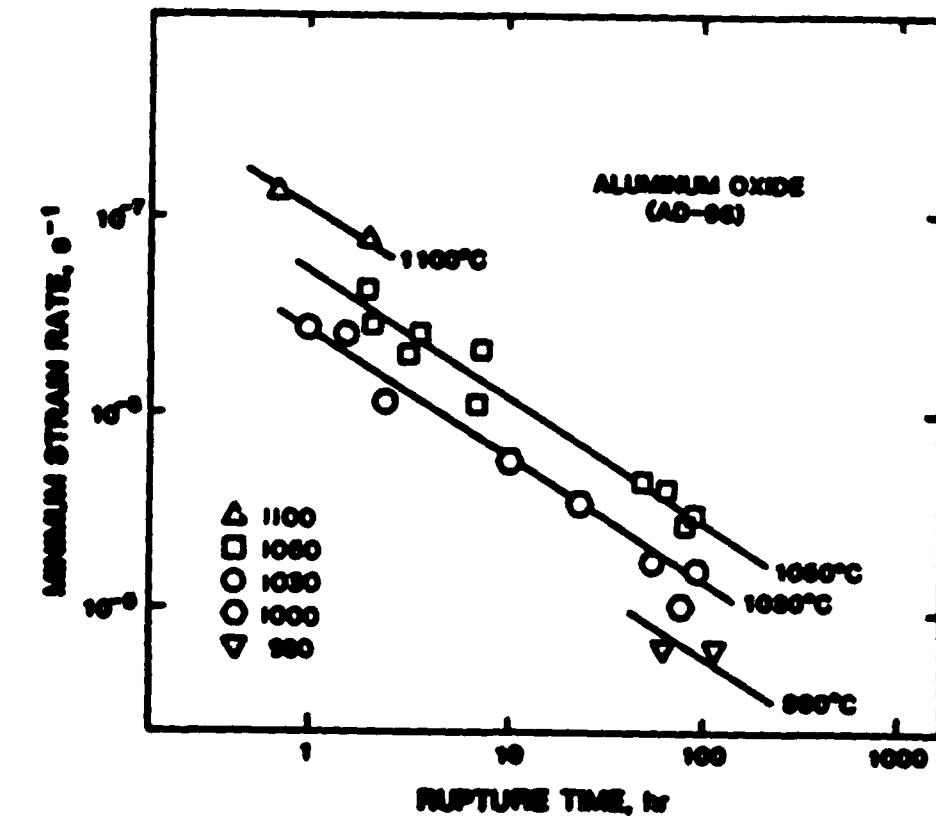
7. Creep of AD-96 alumina under an applied stress of 60 MPa at 1044°C:
 (a) No prior annealing. Note that failure occurs within 30 minutes of initial load application for both specimens, (b) Specimen annealed for 96 hours at 1044°C prior to testing. Annealing results in an approximate two hundred-fold increase in specimen lifetime primarily as a consequence of grain boundary devitrification.



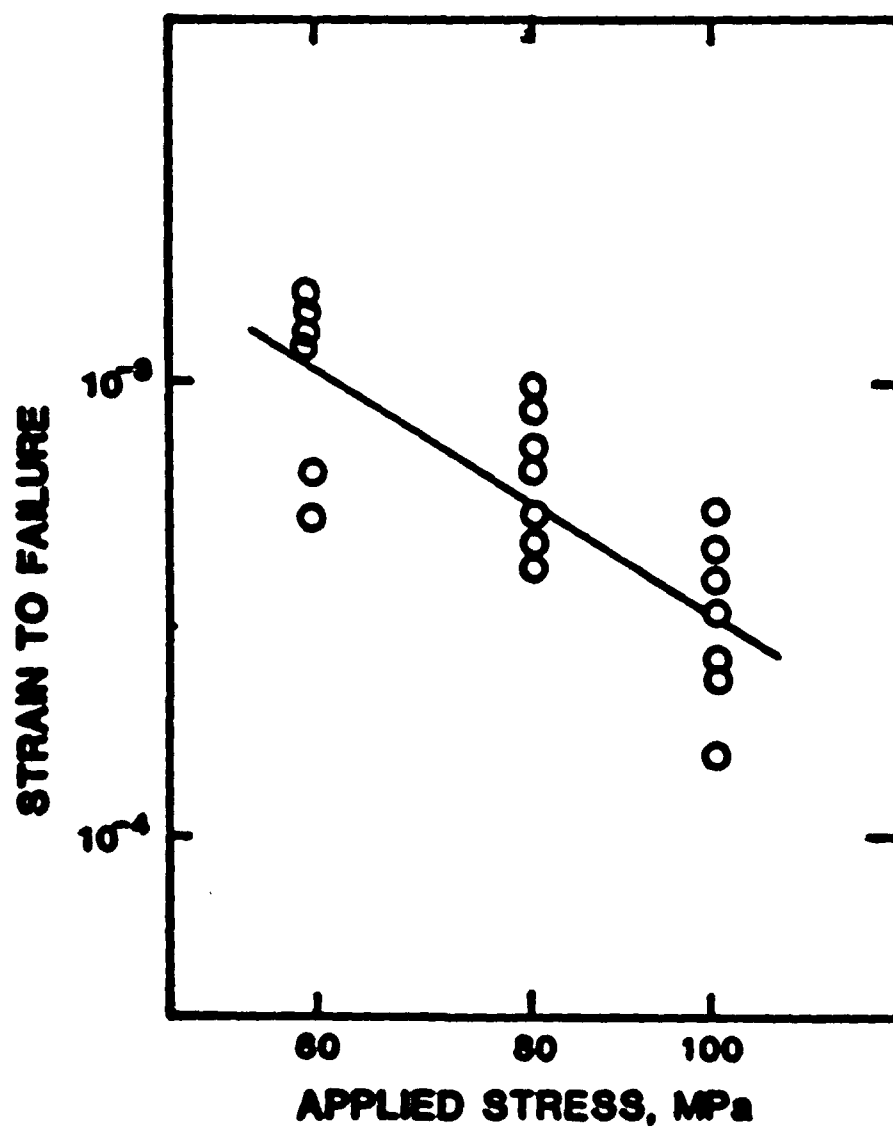
8. Comparison of short and long term creep of AD-96 alumina at 1044°C: (a) 80 MPa initial applied load, (b) 40 MPa initial applied load. In neither creep measurement, could a distinct steady state region be identified. This is particularly true for the long term runs (b), which suggest continual work hardening. The upper curve in (b) was in an advanced state of fracture and yet gave no indication of stage 3 behavior. In the other creep curves of figure 6 and 8, the initial and final stages of creep tend to overlap.



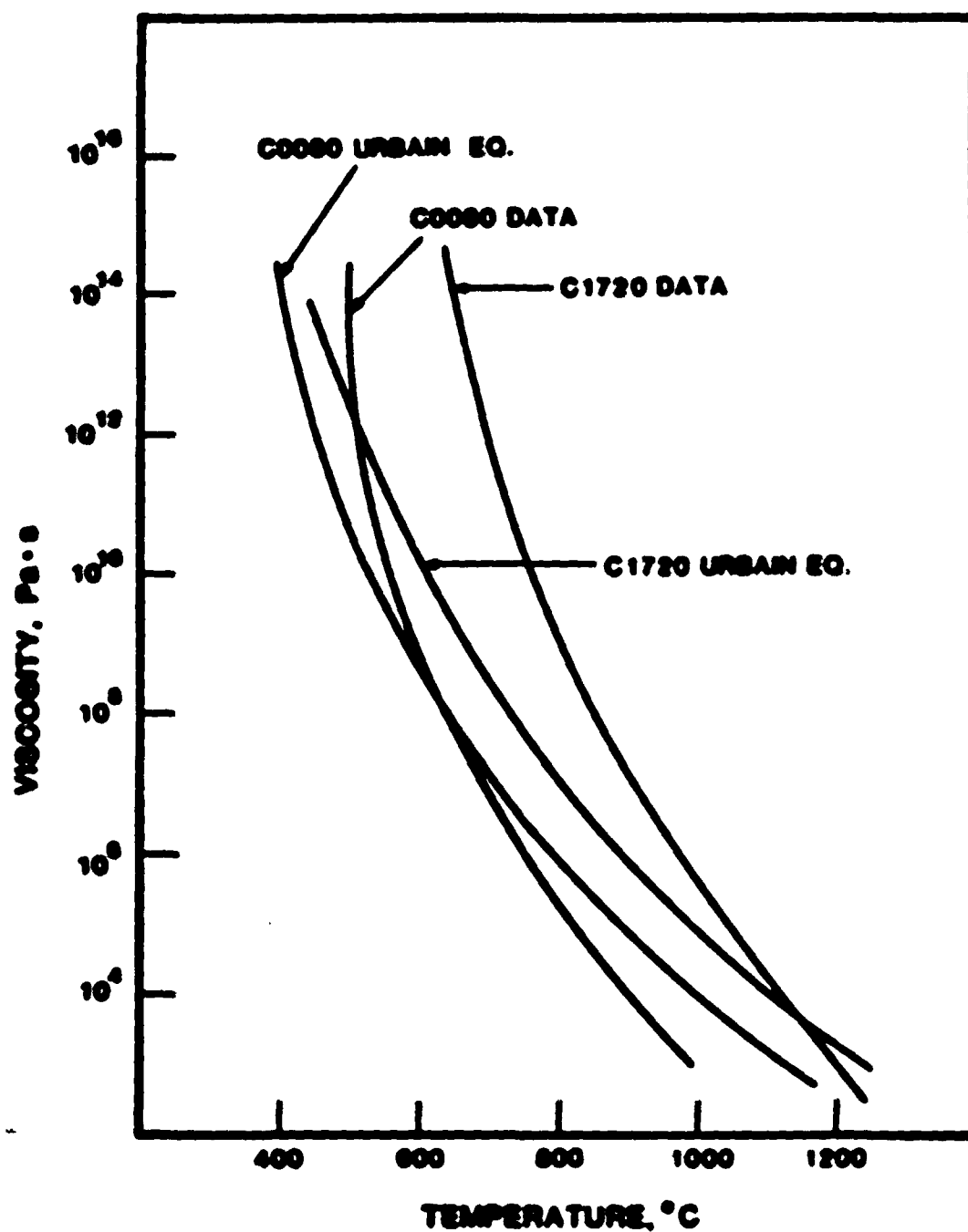
9. Creep-rupture data fit to a Monkman-Grant type of plot.



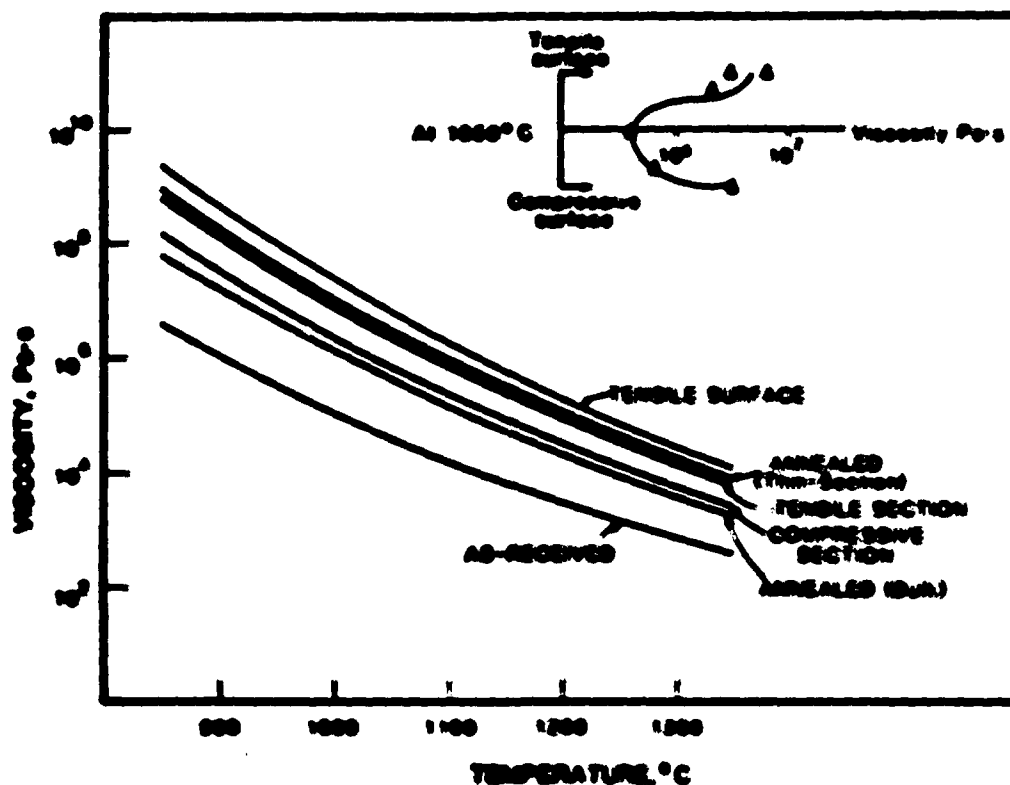
10. Creep-rupture data plotted as in figure 10, but identifying points of either: (a) constant temperature, or (b) constant applied stress.



11. Strain to failure as a function of initial applied stress.



12. Viscosity of two commercial glasses compared with viscosities calculated from the Urbain equations.



13. Calculated viscosities of glass composition given in Table 3. The insert shows how the glass viscosity changes from the tensile to the compressive cross-section of the bend bars, at a temperature of 1044°C .

ESTIMATION OF POWER-LAW CREEP PARAMETERS FROM BEND TEST DATA

by

**Tse-jer Chuang
Center for Materials Science
National Bureau of Standards
Gaithersburg, MD 20899**

OPICE PAGE 11 PLANT

ABSTRACT

Power-law creep parameters of brittle ceramic materials are commonly deduced from load-point displacement data generated by four-point bend experiments, under the assumption that tensile and compressive behaviors obey the same constitutive law. However, because of microcracking and cavitation, it is now well recognized that this premise may not always be valid. The present paper presents an analysis which takes the differences into account. Governing equations are first derived for the location of the neutral axis of a beam under bending which does not in general pass through the centroid of the cross section and for the creep response in terms of both curvature rate and load-point displacement rate as functions of the applied moment and power-law creep parameters. Numerical solutions are obtained for any given set of material constants over a wide range of applied moments. It is shown from the plots of creep response versus applied moment on a logarithmic scale that even linear curves over a narrow range of applied moment do not necessarily imply identical stress exponents and that nonlinear curves (concave down) signify a profound difference in stress exponent between tension and compression. An example of applying the present analysis to a set of load-point displacement data on glass-ceramic beam specimens tested at 1100°C is given. The results show that the conventional method over/underestimates the creep rates in compression/tension by two orders of magnitude, indicating a need of using the more accurate analysis presented here. Several recommendations are offered to improve the estimation of power-law creep parameters from bend test data.

1. Introduction

The present paper is concerned with steady-state creep deformation behavior of structural ceramics which are candidate materials for high-temperature stress-bearing applications, and aims at developing a mathematical scheme from which individual tensile and compressive power-law creep parameters can be estimated from conventional four-point bend test measurements. Instead of directly relying on uniaxial testing, flexural test methods are frequently adopted as an alternative to generate data from which information on materials' creep behavior may be extracted (see for example [1-3]). This practice can be attributed to the fact that a bending experiment is more stable and easier to perform without involving problems of fixturing and alignment usually associated with tension testing of brittle materials at high temperatures. A challenging issue that must be resolved for a given set of data produced from creep bend tests is: how can one, if possible, separately estimate the uniaxial creep behavior (both in tension and in compression) when the applied stress is given? Since bending data consist both tensile and compressive components, it is perhaps natural to expect that the resulting predictions would be strongly influenced by the form of constitutive equations assumed. A simple

Extensive literature review on the thermal creep of ceramics [4] indicates that generally speaking the steady-state behavior relating creep strain rate $\dot{\epsilon}$, to applied stress σ can be described by Norton's law in a form $\dot{\epsilon} = A \sigma^n$, where A is pre-exponential constant depending only on test temperature and materials' properties; n is stress exponent which may be

may not depend on stress. Hollenberg, et al. [4] presented the first analysis in which stresses and strains in the crept beam specimens can be calculated from the bend test data provided tensile power-law creep behaves identically to its compressive counterpart. This simplifies the analytical work substantially and allows the solutions to be presented in closed forms as the neutral axis location in this case always coincides with the center line of the beam height regardless of the magnitude of the applied loads.

However, it is now well recognized that tensile response might be distinct from its compressive counterpart inside a beam for a given material even tested under identical environments (see for example [5-6]). Consequently, for application to plain concrete, Krajcinovic [7] developed a damage theory for beams under pure bending in order to justify that tensile stresses assume a parabolic distribution in terms of strain while the compression behavior remains linearly elastic obeying Hook's law. More recently, Rosenfield et al. [8] extended this time-independent analysis to two more constitutive equations in tension, namely linear elastic with lower effective Young's modulus and elastic-perfectly plastic while once again leaving the compressive portion unchanged. On the other hand, within the arena of power-law creep, Finnie [9] was the first to recognize the possible situation of pronounced differences between tensile and compressive creep. His analysis permits $A_t = A_c$ and is capable of predicting creep rates from data generated by creep bending of a trapezoidal cross section beam provided n_t and n_c are of unity; here subscripts t and c refer to the cases of tension and compression

respectively. Talty and Dirks [10] extended the analysis of the same trapezoidal beam to a more general case of N other than unity (i.e. $n_t = n_c = N$).

The present paper extends the previous work to a completely general case of unequal tension vs compression power-law creep behaviors wherein not only the pre-exponent factors are permitted to be distinctive ($A_t \neq A_c$) but also the stress exponent constants may be unequal ($n_t \neq n_c$). For the sake of simplicity, only rectangular beams of uniform cross-sections are considered. Further, the existence of a steady-state is assumed so that time can be eliminated as a variable in the study. This assumption requires that the transient stage be short-lived and thus can be ignored, although it should be acknowledged that this phenomenon may sometimes become important [11-12] when a well-defined steady state does not develop [13].

In the next section, governing equations are first derived which relate separately the position of neutral axis and the applied moment to the curvature rate, \dot{K} and (unknown, a priori) power-law creep parameters. Computer programs were developed to solve these coupled non-linear algebraic equations numerically. Solutions are obtained in graphic form for an arbitrary set of power law constants. Graphic solutions are also given in terms of the load-point displacement rate, $\dot{\Delta}_p$ - a more measurable quantity than \dot{K} for collecting data on specimen's response. Cases of $n_t = n_c = N$ as examined by Talty and Dirks [10] and $A_t = A_c = A$, $n_t = n_c = N$ as analyzed by Hollenberg, et al. [4] are then presented as special cases of the present investigation. From the point of view of an experimenter,

in order to apply the current theory, a parametric study method must be used from which curves can be produced from the computer programs to match the discrete data points which are dictated by creep bend tests. Once accurate matching is achieved, the predicted power-law parameters become available at once from the well-fitted curve. For the sake of demonstration of how to use the theory, an example is given to estimate the four power-law constants from a set of six bend test data on debased alumina beams crept at 1100°C for a duration of more than 100 h. At conclusion, we are able to make some recommendations from the present analysis for those who prefer using the four-point bend test method to characterize power-law creep behavior in structural ceramics. Those suggestions should lead to more accurate characterization of creep properties.

2. Analysis

2.1 Derivation of the governing equations

In this section, we derive the control equations that relate material response to external variables and material constants, for a rectangular beam under four-point creep bending. (See Fig. 1)

As already discussed in the preceding section, under the action of some constant external loads the material is assumed to respond in the steady state according to a power law of the form:

$$\dot{\epsilon}_{sc} = A_c (\sigma/\sigma_0)^{n_c}, \quad \sigma \text{ in compression} \quad (1a)$$

and

$$\dot{\epsilon}_{st} = A_t (\sigma/\sigma_o)^{n_t}, \sigma \text{ in tension} \quad (1b)$$

where $\dot{\epsilon}_s$ is steady-state creep strain rate; A and n are materials constant, σ is the normal stress and σ_o is a reference stress. The subscript c and t refers to the case in compression and in tension respectively. A schematic sketch of Eq. 1 applied to a beam is given in Fig. 2.

The derivation that follows adopts the conventional simple beam theory which entails a fundamental assumption, known as Bernoulli's hypothesis, that planar sections remain plane during bending when creep is taking place so that no warping will occur (because of the need for geometric compatibility this condition seems to hold in practice [14]). This implies that the strain rate $\dot{\epsilon}$ of a fiber element is linearly dependent on Y, the distance away from the neutral axis where $\dot{\epsilon} = 0$ and the curvature rate, \dot{K} serves as a proportionality constant. Thus

$$\dot{\epsilon} = \dot{K} Y$$

and the stress distribution over the cross section of the beam is highly nonlinear and has the following form, according to Eq. (1):

$$\sigma(Y) = \sigma_o \left(\frac{Y \dot{K}}{A} \right)^{1/n} \quad (2)$$

regardless of the sign of stress. Equilibrium requirements then dictate that the total force acting on the compression side of the cross-section be counter-balanced by its tensile counterpart. This means that $F_c = F_t$ or $B \int_0^{H_c} \sigma dY = B \int_0^{H_t} \sigma dY$ where B is the beam width and H ($=H_c + H_t$) is the beam height (see Fig. 1). By integrating σ using Eqs. (2) and (1), and after some mathematical manipulations, this force balancing equation finally reduces to

$$\left\{ \frac{1}{R \frac{n_t}{n_c} + 1} + \frac{n_t - n_c}{n_c (n_t + 1)} \left[\frac{n_c (n_t + 1)}{n_t (n_c + 1)} \right]^{\frac{n_t}{n_c + 1}} \right\} h_c + h_c = 1 \quad (3)$$

where $R = A_t/A_c$, $\dot{k} = \dot{K}H/A_c$ and $h_c = H_c/H$ are dimensionless parameters. Here we choose A_c as normalizing factor for R and \dot{K} presumably because A_c is much easier to measure than A_t . Eq. (3) is a nonlinear algebraic equation of the form $Cx^n + x = 1$ for the unknown h_c quantifying the physical location of the neutral axis. Since both C and n are positive definite, as parameters appeared in Eq. (3) are all positive quantities, it can be proved from the form of this nonlinear algebraic equation that a unique solution for x always exists in the range $0 < x < 1$ beyond which no physical meaning may be assigned to x .

In addition, the requirement that the total summation of moments produced by local tractions be equated to the external moment, M , forms the second governing equation, viz.

$$M = \int_0^{H_c} \sigma Y B dY + \int_0^{H_t} \sigma Y B dY$$

Substitution of Eq. (2) for $\sigma = \sigma(Y)$ and recognition of $h_t + h_c = 1$ result in an equation relating the applied moment to the material's response \hat{k} :

$$m = \hat{k} \left[\frac{1}{n_c} - \frac{1}{n_t} - \frac{1}{n_c} \frac{2n_t+1}{n_t} + \frac{n_c}{2n_c+1} h_c \right] \quad (4)$$

where $m = M/(BH^2\sigma_0)$ is the normalized applied moment. The assignment of the reference stress σ_0 is somewhat arbitrary. Since the unit of the applied stress is generally expressed in MPa, it is convenient to set $\sigma_0 = 1$ MPa for simplicity.

Equations (3) and (4) constitute a system of algebraic equations for the two unknowns h_c and \hat{k} , while the remaining parameters such as the applied moment m and the materials parameters A 's and n 's are being treated as given. After examining the structure of these two equations, we arrive at the unfortunate conclusion that analytical solutions in close form cannot be obtained because they are highly nonlinear and coupled in

\dot{k} . Accordingly, a numerical approach is the practical way to tackle this problem. A computer program was developed which contains the following primary tasks: first the development of a subroutine to solve h_0 from Eq. (3) by a Newton-Raphson's iteration scheme. Input to this subroutine are R , n_t , n_0 and \dot{k} , the latter being treated as an independent variable. Note that initially an overshoot outside the range (0,1) for h_0 may arise during numerical iterations, stability can then be restored if h_0 be reset to its boundary value. Once h_0 is successfully solved from this subroutine, it can then be used as input, together with the independent variable \dot{k} , to Eq. (4) for the computation of m . At the end, a total of three one-dimensional arrays were generated, namely m , \dot{k} and h_0 . This concludes the computation phase of programming, and the plotting phase follows. The solutions were then displayed in graphic form for \dot{k} versus m as well as h_0 versus m with any given A 's and n 's.

2.2 General Solutions

2.2.1 Location of neutral axis, h_0

The solutions for h_0 are plotted as a function of m in Fig. 3 for several values of n_t at $n_0 = 4.0$, $R = 1000$. Generally speaking for the practical range of $m > 0.5$, as the applied stress increases, the compressive zone keeps shrinking with increasing n_t . Intuitively this must be true since an increase in n_t implies that the material's ability to support tensile stresses is reduced for a fixed creep rate. When $n_t = n_0$, $h_0 = 0.2$, independent of the applied stress. In fact, h_0 can be

expressed analytically in case of equal n . This special case will be discussed later. Another interesting observation that can be extracted from Fig. 3 is that when m is at a value of around one half, h_0 is about 0.2 regardless of the value of n_t . As a matter of fact, when examined in a more broader base, we found that when m lies between 0.25 and 0.4 the solutions are quite insensitive to both n_t and n_0 suggesting that this range of m should be avoided in a testing program that aims to characterize the materials creep parameters. Fig. 4 presents another solution for h_0 for five values of R , fixing values of n_t and n_0 at 1 and 5 respectively. As expected, the higher the value of R , the lower the size of compression zone as high R implies that the material's creep resistance in tension is reduced at a given strain rate (or applied moment). When m exceeds 10, however, a major portion of the beam is in compression for R values up to 1000. Conversely, setting $n_t = 5$ and $n_0 = 1$ demonstrated a reverse trend, as shown in Fig. 5 for the same five values of R . Again, cases of higher R result in smaller compression zone as expected.

2.2.2 Curvature rate of a beam element, \dot{k}

The materials response in the form of curvature rate \dot{k} under creep bending for a given applied moment m is plotted in Fig. 6 on a log-log scale for five values of n_t and fixing $n_0 = 4$ and $R = 1000$. Two important observations can be made here: (1) the curves appear linear with, of course, always positive slopes when n_t 's are in the neighborhood of n_0 but when the gap between the values of n_t and n_0 widens, the curves become nonlinear and concave upward; (2) a "blind point" in the vicinity of $m = 1/2$ is also observed, similar to the solutions of h_0 . Fig. 7

demonstrates the solutions of \dot{k} upon variation of R under fixed values of $n_t = 1$ and $n_0 = 5$. Again, owing to big differences between the values of n_t and n_0 , concave upward curves are obtained. Another interesting feature noteworthy to state is the solutions converge into one single straight curve as the applied moment exceeds 15. This means that applying a load in excess of $m = 15$, would generate a straight line in \dot{k} vs m plot, regardless of the values of R and therefore is not particularly useful. Lower loads (much less than $m = 15$) are thus recommended. If, on the other hand, $n_t = 5 \gg n_0 = 1$ then the solutions are well-behaved in the practical range of the applied load ($.01 \leq m \leq 100$) as indicated in Fig. 8, although most of the solutions appear to be linear.

2.2.3 Outer fibre stresses, σ_0 and σ_t

As can be seen from the preceding section, during steady state creep the neutral axis is displaced from the centroid and the stress distributions are highly non-linear. As a result, it is to be expected that the outer fibre stresses, both at the tensile side as well as at the compression side must in general differ from the initial elastic stress levels. In terms of the applied bending moment M , the outer fibre elastic stresses both in tension and in compression have a value $\sigma_e = 6M/(Bh^2)$ from classical simple beam theory, and in terms of dimensionless quantities, there results $\delta_e = 6m$, where $\delta_e = \sigma_e/\sigma_0$ is the normalized outer fibre elastic stress.

The steady-state compressive creep stress at the outer surface of the beam is

$$\sigma_c = \sigma_0 (k h_0)^{1/n_0}$$

as evidenced from Eq. (2). Normalizing against σ_0 we have

$$\sigma_c / \sigma_0 = \frac{1}{6m} (k h_0)^{1/n_0} \quad (5)$$

Similarly the creep stress at the tensile edge, also normalized by σ_0 is

$$\frac{\sigma_t}{\sigma_0} = \frac{1}{6m} [k (1-h_0)/R]^{1/n_t} \quad (6)$$

Examination of these two equations indicates that the outer fibre creep stresses, unlike their elastic counterpart, are not only a function of applied moment, but also dependent on the neutral axis location and the intrinsic power-law creep parameters. The maximum compressive stresses for several n_t are plotted in Fig. 9, according to Eq. (5) for typical values of $n_0 = 4$ and $R = 1000$. When $m < 0.35$ corresponding to an elastic stress of about 2 MPa, higher values of n_t yield lower compressive stresses; the reverse situation occurs if the applied stress exceeds 2 MPa. On the other hand, the maximum tensile stresses at the outer fibre, as plotted in Fig. 10 from Eq. (6), show a unique feature, namely for a fixed applied load, in the practical range (1 - 600 MPa) low values of n_t yield higher tensile creep stresses. Note that in both cases, as shown in

Figs. 9 and 10, in the case of $n_0 = n_t$, the outer fibre stresses are independent of the applied moment and as will be shown later in Sec. 2.3 they can be expressed in closed forms.

2.2.4 Load-point displacement rate, $\dot{\Delta}_p$

As demonstrated in the preceding sections, $\dot{\kappa}$ is a proper parameter to measure the response of creep for a bend bar under the constant applied moments. Unfortunately, the curvature time-rate of a beam at a fixed location is difficult to measure in the laboratory and it is a general practice to measure instead the load-point displacements continuously as a function of time. Hence, it is desirable to present solutions in terms of $\dot{\Delta}_p$.

For a given material with a well defined $\dot{\kappa}$ vs m relationship the load-point displacement rate $\dot{\Delta}_p$ incurred from a four-point bend beam can be solved numerically by integration of $\dot{\kappa}$ along the beam length x with linear moment distribution in the outer span and a constant maximum moment in the inner span. Here, it is assumed that shear effects on the beam deflection y are negligible and the slopes of the deformed beam shape are small ($dy/dx \ll 1$). The differential equation that needs to be solved is then $d^2\dot{y}/dx^2 = \dot{\kappa}(x) = f(m)$ with $\dot{\kappa} = f(m)$ given in Sec. 2.2.2. Setting the origin of the coordinate system at the mid span of the deformed beam, the proper boundary conditions are $y(0) = 0$ and $y'(0) = 0$ due to symmetry. After the deformed shapes $\dot{y} = \dot{y}(x)$ are solved, the load-point displacement rate is given by $\dot{\Delta}_p = \dot{y}(L/2) - \dot{y}(l/2)$ where L and l are the lengths of major and minor spans respectively. Typical solutions are plotted in Fig.

1) for nondimensional load-point displacement rate, defined as $\dot{\delta}_p / M \Delta_c$ as a function of the applied moment m for several values of α_1 with $\alpha_c = 4$, $R = 1000$, $L = 41$ and $N/l = 1/2$. Similarities between Fig. 6 and 11 are observed. Whenever $\alpha_c = \alpha_1 = N$, the solution can be described by a linear curve owing to the fact that the relationship between $\dot{\delta}_p$ and $\dot{\delta}_p$ is linear and has a form

$$\dot{\delta}_p = \frac{N(N-2)}{(L-1)(L-(N-1))} \dot{\delta}_p$$

2.) The special cases

Having obtained the general solutions in the previous section, it is easy to arrive at the results for the special cases as considered by Hollenberg et al. [8] and Tilly and Dirks [10].

2.1. The case $\alpha_1 = \alpha_c = N : N = 1$

This is the case considered by Tilly and Dirks [10] and Coert et al. [12]. For this case, Eq. 3 describing the location of neutral axis takes the following simple form

$$\eta_c = \frac{r}{r + R} \quad (17)$$

independent of the applied moment m . This is in agreement with the work of Coert et al. [12] (See Eq. 3 of Ref. 12 in which our η is equivalent to their S^0). In addition, it can be shown from Eq. 4 that the moment vs curvature rate is linear when plotted on logarithmic scales, and therefore can be described by

$$\dot{k} = C a^N \quad (8)$$

where C is the intercept at $a = 1$ and is only a function of n_0 , R and N :

$$C = \left[\frac{(2N+1)/N}{n_0^{2N+1/N} - (1-n_0)^{2N+1/N}} a^{1/N} \right]^N \quad (9)$$

Fig. 12 presents the solutions of n_0 for several N , based on Eq. (7) as a function of C defined in Eq. (9). Fig. 13 demonstrates the solutions for

R . If $n_0 = n_1 = R$, the bond test data in terms of \dot{k} vs a ought to be fitted by a linear curve on logarithmic axis. n_0 is automatically obtainable from \dot{k} and k (see Fig. 1 and definition of \dot{k}). C as well as N can then be extracted from this curve. Figs. 12 and 13 can then be used to obtain n_0 and R (hence n_1) and the complete cross parameters are determined.

2.3.2 The case of uniform property ($n_1 = n_0 = R$; $R = 1$)

This case has already been considered by Hollenberg et al. [4]. The neutral axis in this case always coincides with the centroid (i.e., $n_0 = 1/2$) as can be shown from Eq. 7 when $R = 1$ is substituted.

Constitutive equation 8 describing the relations between \dot{k} and a is of course still valid but the intercept C now takes the simple form:

$$C(n) = 2 \left(\frac{2n+1}{\sqrt{2}} \right)^2 \quad (10)$$

Fig. 14 is a plot of n against C from Eq. (10). This can be used as a first step to check whether the material has uniform properties in creep by checking the observed value of C to see if it agrees with the predicted value of C given by this plot.

3.4 Application

As an example of demonstrating the applicability of the present analysis, three loads of different magnitude were applied to debased alumina (commercially known as AD-85¹ from Coors Corporation) beams at 1100°C in a four-point bend configuration with major and minor spans set at 40 and 10 mm respectively. Load-point displacements are continuously monitored as a function of time. Apparent steady-state was observed in all cases within 30 hour duration. Table 1 lists the pertinent data of measurements. After data were taken, the first step is to plot $\dot{\epsilon}_p$ versus σ on logarithmic scales. If the resulting curves are linear, the solutions presented in Sec. 2.3 can be used to check whether special cases apply. Since plotting of data in Table 1 indicated non-linear behavior (suggesting $n_1 \neq n_2$), the special cases discussed in Sec. 2.3 must be ruled out. Solutions of different n and σ were produced in order to fit the data points. It was finally found that a special curve as shown in Fig. 15 with the following constants $n_1 = 4$, $n_2 = 1/2$, $\sigma = 50,000$ fits the

¹ Certain commercial equipment, instrument or materials are identified in this paper in order to adequately specify the experimental procedure. Such identification does not imply recommendation or endorsement by the NBS, nor does it imply that the materials identified are necessarily the best available for the purpose.

data well. A_c was determined from the solution to be $0.85 \times 10^{-13} \text{ s}^{-1}$. Thus the steady-state tension creep behavior of this refractory material can be described by

$$\dot{\epsilon}_{st} = 4.25 \times 10^{-9} \sigma^{1/2}$$

and the compression creep, on the other hand, by

$$\dot{\epsilon}_{sc} = 0.885 \times 10^{-13} \sigma^4$$

where $\dot{\epsilon}$ and σ have the units of s^{-1} and MPa respectively.

The predictions strongly suggest a profound difference of creep behavior between tension and compression. Uniaxial tension tests were also performed which yield the same order of magnitude as predicted by the current analysis. Additional tests in simple tension as well as in compression are being performed in order to verify the predictions. Detailed microstructures of these post crept beam specimens are also being investigated in order to understand the rheology leading to the resulting power-law stress exponents. One dominating factor obtained from the preliminary studies is the observation of compositional changes due to devitrification, resulting in drastic variation of viscosity in the grain boundary liquid phases [15-16]. This strong stress-dependent viscosity coupled with local recrystallization in the compression zone and dilatancy and/or cavitation in the tension region may be responsible for the unequal stress exponents.

In contrast, the conventional method assumes $R = 1$ and $n_t = n_c = N$ so that the outer fibre creep rate can be computed from the load-point displacement rate data by the following equation

$$\dot{\epsilon}_{so} = \frac{2(N+2)H\dot{\Delta}_p}{(L-t)[L+(N+1)t]}$$

and the outer fiber stresses by

$$\sigma = \sigma_o \left(\frac{2N+1}{3N} \right)$$

Table II lists the resulting outer fiber creep rates and stresses computed from the same set of load point displacement data tabulated in Table I. A plot of $\dot{\epsilon}_{so}$ versus σ_o on logarithmic scales by least squares method as shown in Fig. 15 leads to a prediction of $A = 1.71 \times 10^{-11} \text{ s}^{-1}$ and $N = 1.86$. Hence we see there are substantial differences in the prediction of power-law creep parameters between the present analysis and the conventional method. Notice that $A_t < A < A_c$ and $n_t < N < n_c$ implying that the conventional techniques, by imposing uniform properties, effectively generate an average response in bending creep.

3. Discussion

We have presented a viable technique by which individual tension and compression creep behaviors, being equal or not, can be predicted directly from bend test data. Several main features in the analysis are noteworthy: (1) the neutral axis of the beam cross-section is, in general, not located at the centroid, the location is not only a function of the material constants but also of the applied loads. This is generally indicated by observations of significant densities of cavities developed over 50 percent of the beam cross section, suggesting the neutral axis has

migrated towards the compressive side. (2) If a plot of data on $\dot{\epsilon}$ vs m shows strong non-linearity which is concave upward, there will be a big difference between n_c and n_t . (3) There exists an applied load for all materials, in the neighborhood of 1 - 2 MPa of initial outer fibre elastic stress, under which the material response in $\dot{\epsilon}$ or $\dot{\Delta}_p$ will be insensitive to n 's suggesting that this load level is not useful in the test program.

(4) If $\dot{\epsilon}$ vs. m data demonstrates a linear response on logarithmic axes, then the results given in Sec. 2.3 can be first used to ascertain whether the material poses uniform creep properties. Otherwise, the general solution scheme as detailed in Sec. 2.1 has to be adopted since a linear curve within a short range of m does not necessarily mean that $n_t = n_c$ as evidenced from Fig. 7. An example was given in Sec. 2 to show how to apply the current analysis to a realistic case.

However, the analysis does have some restrictions and limitations built-in which ought to be borne in mind. First, the constitutive law is assumed to take a power-law equation form with the distinction being made through the variations in n and A . Microscopic observations including SEM and STEM have showed that in a general ceramic system, cracks and cavities are developed in different patterns both in terms of density and orientations inside the tensile and compressive zones of a crept bend specimen. Hence, cracking and cavitation play an important role in the contribution to creep resulting in distinct behaviors. Secondly, no deformation mechanism changes are assumed to take place under uniaxial loading so that a single power-law equation completely characterizes the creep behavior. Consequently, the current analysis is not applicable to materials exhibiting bi-linear law, although in principle, a numerical

scheme may be developed to handle this case. Finally the problem of creep fracture is not addressed in this paper. As a result, the solutions presented here are assumed to be valid irrespective of how high the loads are applied. Realistically, however, as the loads become higher and higher, the solutions will always be termed invalid somewhere by premature failure due to void growth and flaw linkage. The prediction of rupture time as a function of applied stress is thus an important area which warrants further studies.

Rosenfield et al. [8] recently presented a similar time-independent analysis on a beam with three different tensile laws. By fixing the compression behavior as linearly elastic, they found an interesting result that at $1/5$ of the beam depth from the tension edge, the stress there is fairly fixed regardless of the form of the tensile deformation law. However, with the removal of the assumption of linear behavior in compression, the results given by the present analysis did not show this feature. Accordingly, we must conclude that their results possess a strong limitation induced by the imposed linear elastic behavior in compression.

4. Summary and Recommendations

In lieu of summary of the analysis presented in the paper, the following recommendations are offered to experimenters who intend to use bend tests for characterizing the materials creep behavior:

- (1) The range of the applied loads should be as wide as possible; at least two orders of magnitude in loads (e.g. 5 - 600 MPa) are recommended.

(2) In case that higher moments cannot be achieved owing to premature fracture a supplemental test program either in tension or in compression should be performed for the purpose of reducing computer work, thus improving the accuracy of the results.

(3) Direct measurement, of uniform curvature rate in the inner span are preferred to load-point displacements measurements as the latter induce complications such as shearing effects, although the former may be more difficult to do.

Acknowledgments

Financial support by AR&TD Fossil Energy Materials program of the U.S. Department of Energy under interagency agreement DE-A105-800R20679 and by the U.S. Air Force Office of Scientific Research under the agreement AFOSR-ISSA-84-00013 with NBS are hereby acknowledged. The author is grateful to Professor Karl Jakus of the University of Massachusetts, Amherst, MA for carrying out the bending experiment on glass-bonded alumina, and to Drs. Richard J. Fields and Sheldon M. Wiederhorn of NBS for critically reviewing the manuscript.

References

1. S.U. Din and P.S. Nicholson, J. Mater. Sci. 10 (1975) 1375.
2. S.U. Din and P.S. Nicholson, J. Am. Ceram. Soc. 58 (1975) 500.
3. W.R. Cannon and T.G. Langdon, J. Mater. Sci. 18 (1983) 1.
4. G.W. Hollenberg, G.R. Terwilliger and R.S. Gordon, J. Am. Ceram. Soc. 54 (1971) 196.
5. M.S. Seltzer, Bul. Am. Ceram. Soc. 56 (1977) 418.
6. R. Morrell and K.H.G. Ashbee, J. Mater. Sci. 8 (1973) 1253.
7. D. Krajcinovic, J. Appl. Mech. 46 (1979) 592.

8. A.R. Rosenfield, D.K. Shetty and W.H. Duckworth, to appear in J. Mater. Sci.
9. I. Finnie, J. Am. Ceram. Soc. 49 (1966) 218.
10. P.K. Talty and R.A. Dirks, J. Mater. Sci. 13 (1978) 580.
11. T. Fett and D. Munz, ibid. 19 (1984) 1791.
12. H. Cohrt, G. Grathwohl and F. Thgummler, Res. Mechanica, 10 (1984) 55.
13. R.M. Arons and J.K. Tien, J. Mater Sci. 15 (1980) 2046.
14. G.H. MacCullough, Trans. ASME (1933) 55.
15. S.M. Wiederhorn, B.J. Hockey, R.F. Krause and K. Jakus, submitted to J. Mater. Sci.
16. W.D. Kingery, H.K. Bowen and D.R. Uhlmann, "Introduction to Ceramics", John Wiley & Sons, Inc. (1976) p. 757.

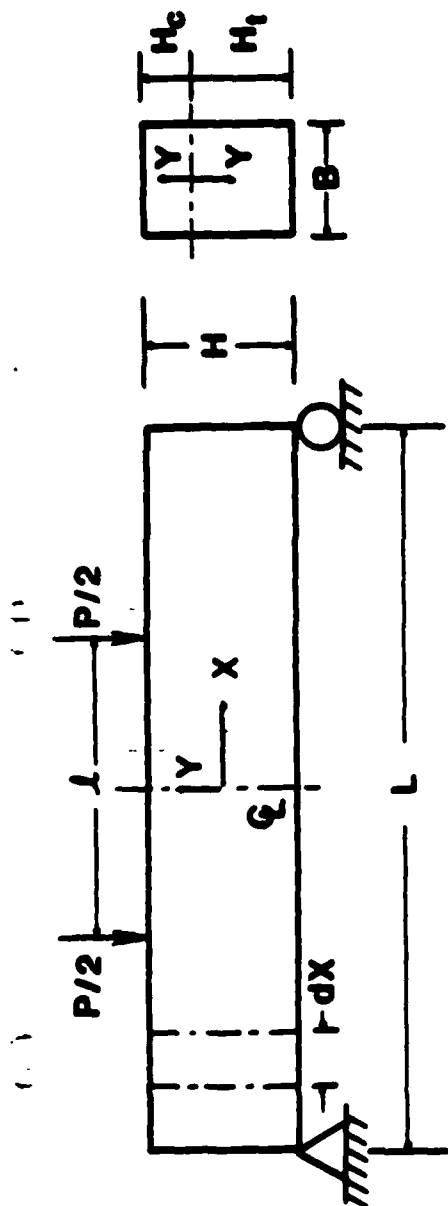
Table I. Calculations of normalized load-point displacement rates from 4-point bend data of glass alumina tested at 1100°C. Power-law creep parameters were then obtained based on the present analysis.

Specimen No.	Beam Height H (mm)	σ_e (MPa)	m	\dot{A}_p ($\times 10^{10}$ m/s)	\dot{A}_p/H ($\times 10^7$ s $^{-1}$)	\dot{A}_p/HA_c ($\times 10^{-6}$)
1	2.785	20	3.333	5.185	1.862	2.191
2	2.785	20	3.333	4.719	2.694	1.993
3	2.770	30	5.000	6.311	2.278	2.680
4	2.770	30	5.000	6.656	2.403	2.827
5	2.770	40	6.666	11.50	4.152	4.885
6	2.770	40	6.666	11.57	4.177	4.914

Table II. Computation of strain rates for the same set of data listed in Table I. Different power law creep parameters were then predicted based on conventional method.

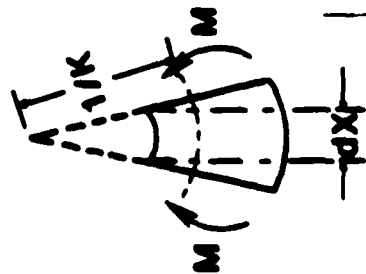
Specimen No.	Beam Height H (mm)	Outer Fibre Elastic Stresses σ_e (MPa)	Outer Fibre Creep Stresses σ (MPa)	$\dot{\Delta}_p$ ($\times 10^{10}$ m/s)	Creep Rate $\dot{\epsilon}_{ss}$ ($\times 10^9$ s $^{-1}$)
1	2.785	20	16.93	5.185	5.417
2	2.785	20	16.93	4.719	4.930
3	2.770	30	25.40	6.311	6.557
4	2.770	30	25.40	6.656	6.916
5	2.770	40	33.87	11.50	11.951
6	2.770	40	33.87	11.57	12.020

Note: $\sigma = \left(\frac{2N+1}{3N}\right)\sigma_e \cdot \dot{\epsilon}_{ss}^{-\frac{2(N+2)}{(L-2)[L+(N+1)2]}}$; $N = 1.86$, $L = 40$ mm, $l = 10$ mm .

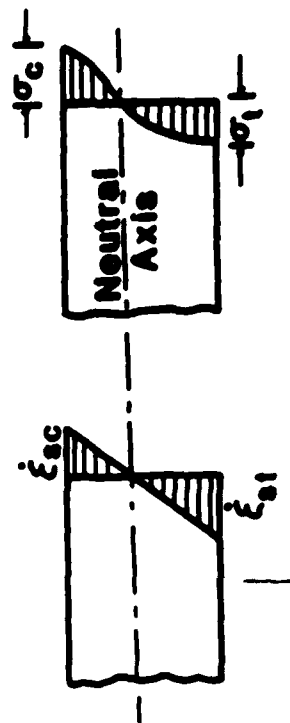


(a)

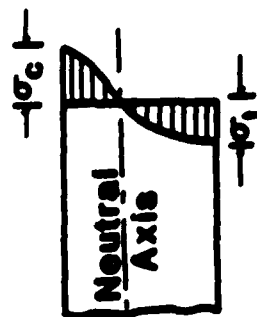
(b)



(c)



(d)



(e)

Fig. 1. Schematic sketches of a four-point bend beam. (a) loading configuration (b) representative cross-section (c) typical element of deformed shape (d) strain-rate distribution and (e) stress distribution.

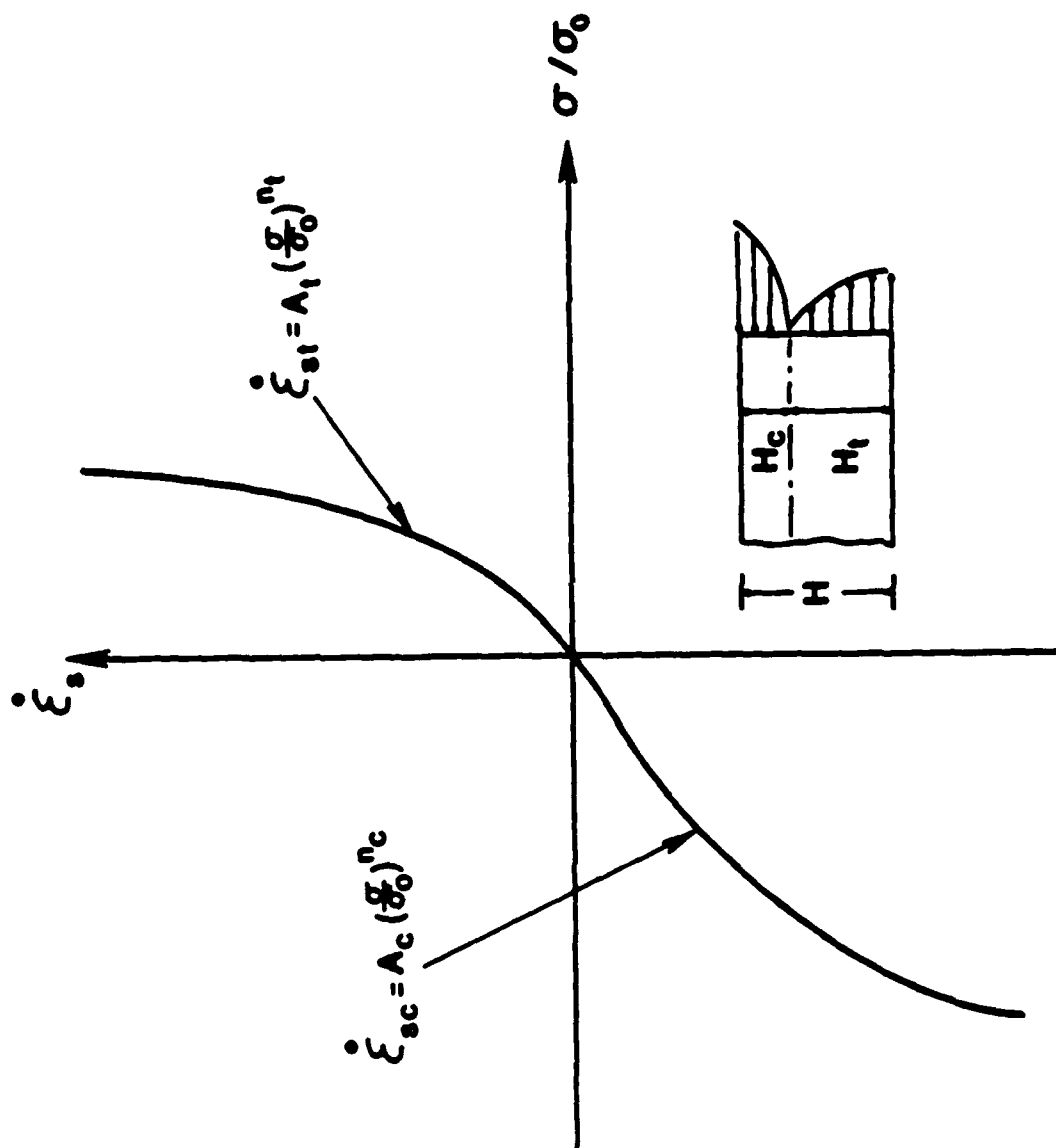


Fig. 2. Schematic of power-law constitutive equations in creep showing distinct behaviors between tension and compression.

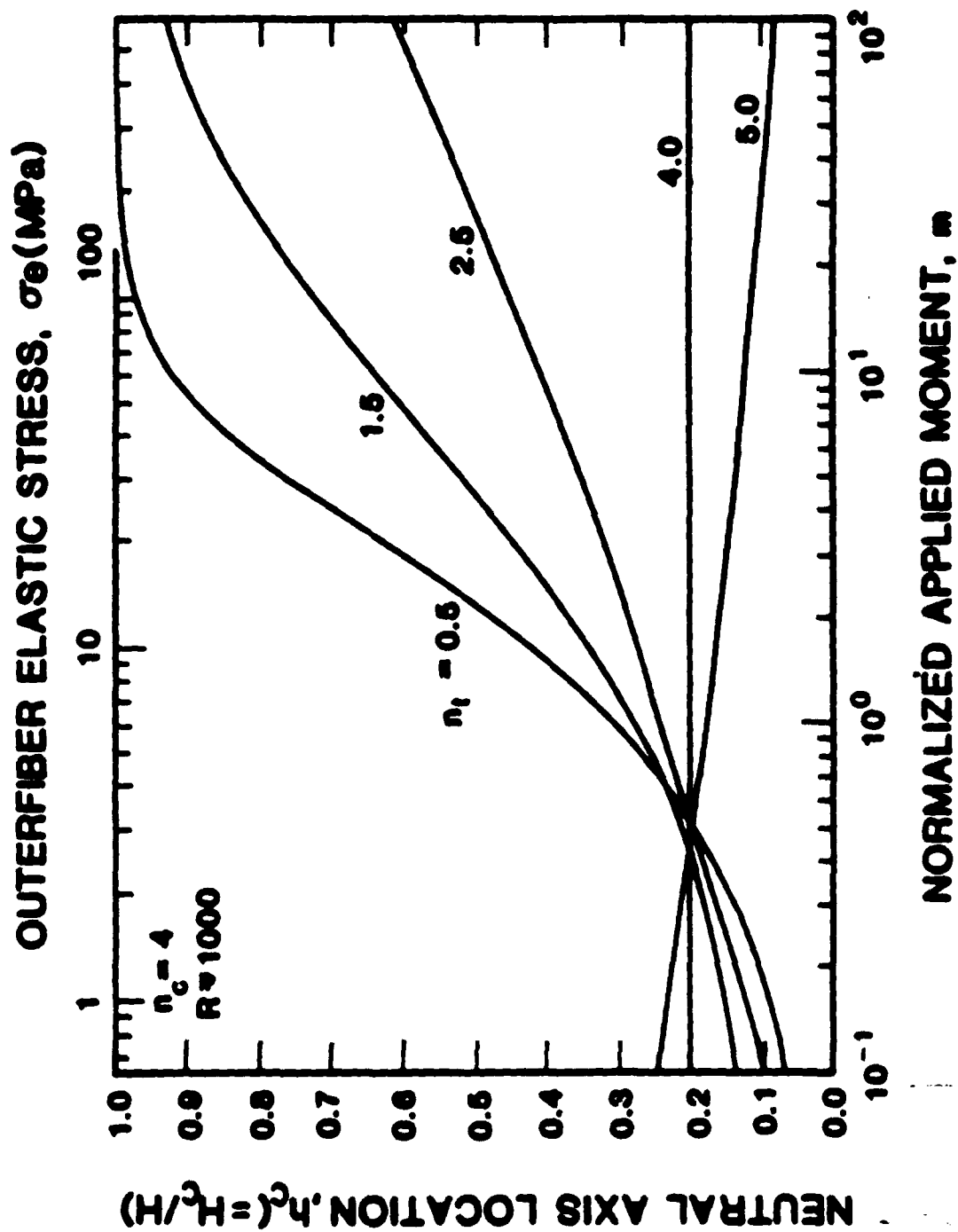


Fig. 3. Solutions for normalized compressive size h_0 as a function of the applied bending moment, n_0 at $n_0 = 4$, $R = 1000$ and $n_t = 0.5, 1.5, 2.5, 4.0$ and 5.0 respectively.

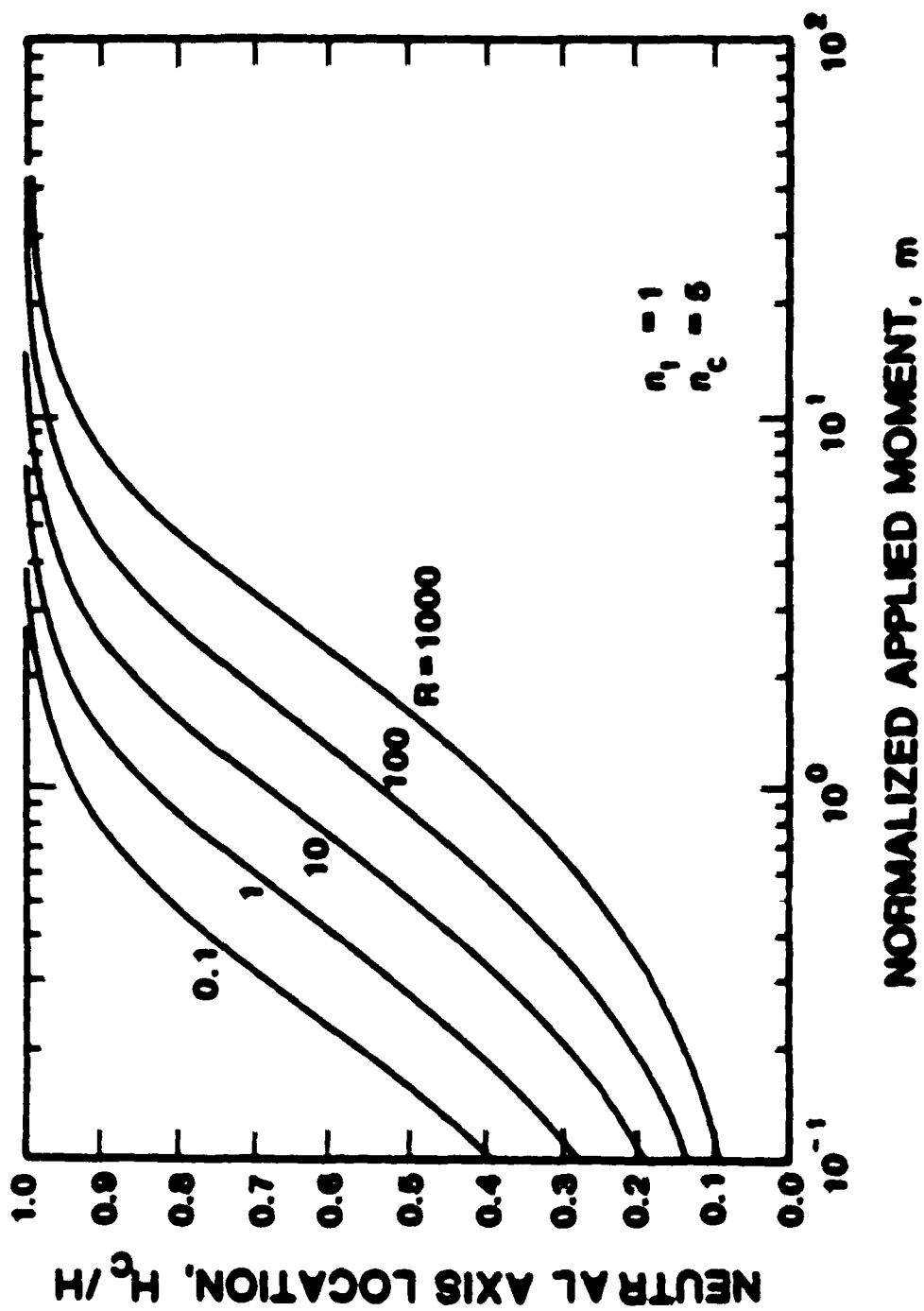


Fig. 4. Plots of neutral axis location versus the applied moment for $n_t = 1$, $n_c = 6$ and $R = 0.1, 1, 10, 100$ and 1000 respectively.

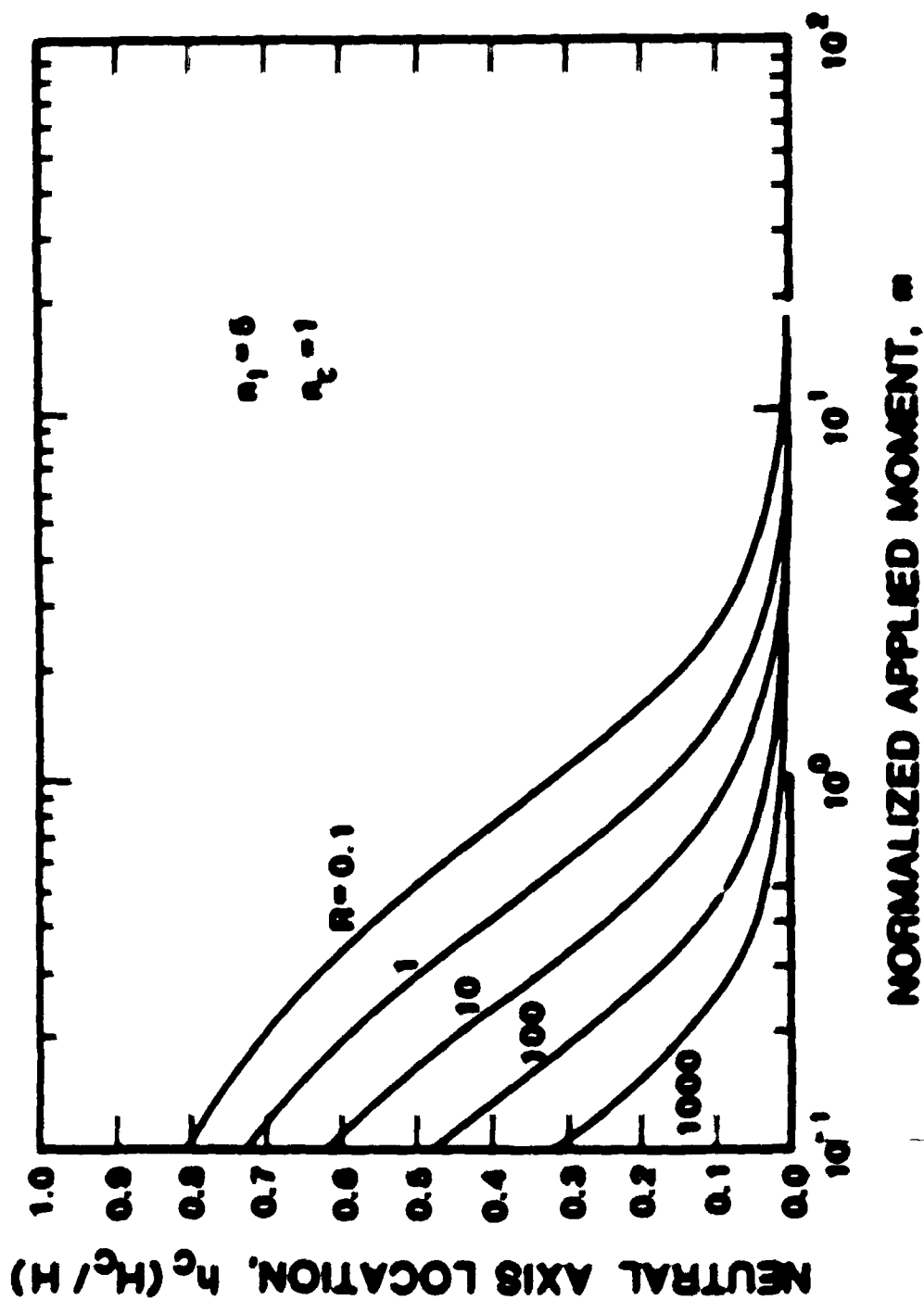


Fig. 5. Compressive case size solutions as a function of the applied moment at $\eta_1 = 5$, $\eta_2 = 1$ and $R = 0.1, 1, 10, 100$ and 1000 respectively.

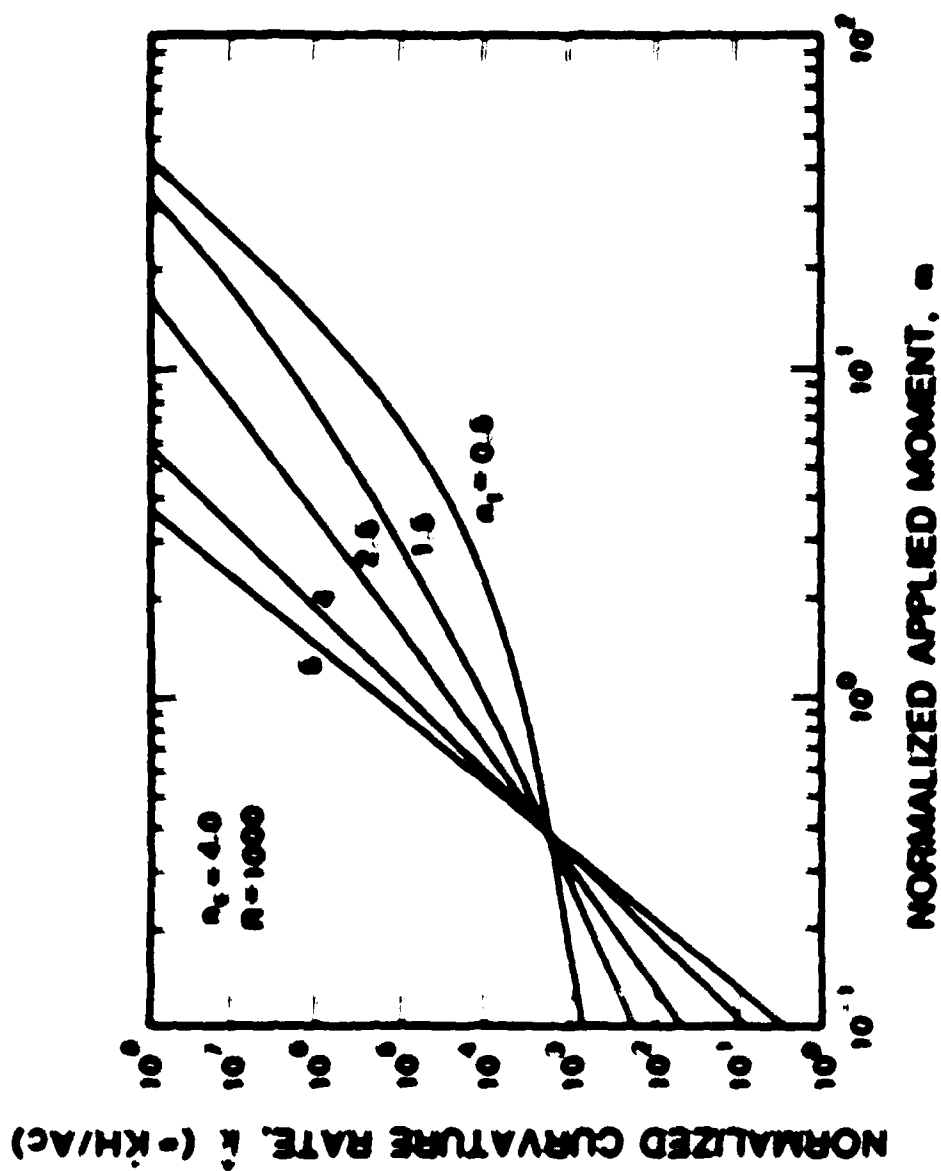


Fig. 6. Solutions of normalized curvature rate as a function of applied moment for $a_2 = 4$, $n = 1000$ and $a_1 = 0.5$, 1.5 , 2.5 , 4 and 1000 respectively.

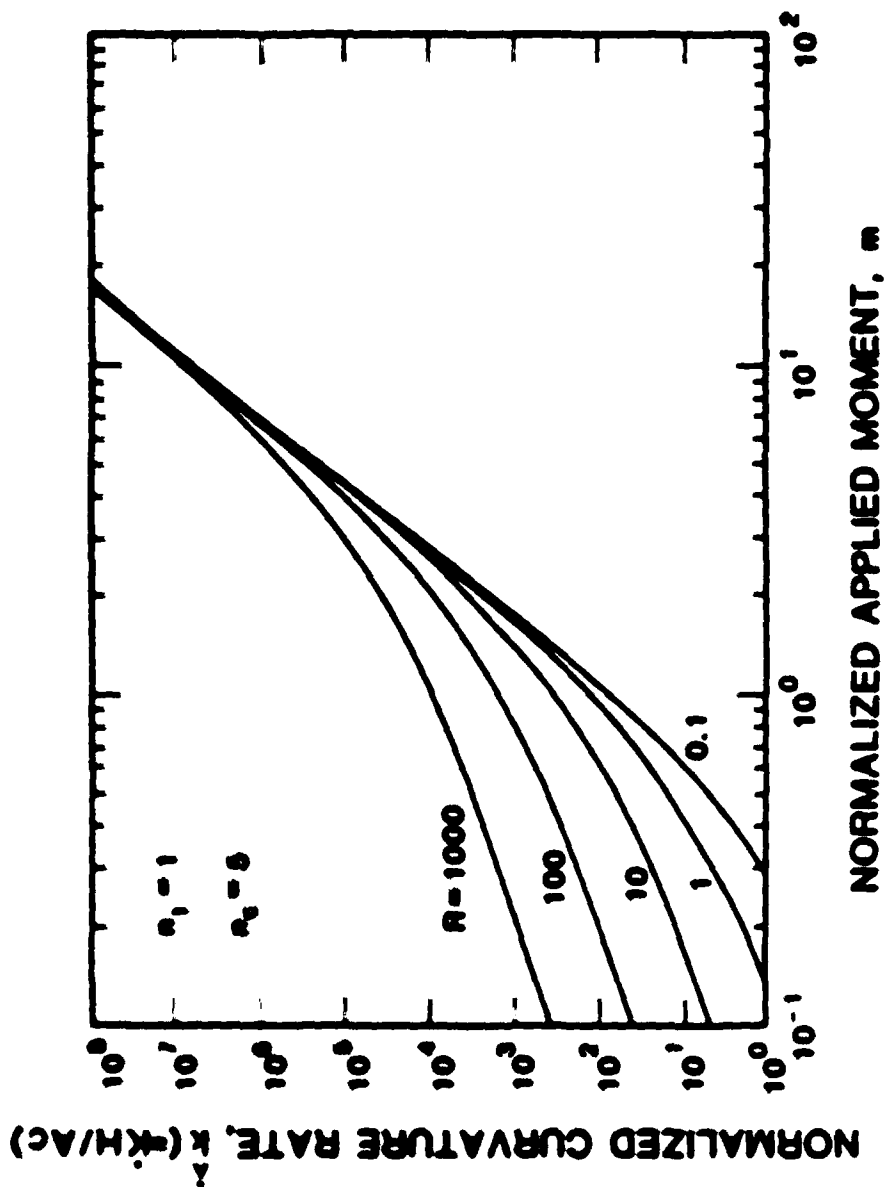


Fig. 7. Typical plots of \dot{k} vs m for $n_c = 1$, $n_c = 5$ and $R = 0.1$, 1.0, 10, 100 and 1000 respectively.

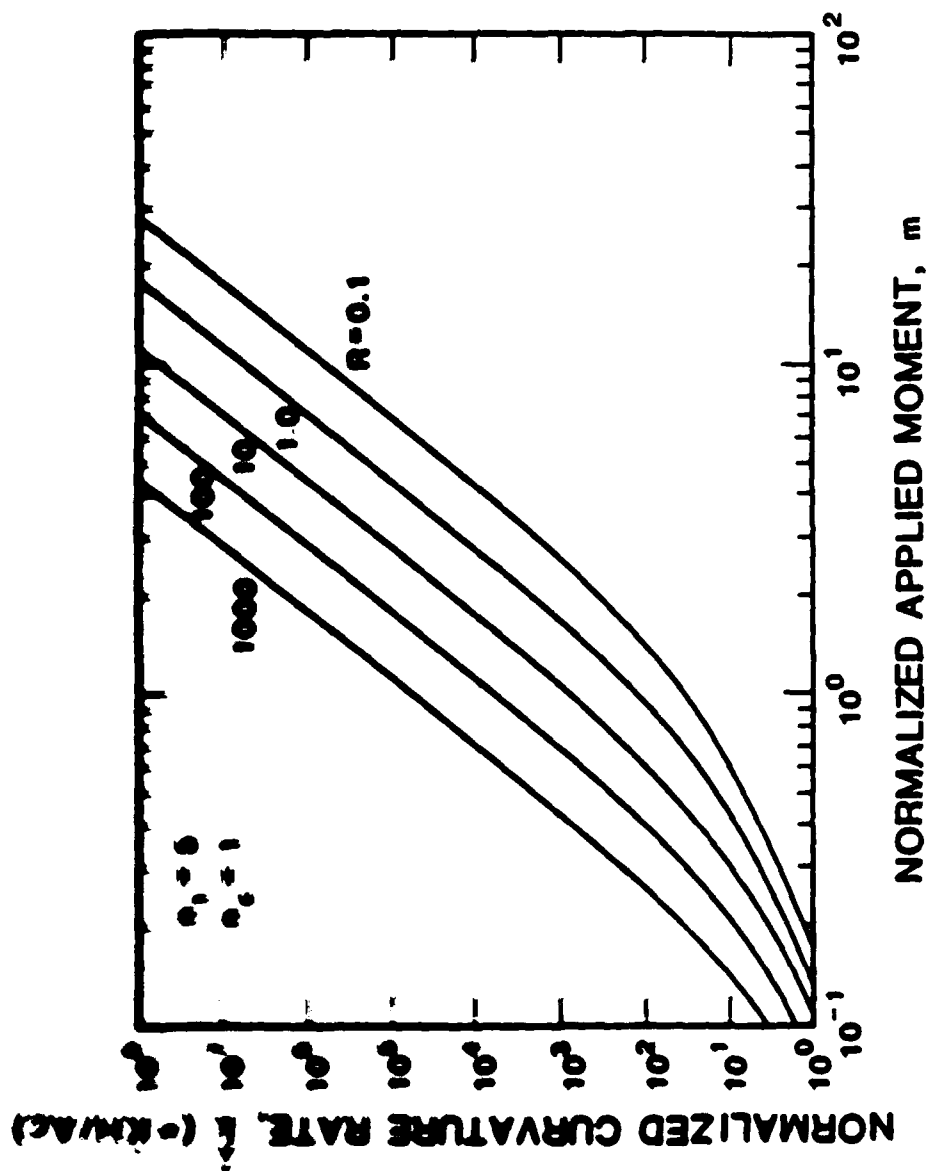


Fig. 8. Similar plot as Fig. 7 except $n_t = 5$ and $n_c = 1$.

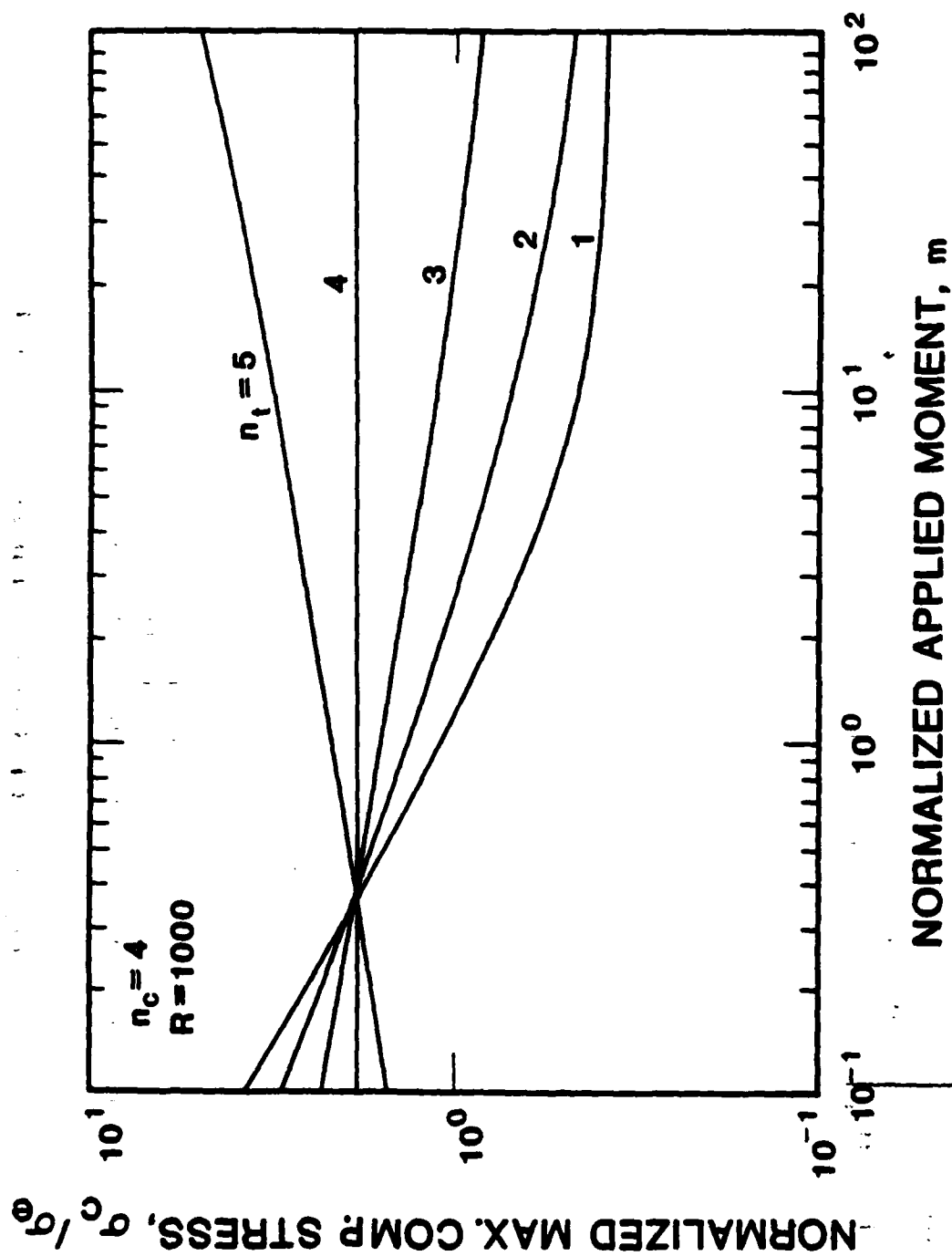


Fig. 9. Plots of outer fibre compressive creep stress normalized against elastic stress versus applied moment for $n_c = 4$, $R = 1000$ and $n_t = 1, 2, 3, 4$ and 5 respectively.

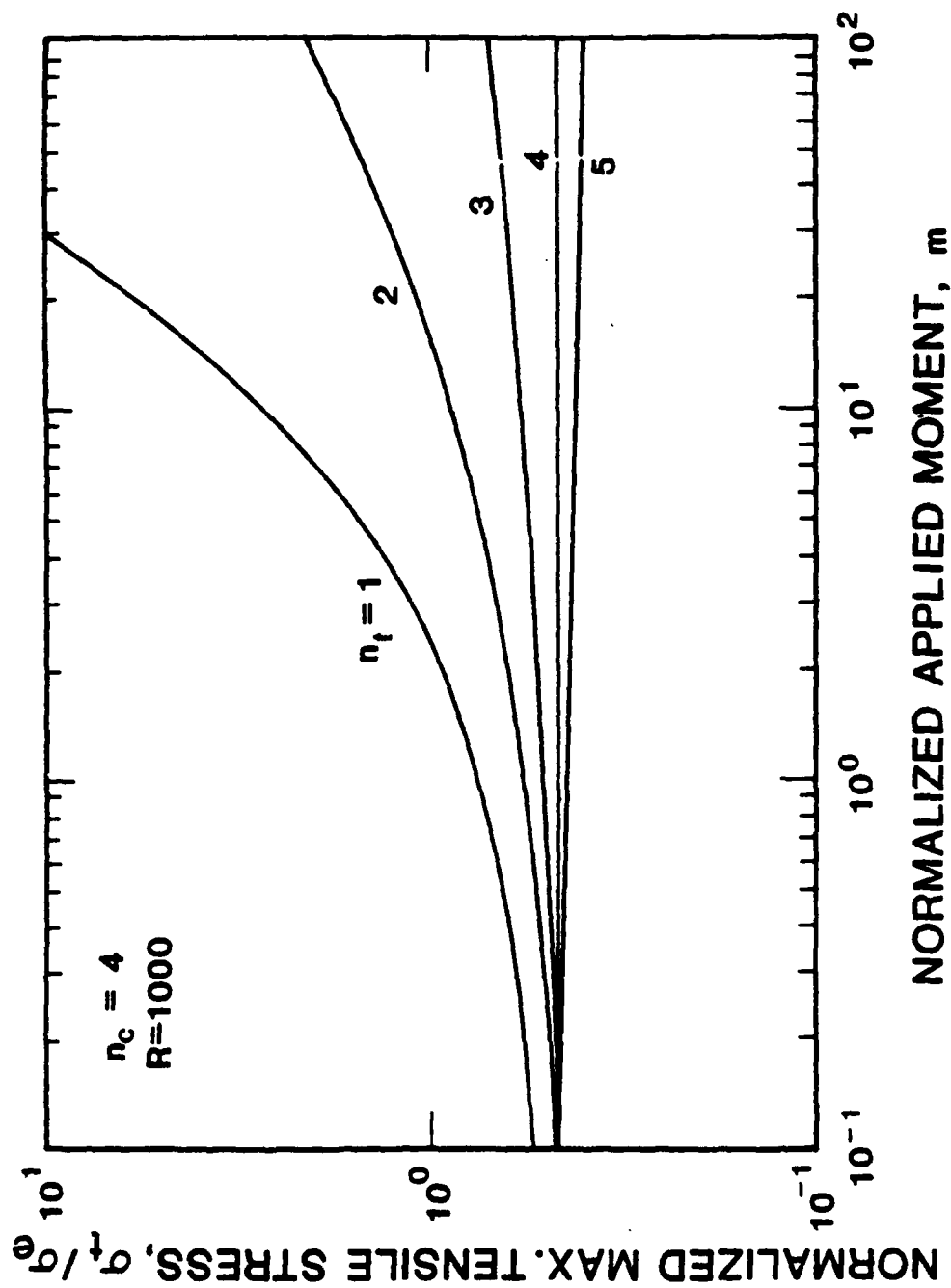


Fig. 10. Numerical solutions for normalized outer fibre tensile stress, (σ_t/σ_e) as a function of m . The materials constants are the same as in Fig. 9.

INITIAL OUTERFIBER ELASTIC STRESS, σ_e (MPa)

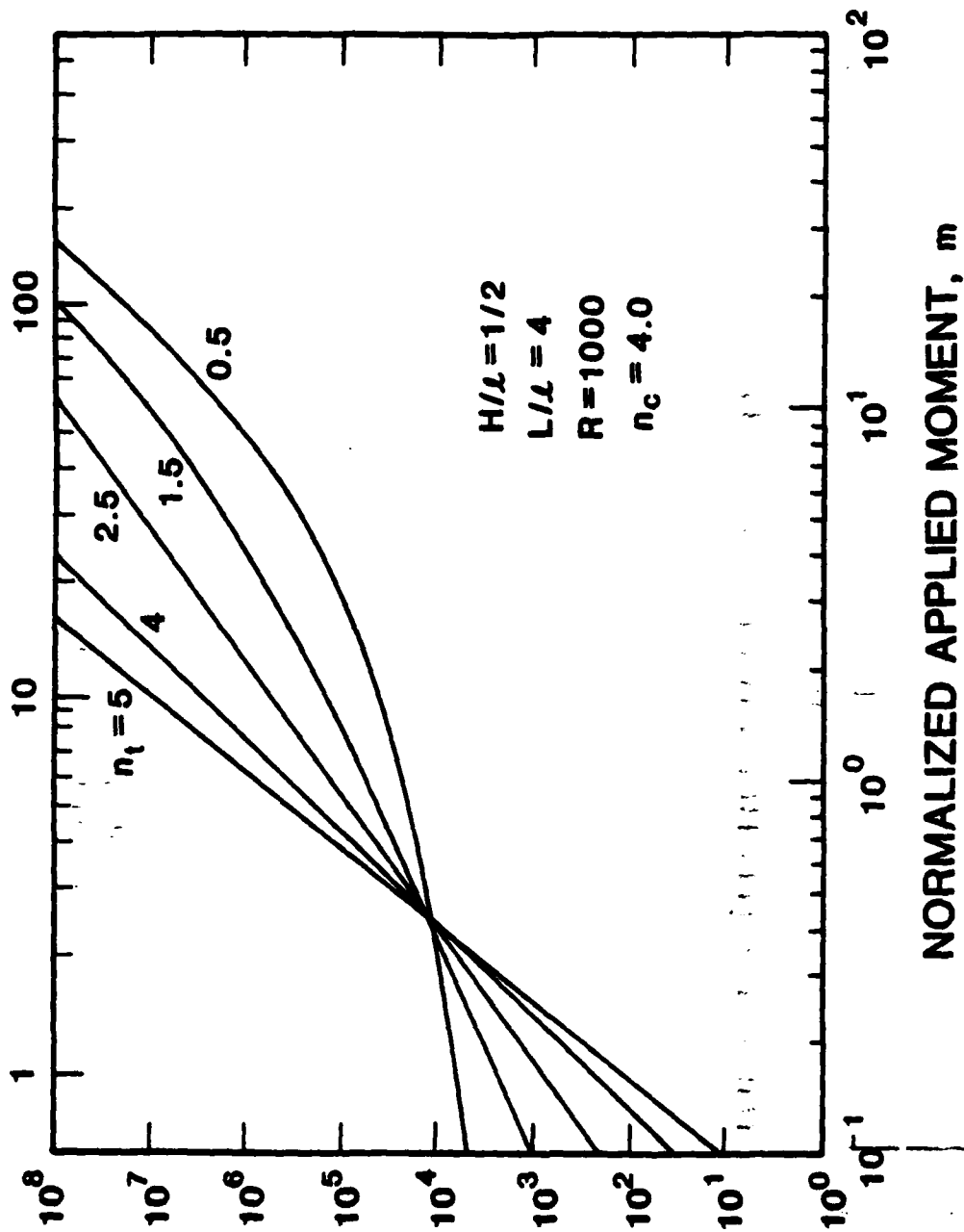


Fig. 11. Plots of load-point displacement rate versus m for several values of n_t at $n_c = 4$ and $R = 1000$.

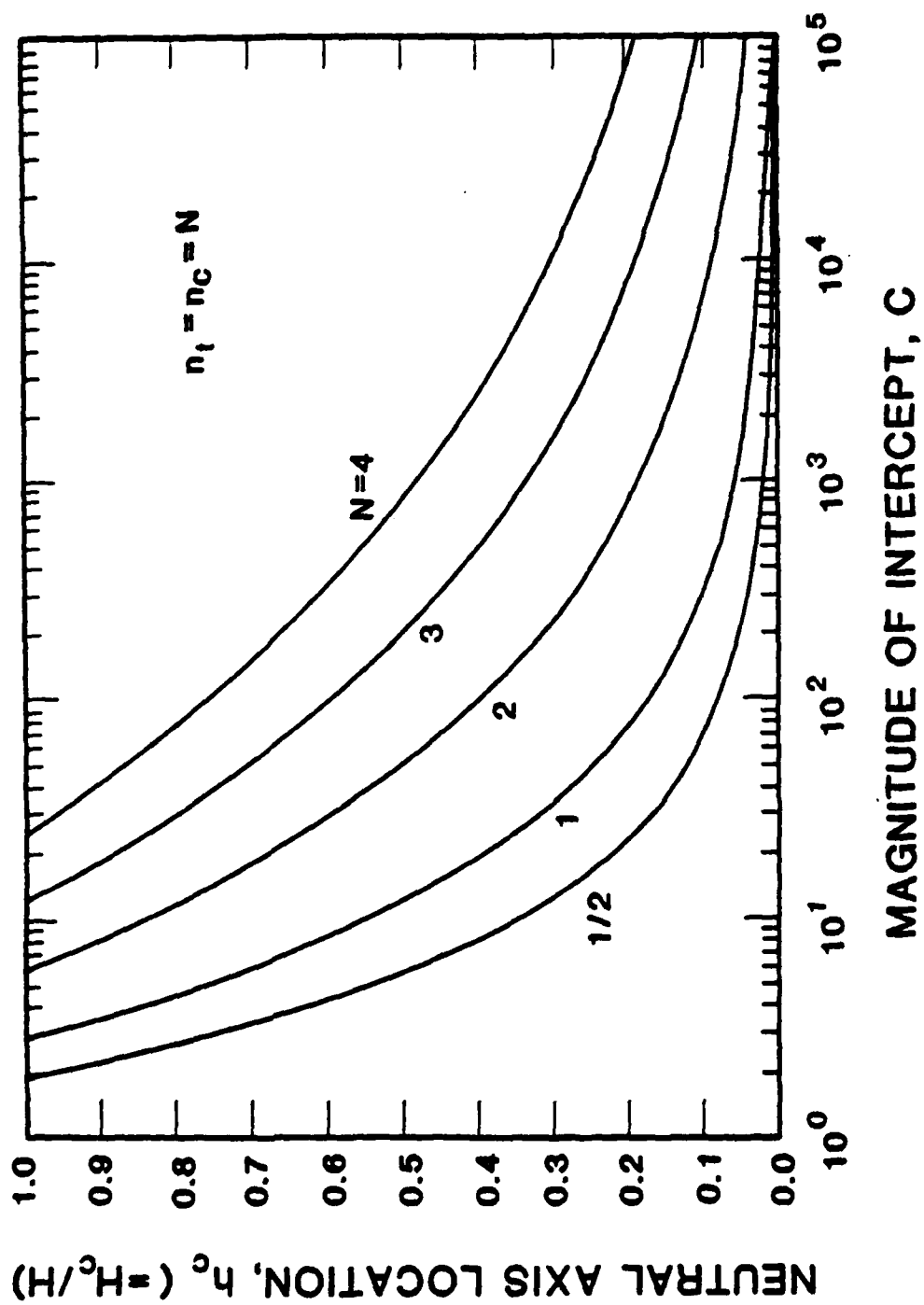


Fig. 12. Plots of h_c vs C , C being the intercept of the linear curves on \dot{k} vs m at $m = 1$, thus is a measurable parameter.

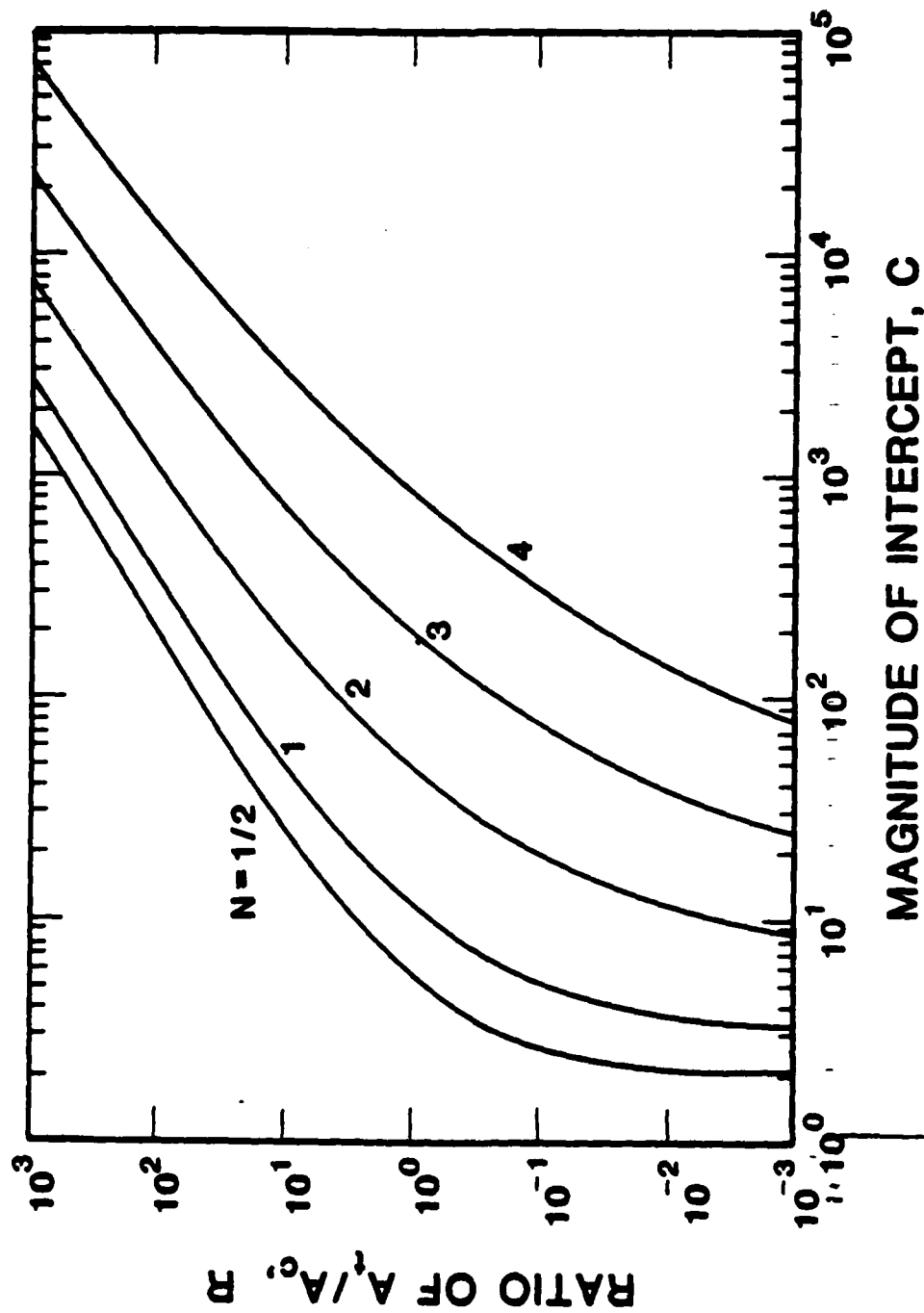


Fig. 13. Plots of R vs C for the same fixed value of N .

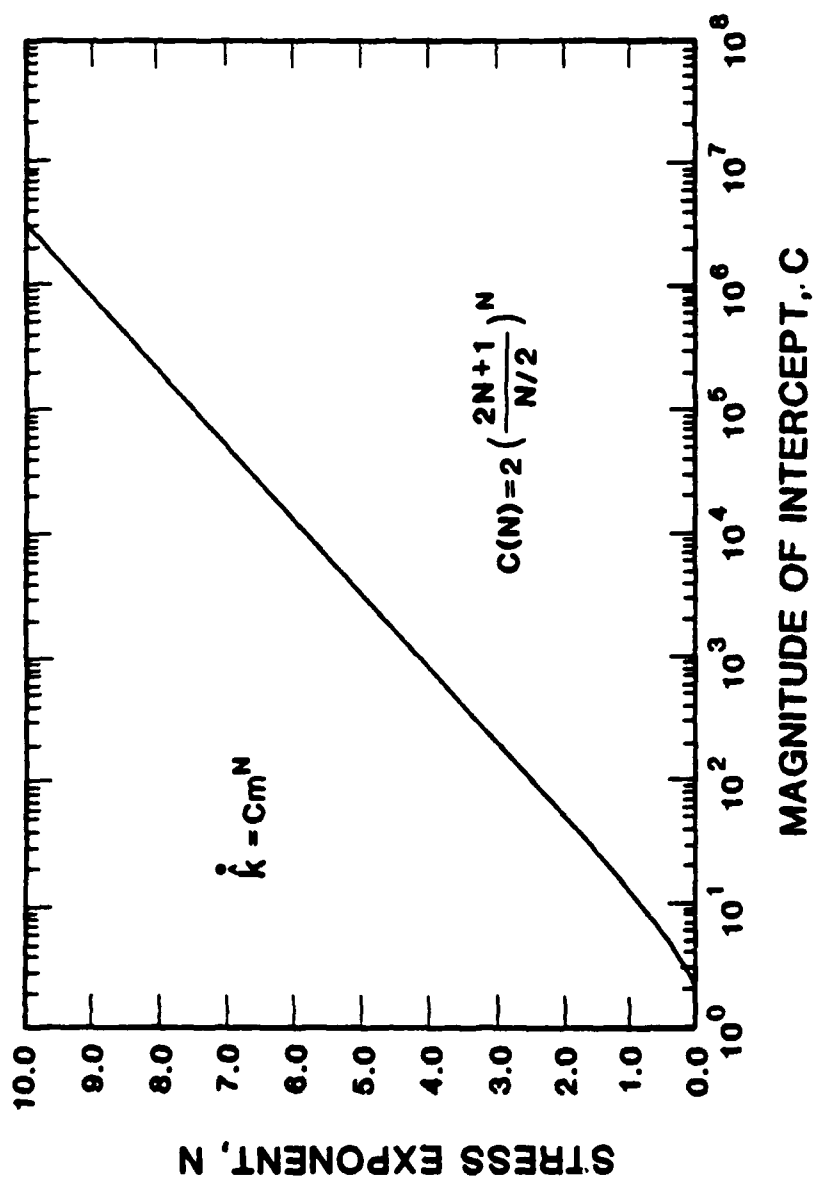


Fig. 14. Plots of N vs C when $R = 1$ and $n_t = n_c = N$.

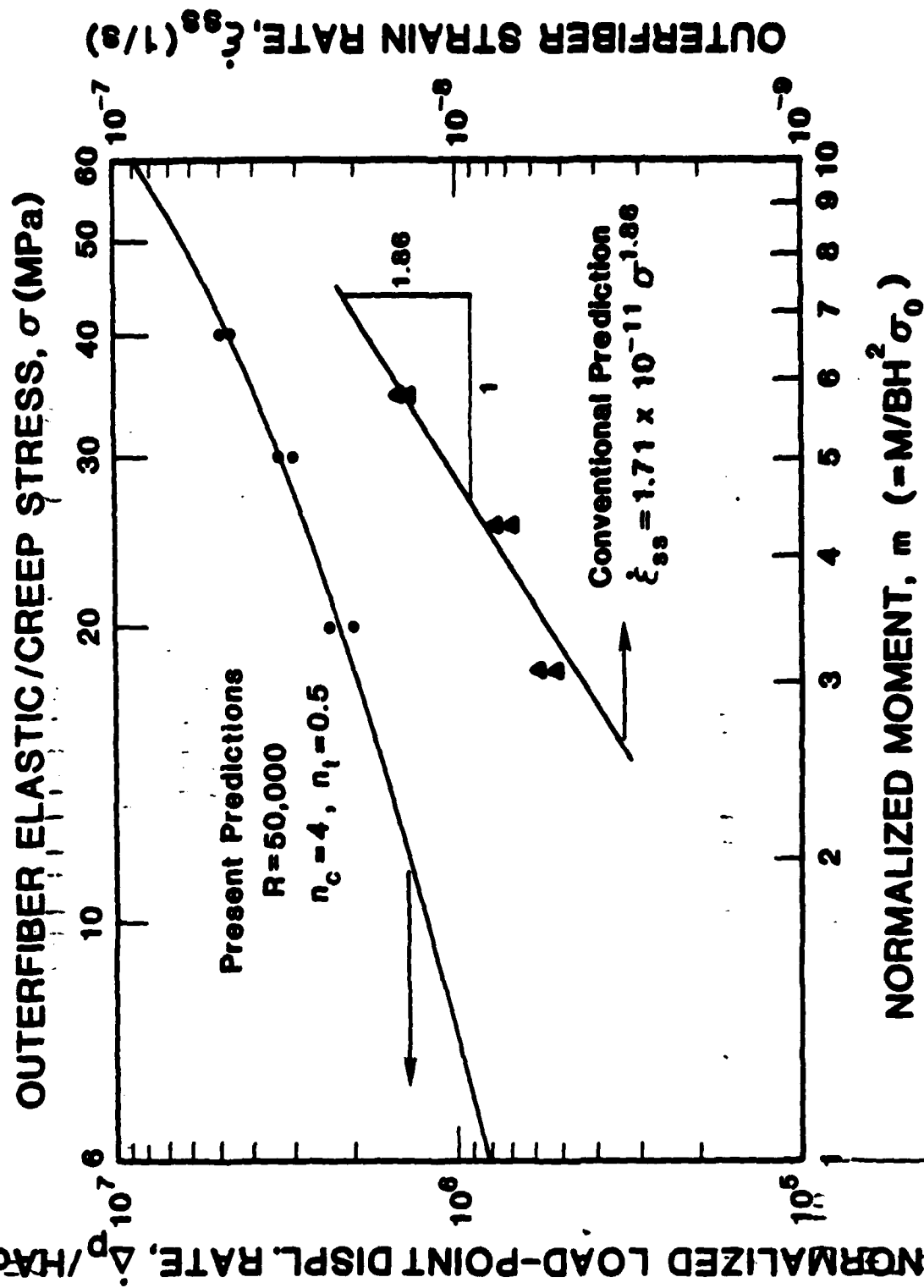


Fig. 15. Plot of four-point bend test data on glass alumina crept at 1100°C in the space of $\log (\dot{\Delta}_p/H\sigma_0)$ versus $\log m$ indicating a good match at a solution for $R = 50,000$, $n_0 = 4$ and $n_1 = 1/2$. The power-law creep parameters are then predicted as $\dot{\epsilon}_0 = 0.85 \times 10^{-13} s^{-1}$, $n_0 = 4$; $A_t = 4.25 \times 10^{-9} s^{-1}$, $n_t = 1/2$. For comparison purposes, a linear plot based on the conventional method is also given.

(THIS PAGE IS BLANK)

STRUCTURAL RELIABILITY OF CERAMIC MATERIALS
S. M. WIEDERHORN AND E. R. FULLER, Jr.
NATIONAL BUREAU OF STANDARDS
GAITHERSBURG, MD. 20899

presented at Ceramics, Jerusalem '84
Jerusalem, Israel
December, 16-20 1984

J. Mat. Sci. and Eng., to be published

(THIS PAGE IS BLANK)

STRUCTURAL RELIABILITY OF CERAMIC MATERIALS
S. M. WIEDERMANN AND E. R. FULLER, Jr.
NATIONAL BUREAU OF STANDARDS
GAITHERSBURG, MD. 20899

ABSTRACT

The effect of materials properties on the structural reliability of ceramics is reviewed. For low temperature applications, methods for estimating reliability are in an advanced state of development. The parametric equations that are used to describe failure can be explained in terms of a crack growth model in which failure occurs primarily as the result of the growth of defects from a subcritical to a critical size. Recent modifications of this model have made it possible to explain microstructure and residual stress effects in terms of R-curve behavior. As a consequence, reliability techniques can be applied to most fine ceramics at room temperature. At elevated temperature, however, methods of assessing reliability are not as well developed. At high levels of applied load, failure occurs by subcritical crack growth from preexisting flaws. In which case, failure is governed by the same equations that govern failure at room temperature. At low levels of applied load, failure occurs by creep rupture, which involves the generation of new flaws by the creep process. Because failure by creep rupture is not yet well characterized theoretically, lifetimes are given only in terms of parametric representation of the controlling variables.

STRUCTURAL RELIABILITY OF CERAMIC MATERIALS
S. W. NIEDERHORN AND E. A. FULLER, Jr.
NATIONAL BUREAU OF STANDARDS
GAITHERSBURG, MD. 20899

INTRODUCTION

Concepts of reliability are applicable to all fields of engineering design and have been used widely on electronic and structural components and assemblies[1,2]. In structural materials, reliability is a term related to acceptable performance of a component for a specified period of time. This term is defined as the probability of survival up to a given time, and as such, it is concerned with the statistics of failure times. Failure time is the most important variable in reliability theory because it establishes an absolute limit to the useful lifetime of a component. To establish the reliability of structural materials, parameters such as strength and stress have to be related to the failure time. Once this is done, the reliability can be calculated and expressed in a way that can be used for material or component selection. This is best done in terms of hazard functions, which give the failure rate normalized to the number of components in the surviving population. Hazard functions can be represented by bathtub curves which express the failure rate as a function of time, figure 1.

This paper presents a discussion of the effect of material properties on the mechanical reliability of ceramic materials. The subject is considered from a broad perspective, to include ceramics that are used in both structural and non-structural applications. For any given application, an acceptable theory of reliability should enable the engineer or designer to select an allowable stress that will permit a

component to function for the expected lifetime with a low probability of failure. At low temperatures, acceptable theories of lifetime have been developed for a wide range of applications. The basis of these theories will be summarized briefly in this paper, stressing the importance of fracture mechanics as a means of lifetime prediction. Problems that arise as a consequence of residual stresses and microstructure will then be discussed, and a method of handling these problems will be presented. The problems that arise when ceramic materials are used at elevated temperatures will also be discussed, and the application of non-fracture mechanics methods of lifetime prediction will be explored.

FRACTURE MECHANICS BASIS FOR DESIGN

The theory of structural reliability of ceramic materials starts with the work of Griffith[1], which assumes that the strength of a solid can be related to the size of a critical crack, c , contained within the solid, and to the surface free energy, γ , of the solid:

$$S = \sqrt{2\gamma E} / c \quad (1)$$

where S is Young's modulus of the material.

In modern fracture mechanics terminology, equation 1 can be expressed in terms of the critical stress intensity factor, K_{Ic} for crack growth:

$$S = K_{Ic} / \sqrt{c} \quad (2)$$

stress σ is a function determined by the crack and specimen geometry. For
 straight and penny shaped cracks, f has a value that ranges from
 approximately 1.0 to approximately 1.8[4]. The critical stress intensity
 factor K_{IC} is considered to be a materials constant, and small cracks in ceramic
 materials are considered to behave in exactly the same way as large cracks
 in ductile materials. This assumption may not be true when
 microstructural and residual stress effects play a role in determining
 crack growth resistance. It is important to emphasize that equation 2
 represents a failure criterion. When this equation is satisfied, and
 when the failure stress for ductile materials increases with crack length more
 rapidly than the fracture resistance, then failure is assumed to occur.
 When materials properties or microstructure are of
 importance in the fracture process, then equation 2 will have to be
 modified.

Equation 1 shows that a simple hypothesis of strength on crack length.
 This hypothesis has been used previously, however, when introduced into the formalism,
 based on the assumption of constant failure and subcritical crack growth
 it leads to a contradiction. It is clear to anyone that delayed failure
 involves the growth of cracks, cracks or other types of defects that
 are considered to be the cause of failure. It is also clear to
 anyone that the strength of a material is considered to be a function of
 the applied stress. Equation 1 is

where v_0 and n are empirically determined constants and K_0 is a normalization constant.

The applied stress intensity factor is expressed in terms of the crack length, c , and the applied stress, σ :

$$K_1 = \sigma Y \sqrt{c} \quad (4)$$

From equations 2, 3 and 4 it can be shown that strength, S , and its time dependence are determined by the initial component strength, S_i , and an integral that depends on time[6]:

$$S^{n-2} = S_i^{n-2} - (1/B) \int_0^t \sigma^n(t) dt \quad (5)$$

where the constant B depends on the critical stress intensity factor, and the crack growth parameters v_0 and n :

$$1/B = [(n-2)v_0 Y^2 K_{1c}^{n-2}]/(2K_0^n) \quad (6)$$

If any of the constants in equation 6 also depend on time they too must be included within the integral sign.

The strength degradation integral shown in equation 5 can be easily evaluated when the applied stress is known as a function of time. When n and B are constant, the value of this integral completely determines the strength loss during any application. Although not expressed exactly in the form given above, this integral has been evaluated for a number of practical situations involving time dependent stresses, including: constant load[7,8], constant rate of loading[7-10], cyclic loading[11], and thermal shock[12]. Equation 5 relates strength to time and thus provides an essential link between the time-to-failure and the initial strength of the material. Since the initial strength depends on the flaws contained within the material, the equation relates failure time to initial crack size.

To complete the theory, it is necessary to express the initial strength in terms of some measure of its central value and its spread in values. For ceramic materials, the initial strength distribution is often expressed in terms of a two parameter Weibull distribution for which

$$S_1 = S_0 (\ln (1-P)^{-1})^{1/m} \quad (7)$$

where S_0 and m are the Weibull scale and shape factors, respectively: S_0 is a parameter that gives a measure of the central tendency of the strength, whereas m is a parameter that gives a measure of the scatter of the strength. The variable, P , is the cumulative failure probability, which is commonly used in reliability theory[1].

By substituting equation 7 into equation 5 an equation is obtained in which the strength is expressed in terms of the cumulative failure probability, P , the fracture parameters B and n , and the statistical parameters S_0 and m .

$$S^{n-2} = S_0^{n-2} [\ln(1-P)^{-1}]^{\frac{n-2}{m}} - (1/B) \int_0^t \sigma^n(t) dt \quad (8)$$

When the applied stress is assumed to be a constant and $S_1 \gg S = \sigma$, then the time-to-failure can be expressed in terms of failure probability with the following expression:

$$t = t_0 [\ln(1-P)^{-1}]^{1/m'} \quad (9)$$

where $t_0 = B\sigma^{-n} S_0^{n-2}$ and $m' = m/(n-2)$. It is worth noting that equation 9 has exactly the same form as equation 7. The failure time is now expressed in terms of a two parameter Weibull distribution, in which the shape parameter, m' , and the scaling parameter, t_0 , are related to the applied stress, σ , the crack propagation constants, v_0 and n , and the shape, m , and scaling, S_0 , parameters of the initial strength distribution. This connection between the distribution in failure times, and the distribution in strength was first reported by Paluszny[13].

For ceramic materials, m is usually smaller than n which means that the Weibull shape parameter for the failure time will have a value that is less than 1. For ordinary glass, for example, $m=7$ and $n=16$, so that

$m' = 0.5$. This result is significant because small or fractional values of m' result in failures that occur over several orders of magnitude in time. This prediction is consistent with data obtained on glass[14] and on aluminum oxide[15]. In figure 2, for example, a Weibull representation of the failure time is given for glass bonded aluminum oxide (AD-96). As can be seen, the slope of the Weibull plot is approximately 0.25, which is consistent with the value of $m' = 0.18$ (calculated from $n = 55$ and $m = 9.8$) for this material[15].

A more complete discussion of the application of probability theory to lifetime prediction was given by Paluszny[13], who also developed the equations for bathtub curves from equation 9. Paluszny noted that when m' is less than 1, the hazard rate and hence the risk of failure decreases with time. This type of failure is typical of that occurring as a consequence of manufacturing defects and hence represents the initial portion of the bathtub curve. On the other hand when m' is greater than 1, the hazard rate increases with time and the curve represents the wear-out portion of the bathtub curve.

By eliminating weak components from the initial strength distribution, proof testing or nondestructive evaluation can be used to improve the reliability of ceramic materials at room temperature. Once the weak specimens have been eliminated, a specific amount of time is required before enough crack growth has occurred to break the weakest specimen remaining in the distribution. In this case, there will be a

period of time over which no failures occur after the load has been applied. If the truncation strength is given by the proof test stress, σ_p , then the minimum time-to-failure, t_{min} , is given by[8,16]

$$t_{min} = B \sigma^{-n} \sigma_p^{n-2} \quad (10)$$

This equation makes no reference to failure probability; every term in the equation can be evaluated experimentally, and in principle, "guess-work" in predicting the lifetime of a component is eliminated. Thus, once the initial strength distribution has been truncated, the prediction of lifetime is entirely deterministic.

Proof testing has been shown to work for vitreous grinding wheels and for glass under laboratory conditions for which the test environment can be controlled[8,16-18], figure 3. The possibility of truncating strength distributions has also been demonstrated on hot-pressed silicon nitride[19], alumina[20], and silica-fiber tiles[21]. For proof testing to be effective, it is necessary to avoid: (1) the introduction of new flaw populations during or subsequent to the proof test; and (2) the intensification (by crack growth) of flaws that are already present in the component. In situations where moisture contributes to subcritical crack growth, dry test conditions and relatively rapid unloading rates are required to sharply truncate distributions[22]. Where compressive forces and contact loads are important to component function, care has to be taken to avoid the introduction of cracks as a result of the contact loads during the proof test[23]. If these precautions cannot be exercised, then the strength distribution after the proof test may be worse than the

initial distribution[22,24]. Despite these drawbacks, proof-testing has been used in a number of applications including space-craft windows[25,26], optical fibers[27] and heat engine rotors[28]. Today proof testing is probably the most widely accepted means of assuring component reliability in structural applications.

Nondestructive testing is more difficult to use in ceramic applications for several reasons. First, the flaws and defects that cause failure in ceramic materials are small and therefore difficult to detect by conventional nondestructive testing techniques. In glass, for example, the surface cracks that are responsible for strength degradation are typically on the order of 10 to 100 microns; flaws in polycrystalline ceramics are of about the same magnitude in size. Flaws of this size cannot be imaged by x-ray techniques with the resolution needed for lifetime prediction even when scattering conditions are favorable. Although dye-penetration techniques are capable of detecting flaws of this magnitude, the technique is tedious and only reveals the surface trace of the flaw. No information is obtained on the flaw depth, so that the flaw severity vis-a-vis mechanical loading is difficult to estimate. Although dye penetration is used for process control for ceramics, its application as a quantitative technique for estimating flaw size is probably not feasible.

Acoustic techniques have also been considered as methods for detecting the presence of critical flaws in ceramic materials[29]. The ease of detecting defects depends on the type of defect and its location. Bulk defects (e.g. voids, inclusions, large grain aggregates) are

difficult to analyze by acoustic techniques and require complex equipment for complete characterization. In order to estimate the size, shape and type of defect, combinations of acoustic measurement techniques are needed including acoustic microscopy and low and high frequency scattering techniques. Although considerable advances have been made in the development of acoustic techniques, they are not yet being applied in a quantitative way to ceramics for predicting flaw severity.

By contrast to the above conclusions on bulk defects, some success has been experienced in the use of ultrasonic surface waves to detect machining damage in hot-pressed, silicon nitride. For surface damage, relationships between the detected flaws and the strength of the ceramic have been explored[30] and for laboratory tests, at least, agreement between measured and predicted strengths have been obtained, Table 1. A problem that has been experienced in these studies is that of crack closure. A closed crack gives a much weaker signal than an open crack and therefore may belie the serious nature of the critical flaw. This problem can be alleviated somewhat by applying a stress to the component in order to "open" critical flaws and thus permit their detection by the ultrasonic waves. Although feasible in some cases, this procedure complicates the testing.

A problem that is common to all nondestructive testing techniques is the evaluation of flaw severity once the flaw has been detected. Flaws in ceramic materials consist of foreign inclusions, pores and machining damage. As has been shown by Evans on hot-pressed silicon nitride, figure 4, the severity of defects is determined both by the defect size and by the defect type[29]. The ease of detecting defects does not depend

on their severity as strength limiting flaws, but on how different their chemical or mechanical properties are from the host material. Therefore, the usefulness of a nondestructive test technique depends on our ability to both image the flaw and characterize the flaw type so that the degree of severity of the particular flaw can be estimated. To date these problems are still being worked on, and the application of nondestructive test techniques to ceramic materials awaits their solution.

Before leaving this fracture mechanics approach for design, it is worth noting that the crack growth and fracture mechanics parameters B and n do not have to be obtained by fracture mechanics techniques. These parameters can also be obtained by more classical strength techniques[7,8]. Thus, the time-to-failure, t_g , for a constant applied stress, σ , is obtained from equation 5 and is given by:

$$t_g = B \sigma^{-n} S_1^{n-2} \quad (11)$$

where S_1 is now some fixed value of the strength, for example, the median strength. By applying a series of fixed stresses to a set of specimens and plotting the median failure time versus applied stress on a logarithmic representation, the value of n can be determined from the slope of the line. The value of B is determined from the intercept of the line, and from independent measurements of the strength, S_1 , under conditions that preclude subcritical crack growth.

The constants, B and n can also be evaluated by using a constant loading rate to failure[7,8]. In this case the time-to-failure, t_d , is related to the loading rate, $\dot{\sigma}$, and the failure stress, σ : $t_d = \sigma/\dot{\sigma}$ (subscript d is used to indicate dynamic rather than static loading). By substituting this equation into equation 5 the time-to-failure under a constant rate of loading is given by[7]:

$$t_d = (n+1) t_s \quad (12)$$

Again, by plotting the failure time against the failure stress, the value of B and n can be determined.

The two strength methods of determining the fatigue constants, B and n, provide an alternative to the fracture mechanics method of determining these constants. As noted by Davidge et al.[7] and by Ritter et al.[8], the strength techniques are used to obtain data on the same flaws that limit the strength and failure time of structural ceramics. In theory, the same values of n and B should be obtained regardless of which technique is used for their measurement, and as shown in figure 5, compatibility of the experimental techniques is obtained for some materials[31]. For others, microstructural effects preclude the interchangeable use of strength and fracture mechanics techniques for determining B and n. In this case, modification of the theory is necessary to account for the behavior of cracks in ceramic materials.

MICROSTRUCTURAL EFFECTS

Up to this point in the paper, ceramic components have been assumed to be homogeneous and isotropic so that linear elastic fracture mechanics can be applied regardless of crack size. When this assumption is valid, then the constants that describe component fatigue can be obtained either by crack growth or by strength techniques, as is indicated in figure 5. However, when the assumption is not valid, then crack growth and strength techniques often give disparate values for the fatigue parameters, figure 6, and some judgement must be exercised in deciding on which set of parameters to use for lifetime predictions. In polycrystalline ceramic materials there seem to be at least two reasons for this lack of agreement between fatigue constants: (1) localized residual stresses introduced by machining operations provide an additional driving force for fracture; and (2) interactions of the crack with the microstructure results in a variable resistance to crack growth. Because of these microstructural considerations, modification of the theory presented above is necessary to account for the effect of microstructure on design lifetime. These modifications are discussed below.

In polycrystalline ceramic materials, microstructural effects occur because cracks encounter a changing microstructure as they grow larger. If a crack is small compared to the microstructure, crack stability and the resistance to crack growth is determined by local details of the microstructure, such as by the particular grain or grain boundary in which the crack is located. As the crack increases in size, the resistance to crack growth gradually changes from that characterized by a single grain

or grain boundary to that characterized by the polycrystalline material. Resistance to crack growth is enhanced by crack deflections caused by inclusions and by grain boundaries in the material. Often second phase inclusions such as fibers or meta-stable phases are added to the material to enhance crack tip deflection and in this way to increase the materials toughness. Furthermore, if the material consists of non-cubic grains, then localized stresses resulting from anisotropic thermal expansion can also contribute to an increase in toughness of the ceramic as the crack grows. This type of behavior can be represented in terms of a rising R-curve, in which the stress intensity factor characterizing the resistance to crack advance is given as a function of the change in crack size. For example, data of this type has been obtained for aluminum oxide(32). Figure 7, which shows that the resistance to fracture, as characterized by K_I , increases by a factor of approximately 2, as the crack grows. If the applied K_I increases less rapidly than the resistance to crack growth, then the crack remains stable as it grows and the applied stresses must be increased for failure to occur.

Localized residual stresses in the surface of ceramic components influence crack growth in a way that is very similar to that resulting from the effects discussed with regard to microstructure. When a hard particle makes contact with a ceramic surface, a plastic impression surrounded by radial cracks is left behind. Residual stresses at the indentation wedge the crack open, and contribute to the driving force for fracture when an external load is applied(33-35). To obtain the total driving force for fracture, the residual stresses have to be added to those from the external load. Since the residual stresses load the

surface crack at its center, the effectiveness of these stresses for crack growth decreases as the crack grows larger. Thus, the external stresses must be increased to provide sufficient driving force for fracture. If the loading is stopped, the crack will arrest. As in the case of a rising R-curve, crack growth is stable. If the crack size were monitored as the crack grew larger, and if an applied stress intensity factor were calculated from the applied stress and the crack size (as in equation 4), then the applied stress intensity factor required for crack growth would increase as the crack grew larger. Thus even if the local resistance of the material to crack growth were constant as the crack grew larger, an apparent rising R-curve would be obtained as a consequence of residual stresses in the component surface. Curves of this type have been obtained recently by Marshall et al. on several ceramics and glasses [30]. Data for one specimen, silicon nitride, is illustrated in Figure 8.

The concept of a rising R-curve has not previously been combined with time-dependent crack growth for purposes of lifetime prediction. Recent advances in representing the effect of microstructure on fracture rates is possible to extend these methods to rising R-curve behavior. These methods have been developed by Marshall and Leach and their coworkers [33-36] and is being applied in a systematic fashion to a series of fine grain ceramics [35,37]. The method parallels the simple fracture mechanics method discussed earlier in the paper. However, the equation representing the stress intensity factor has to be changed in order to take account of the effect of residual stresses and microstructure on crack growth. As shown in the following equation [38,39],

$$K_1 = K_a + K_r + K_m$$

(13)

$$= Y \sigma/c = \frac{1}{2} P/c^{3/2} + \sqrt{Q}/c^{3/2}$$

the effective stress intensity driving the crack consists of three parts: K_a , resulting from the applied stress, K_r , due to the residual stresses, and K_m , due to the component microstructure. The mathematical forms of K_a and K_r are well documented in the literature; by contrast, the form of K_m has been assumed for mathematical simplicity. Despite its theoretical shortcomings, the inclusion of K_m in equation 13 does permit an evaluation of the effect of microstructure on component lifetime.

The conditions for crack instability are identical to those used in the simple fracture mechanics approach to component reliability:¹

$$K_I = K_{Ic} \quad (14)$$

$$dK_I/dc > 0 \quad (15)$$

From these equations it is possible to show that the strength of a component is given by the following equation:

$$S_c^2 = 0.472 K_{Ic}^{4/3} / Y (1P + \sqrt{Q})^{2/3} = 0.472 K_{Ic}^2 / Y c_0 \quad (16)$$

¹If the fracture resistance, R , is defined as $R = K_{Ic} - K_r - K_m$, then the conditions for instability can be written in terms of the R-curve as $K_a = R$ and $dR/dc > dR/dc$.

[illegible]

1. The first step is to identify the problem or question that needs to be answered. This involves understanding the context and the specific requirements of the task.

2. Next, it is essential to gather relevant information and data. This can be done through research, consultation with experts, or by analyzing existing resources.

3. Once the information is gathered, the next step is to analyze it. This involves breaking down the problem into smaller, more manageable parts and identifying the key factors that influence the outcome.

4. After analysis, a plan or strategy should be developed. This plan should outline the steps that need to be taken to solve the problem, taking into account the resources available and the potential challenges.

5. The final step is to implement the plan. This involves putting the strategy into action and monitoring the progress. If necessary, adjustments should be made along the way to ensure that the goal is achieved.

1. The first step is to identify the problem or question that needs to be answered. This involves understanding the context and the specific requirements of the task.

2. The second step is to gather relevant information and data. This can involve research, consultation with experts, or collecting data from various sources.

3. The third step is to analyze the information and data collected. This involves identifying patterns, trends, and relationships that can help in understanding the problem.

4. The fourth step is to develop a solution or answer. This involves applying the knowledge and skills gained from the previous steps to create a response that addresses the problem.

5. The fifth step is to evaluate the solution or answer. This involves checking the results against the original problem and requirements to ensure that the solution is effective and accurate.

also on the size of critical flaws viz-a-viz the microstructure. Thus, while polycrystalline aluminum oxide may be stronger and tougher than sapphire for large flaws, the reverse is clearly true for small flaws. The polycrystalline aluminum oxide is limited in strength as the flaw size decreases, whereas the sapphire continues to become stronger. By controlling μ and ν in equation 16, it should be possible to control the strength of ceramic materials to some extent.

Failure time is introduced into the formalism in the same way as with the more simple fracture mechanics approach to lifetime prediction. Failure is assumed to occur by the growth of cracks from subcritical to a critical size, but now the criteria for crack instability, equations 14 and 15, include terms that account for the effect of a rising R-curve. As in the earlier treatment, the rate at which the crack grows is given by equation 3. However, the expression for the stress intensity factor, equation 12, also contains terms to account for the effect of a rising R-curve. Using equations 3 and 12 through 15 as the starting equations, Fisher et al. [15] obtained the following solution for the time-to-failure under constant stress conditions:

$$t = \frac{1}{\dot{a}} \left(\frac{S_1'}{S_0} \right)^{n'} \left(\frac{S_1'}{S_0} \right)^{2} \quad (17)$$

where, n' and $2'$ are related to the fatigue parameters n and 2 obtained from fracture mechanics measurements on large cracks: $n' = 3n/4 + 1/2$; $2' = 1 + n \left(\frac{S_1'}{S_0} \right)^{n'} + 2' \left(\frac{S_1'}{S_0} \right)^{2}$. The expression for the strength, S_1' , is given by equation 16. Note that the time-to-failure equation, equation

17, is similar in form to that developed from the more simple theory. The fatigue parameters n' and B' differ from n and B as a direct consequence of the existence of microstructure or residual indentation stresses. The values of n' and B' depend on the type of flaw² (e.g. point vs. line flaw), but not on the magnitude of the residual stress field, χP , or the details of the microstructure, such as grain size. Changes in the microstructure affect fatigue lifetime only as they affect the inert strength of the components.

The effect of a rising R-curve on fatigue behavior is illustrated in figure 10 for glass that has been indented using a Vickers hardness indenter. As can be seen from this figure, the measured value of n' , 13.7, is close to the predicted value of n' , 13.9, calculated from n , 17.9, obtained on annealed glass specimens. This theory has also been shown to be in reasonable agreement with data obtained by dynamic fatigue measurements on other glasses and ceramics.[39]

Statistics can be introduced into the formalism for lifetime prediction in the same way as was done earlier for the simple fracture mechanics approach to delayed failure. Representing the inert strength S_i' by a Weibull distribution, the time-to-failure is expressed in terms of the failure probability by substituting equation 7 into equation 17. The expression for failure time is identical to equation 9 with n' , B' , and S_0' substituted for n , B , and S_0 , respectively. Since microstructural modifications only affect failure time through the strength, the distribution in failure times given by the Weibull parameters are entirely

²The equation given above for n' and B' are for point flaws[36].

dependent on those parameters that affect strength: i.e. on χP and μQ of equation 16. Thus, the scatter in the time-to-failure is determined by the scatter in χP and μQ of equation 16. These results suggest that the formalism developed earlier can be used, almost in its entirety for the prediction of component lifetime when microstructural effects are important. In fact, provided fatigue data are obtained by strength techniques, the formalism is identical to that developed earlier.

Nondestructive evaluation techniques can be introduced by using equation 16 to represent the strength of a component. If the strength distribution is truncated by nondestructive evaluation, all components with crack sizes greater than a given initial value of c_0 will be eliminated. As with the previous procedure, this sets a lower limit to the strength and a minimum value to the failure time. Although proof-testing can be used in the same way, a rather subtle difficulty arises with proof-testing, because R-curve effects always lead to stable crack growth during the proof-test cycle. Crack growth in the component that barely passes the proof-test will have occurred to a point just below that of instability, so that the cracks will be longer after the proof-test than they were before. As a consequence, the crack will not have to grow as far before failure occurs and the time-to-failure will be less than that given by equation 17. Quantitative aspects of crack growth during proof-testing are still to be investigated, so that it is uncertain at the present time how important this problem will be to lifetime prediction.

EFFECT OF TEMPERATURE ON STRUCTURAL RELIABILITY

The theories of reliability discussed above are not fully applicable at elevated temperatures where ceramic structures are no longer chemically or physically inert. Chemical reactions between ceramics and the environment lead to the formation of new populations of flaws or result in chemical modification of the component microstructure, both of which affect strength and mechanical behavior. The kinetics of physical transformations and chemical processes are also enhanced by increasing the temperature. Transport processes such as viscous flow or diffusion, for example, are highly temperature dependent and are greatly accelerated by increasing the temperature. As a consequence, those chemical reactions and physical transformations that depend on transport processes are also accelerated by increasing the temperature. Thus, crack nucleation and crack growth have been observed to occur at elevated temperatures as a result of creep[40-42], which in turn depends on the occurrence of diffusion or viscous flow. These thermally induced changes in the flaw population and in the mechanisms that are responsible for mechanical failure invalidate the assumptions made in developing the theories of reliability presented above. No longer is crack growth the only process to be considered in establishing component lifetime, nor are the flaw populations or the stresses that cause failure invariant in time. In this situation, deterministic aspects of lifetime prediction are lost and alternate approaches to lifetime prediction must be developed. In this section some of the experimental data that lead to this conclusion are discussed, and possible alternative approaches to structural reliability at elevated temperatures are investigated.

The kinds of flaw population changes that occur at elevated temperature and their effect on strength are illustrated in figure 11[43] for a grade of magnesia doped, hot-pressed silicon nitride (NC-132), a material that has been considered for high temperature structural applications. The initial flaw population in this material results from machining operations which leave mechanical damage in the specimen surface. The damage is very similar to that introduced by hardness indentations with their plastic deformation zones and associated cracks. These cracks are the normal fracture sources when structural components are subjected to sufficiently high stresses. If the applied stresses at elevated temperatures are not high enough to break the components immediately or to cause failure by subcritical crack growth, then the effectiveness of the cracks as stress concentrators is diminished by annealing of the residual stresses that are associated with the mechanical damage. In addition to annealing of residual stresses, chemical attack (e.g., oxidation) on the indentation cracks results in blunting and healing of these cracks, which further reduces their severity as stress concentrators.

Because of the effect of high temperature environment, the strength of the silicon nitride initially increases with time, figure 11. With additional exposure, however, new defects, i.e. pits, form in the silicon nitride surface due to localized chemical corrosion at the specimen surface. When these pits are sufficiently large, they act as new fracture sources that now control specimen strength. Strength of components that contain large pits is observed to decrease, and failure no longer

originates from the mechanical damage, but from the pits. Finally, if the component is subjected to an external load for long times at elevated temperatures, creep eventually nucleates new cracks that act as sources of failure. When this occurs, component strength gradually decreases with time, and failure originates from creep initiated cracks rather than from the machining cracks that were first present in the component.

As indicated above, these changes in the flaw population have a significant influence on long-term reliability and delayed failure of ceramic materials. Such effects are illustrated by the work of Quinn[44] and Grathwohl[45], both of whom used indentation techniques to study the time evolution of mechanical damage in magnesia-doped, hot-pressed silicon nitride. Quinn obtained static fatigue curves for specimens of NC-132 into which he introduced controlled flaws by a Knoop indentation. He monitored the time to failure as a function of applied stress and temperature, and identified the origin of failure. In particular, he noted whether failure originated from the indentation or from some other source on the specimen surface. From his results, figure 12, Quinn concluded that at low stresses failure occurred primarily by creep-rupture, in which case, cracks were nucleated by the creep process. At high stresses, however, failure occurred by subcritical crack growth from the pre-existing flaws. Clearly, the indentation cracks had a chance to "heal" at low stresses so that they were no longer of sufficient severity to act as fracture origins.

Grathwohl's study was conducted exclusively at 1200 °C on a different composition of magnesia-doped, hot-pressed silicon nitride. Both creep and creep-rupture studies were conducted. Grathwohl demonstrated that the strain-to-failure and the time-to-failure depended on whether the specimen contained indentation damage, figure 13. At low applied loads, the indentation damage was unimportant as failures did not originate from the indentations. The strain-to-failure was the same for specimens that contained indentations as for smooth bar specimens. At high applied loads, the strain-to-failure was again identical for the indented and the smooth bar specimens, however, now failures in the indented specimens originated from the indentations. In the intermediate range of stresses, the strain-to-failure was very different for the two sets of specimens. Grathwohl's conclusions were similar to those of Quinn. At high levels of stress, the failure was stress controlled and occurred by slow crack growth; whereas at low levels of stress, failure occurred by creep-rupture which generates new cracks.

The results obtained by Quinn, Grathwohl and others (Wiederhorn and Tighe[46], Evans[47], Fuller et al.[48]) suggest that for short time periods, failure occurs by crack growth from preexisting flaws, in which case the time-to-failure is given by the integration of equation 5. The time dependent stress in the integral of equation 5 must not only include the applied stress due to external loading, but also relaxation of that stress due to creep, and relaxation of the residual stresses that were present as a result of the mechanical damage. As in other examples of failure due to crack growth, the statistics of failure can be included in equation 5 by use of a Weibull representation of the flaw population. In

this way, failure by crack growth can be treated in a similar fashion to that used in earlier sections of the paper. Thus, when crack growth controls failure, the effect of temperature is simply to modify but not to drastically alter the approach to structural reliability discussed above[49]. Since crack growth induced failures occur over a relatively short time, they represent the defect stage of the bathtub curve. Elimination of these defect induced failures will depend on manufacturing process control and the application of proof testing or nondestructive testing techniques to remove defective parts from service. Although methods of removing defective parts from service are in principal understood, they have not been applied to structural components for high temperature use, and a data base has yet to be collected for high temperature applications.

When creep-rupture occurs (low applied stresses and high temperatures), a new approach is required to assure component reliability. At the present time, two general types of studies have been conducted to understand the creep-rupture process: those directed at obtaining parametric representations of the creep-rupture process, and those directed towards a theoretical and experimental understanding of the mechanisms that control creep-rupture. Several excellent reviews of creep-rupture mechanisms of failure in ceramic materials have been presented recently[50-53]. Failure mechanisms are classified according to material: those with a second phase, usually glass, at the grain boundary; and those that have no second phase at the grain boundary. In either case, the kinetics of microcrack nucleation, crack coalescence and crack propagation are developed, and the time-to-failure is estimated by

assuming that one of these is the rate limiting step for failure. Results are usually presented in the form of parametric relationships between failure time, temperature, applied stress and strain rate. Although the constants in these relations are given in terms of physical quantities, they are often not easily measured, so that empirical determination of the constants for purposes of lifetime prediction is necessary. The advantages of these theories is that they describe component lifetime in terms of microstructure, temperature and applied load. For most of these theories, the experiments to validate and define limits of the theories have not yet been conducted. In the one case for which a quantitative comparison between theory and experiment was attempted, the experimental data did not fit the existing theories[54]. Clearly, considerable additional work is required before the fundamentals of creep-rupture in ceramics are understood.

On a more practical level, parametric studies have been conducted by a number of investigators on various grades of hot pressed silicon nitride and aluminum oxide, to obtain empirical relationships between applied stress, strain, and temperature. The earliest experiments of this type were conducted in pure tensile stress by Kossowsky et al.[55] who showed that creep-rupture data for magnesia doped, hot pressed silicon nitride (MS-130) fit the Monkman-Grant[56] relation for creep, figure 14.

$$\dot{\epsilon} \epsilon^a = \dot{\epsilon}_0$$

(18)

where $\dot{\epsilon}$ is the minimum creep rate, ϵ is a constant and the Monkman-Grant exponent, a , has a value close to 1.

The creep of another grade of magnesia-doped, hot-pressed silicon nitride (from Annamark GmbH) was studied by Grathwohl[45], who confirmed Kossowsky's finding that rupture data in the creep regime fit the Monkman-Grant relation. Grathwohl also measured the strain-to-failure and found that the strain was a constant in the creep-rupture regime as would be expected from the Monkman-Grant relation. Consequently, Grathwohl put forth the idea of a strain limited rupture criterion, in which the time-to-failure was determined by the time for creep to reach a given strain. For materials that obey the Monkman-Grant relation, this idea is a valid basis for structural design.

Recent studies on aluminum oxide suggest that not all materials obey the simple Monkman-Grant relation in the creep-rupture regime. Johnson et al.[54], for example, showed that a stress modified Monkman-Grant relation was applicable in the case of a fine-grained, hot-pressed aluminum oxide:

$$\dot{\epsilon} \dot{\epsilon}_0^{-1} = A \sigma^n$$

where, n , is a stress exponent. The exponent, s , of the strain rate, $\dot{\epsilon}$, has been assumed equal to 1. A second set of creep-rupture studies by Wiederhorn et al.[55] and by Jaksis et al.[56], on a vitreous bonded grade of aluminum oxide, supported the conclusions reached by Johnson et al. Both sets of data suggest a value for the stress exponent of approximately 4 to 5 in the modified Monkman-Grant relation. These results suggest that the strain-to-failure is not a constant for aluminum oxide, but depends on

the applied stress. This conclusion is seen graphically in the data by Wiederhorn et al., which indicate a dependence of strain at failure on the applied stress, figure 15.

Although the above data support the idea that creep-rupture is determined by a parametric relation of the type given in equations 18 or 19, there is evidence that creep-rupture behavior of some materials differs significantly from that discussed above. Data by Wiederhorn and Figue[59], for example, on yttria-doped, hot-pressed silicon nitride are not consistent with the Monkman-Grant relation. Studies of the microstructure of this material by transmission electron microscopy can be used to rationalize this observation, since a change in the creep mechanism occurs at a temperature greater than approximately 1300 °C[42]. Below this temperature, the yttria and the magnesia doped materials are somewhat similar in their behavior, even though the yttria doped material is more creep resistant. At 1300 °C the grain boundary phase of the yttria doped material appears to decompose, resulting in a change in creep rupture mechanism, so that the fact that the Monkman-Grant relation does not seem to be obeyed is not surprising. Considering this finding, the Monkman-Grant relation can not be assumed for all polycrystalline ceramic materials. Instead the validity of the relation has to be tested for each material. Concurrently, data should be obtained to determine the mechanisms of failure for each material. Despite this drawback, when parametric relations are obeyed, they form a basis for structural design and can be used for prediction of component lifetime.

Another element of structural reliability is the ability to determine scatter in component lifetime. In the creep-rupture regime, the scatter in the time-to-failure is not nearly as great as that for delayed failure at room temperature. This conclusion is evident from extensive stress-rupture data published by Deibel [6], which indicate that failure times usually fall within a factor of two of the median failure time. This behavior is a considerable advantage over that at room temperature. The narrowing of the time-to-failure distribution by high temperature creep processes partially overstates the need for statistical information on the time-to-failure. In this regard, the failure of ceramic materials at elevated temperatures is similar to that experienced by metals under creep-rupture conditions. Therefore, if parametric models are shown to fit experimental creep-rupture data, one can expect the failure time to be accurate to within approximately one order of magnitude.

Finally, it can be noted that creep-rupture defines a natural upper limit to the lifetime of materials that deform by creep. Ceramics are semi-brittle materials, which do not permit generalized deformation on the microstructural level. Once creep has been initiated in ceramics, failure will eventually occur as the result of a stress buildup at inclusions, large grained agglomerates, or other inhomogeneities. The only way to prevent creep induced failure is to prevent the creep, so that in contrast to failures that occur by the propagation of preexisting flaws, failure in the creep regime depends more on the average structure of the component than on specific defects or flaws contained within the structure. Thus, failure by this mechanism defines the wear-out portion of the bathtub curve. Increasing the time to reach this wear-out limit can be

accomplished by processing techniques that improve the behavior of the material through modification of the bulk composition or grain boundary structure, or by reducing the engineering demands on the material. Both approaches have been used to extend the usefulness of structural ceramics in high-temperature applications.

SUMMARY

This paper presents a review of the techniques that have been developed to improve the structural reliability of ceramic materials. For low temperature applications the techniques are in an advanced state of development. The parametric equations that are used to describe failure can be explained in terms of a crack growth model, in which failure occurs primarily as a consequence of the growth of defects from a subcritical to a critical size. Fracture mechanics techniques are used to establish a method of structural design. The defects that are responsible for component failure are characterized by nondestructive evaluation, proof-testing and statistical methods, whereas fracture mechanics or strength techniques are used to obtain the constants that characterize subcritical crack growth. Recent developments in characterizing the influence of microstructure (and residual stress) on strength and fatigue provide a formalism for extending room-temperature reliability concepts to rising R-curve behavior. As a consequence, reliability techniques can, in principle, be applied to most fine ceramics at room temperature.

[illegible]

[illegible]

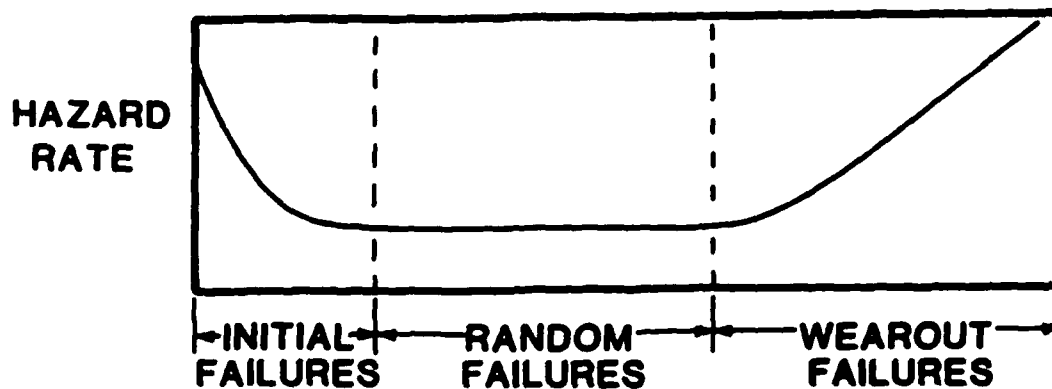
15. A.C. Gonzalez, H. Multhopp, R.F. Cook, B.R. Lawn and S.W. Freiman, in S.W. Freiman and C.M. Hudson (eds.), Methods of Assessing the Structural Reliability of Brittle Materials in ASTM STP 844, American Society for Testing and Materials, Philadelphia (1984) pp. 43-56.
16. A.G. Evans and S.M. Wiederhorn, Int. J. Frac. Mech., 10 (1974) 379.
17. J.E. Ritter, Jr. and J.A. Meisel, J. Am. Ceram. Soc. 59 (1976) 478.
18. J.E. Ritter and S.A. Wulf, Bull. Am. Ceram. Soc. 57 (1978) 186.
19. S.M. Wiederhorn and N.J. Tighe, J. Mat. Sci. 13 (1978) 1781.
20. K. Jakus, T. Service and J.E. Ritter, Jr., J. Am. Ceram. Soc. 63 (1980) 4.
21. D.J. Green, J.E. Ritter, Jr., and F.F. Lange, J. Am. Ceram. Soc. 65 (1982) 141.
22. J.E. Ritter, Jr., P.B. Oates, E.R. Fuller, Jr., and S.M. Wiederhorn, J. Mat. Sci. 15 (1980) 2275.
23. A.G. Evans, S.M. Wiederhorn, M. Linzer and E.R. Fuller, Jr., Am. Ceram. Soc. Bull. 54 (1975) 576.
24. S.M. Wiederhorn, S.W. Freiman, E.R. Fuller, Jr., and H. Richter, pp. 95-116 in Ref. 15.
25. S.M. Wiederhorn, A.G. Evans and D.E. Roberts, pp. 829-841 in Ref. 5.
26. S.M. Wiederhorn, A.G. Evans, E.R. Fuller and H. Johnson, J. Am. Ceram. Soc. 57 (1974) 319.
27. B.R. Turiyal, D. Kallish and M.R. Santana, Am. Ceram. Soc. Bull. 56 (1977) 224.
28. J.E. Harper, in E.M. Lenoir, R.W. Katz and J.J. Burke (eds.), Ceramics for High Performance Applications III Reliability, Plenum Press, New York (1983), pp. 123-149.

29. A.G. Evans, in F.L. Riley (ed.), Progress in Nitrogen Ceramics, Martinus Nijhoff Publishers, The Hague (1983), pp. 595-625.
30. D.B. Marshall, pp. 635-656 in Ref. 29.
31. B.J. Pletka and S.M. Wiederhorn, J. Mat. Sci. 17 (1982) 1247.
32. H. Hübner and W. Jillek, J. Mat. Sci. 12 (1977) 117.
33. D.B. Marshall and B.R. Lawn, J. Mat. Sci. 14 (1979) 2001.
34. D.B. Marshall, B.R. Lawn and P. Chantikul, J. Mat. Sci. 14 (1979) 2225.
35. B.R. Lawn, A.G. Evans and D.B. Marshall, J. Am. Ceram. Soc. 63 (1980) 532.
36. E.R. Fuller, B.R. Lawn and R.F. Cook, J. Am. Ceram. Soc. 66 (1983) 314.
37. R.F. Cook and B.R. Lawn, pp. 22-42 in Ref. 15.
38. B.R. Lawn, S.W. Freiman, T.L. Baker, D.D. Cobb and A.C. Gonzalez, J. Am. Ceram. Soc. 67 (1984) C67.
39. B.R. Lawn, Microstructure-Strength Properties in Ceramics, Parts I and II, J. Am. Ceram. Soc., to be published.
40. R. Morrell and K.H.G. Ashbee, J. Mat. Sci. 8 (1973) 1253.
41. F.F. Lange, B.I. Davis and D.R. Clarke, J. Mat. Sci. 15 (1980) 601.
42. N.J. Tighe, S.M. Wiederhorn, T.-J. Chuang and C.L. McDaniel, in R.E. Tressler and R.C. Bradt (eds.) Deformation of Ceramics II, Plenum Publishing Corp., New York (1984), pp. 587-604.
43. N.J. Tighe and S.M. Wiederhorn, in R.C. Bradt, A.G. Evans, D.P.H. Hasselman, and F.F. Lange (eds.), Fracture of Ceramic Materials, Vol. 5, Plenum Publishing Corp., New York (1983), pp. 403-23.
44. G.D. Quinn, pp. 177-193 in Ref. 15.

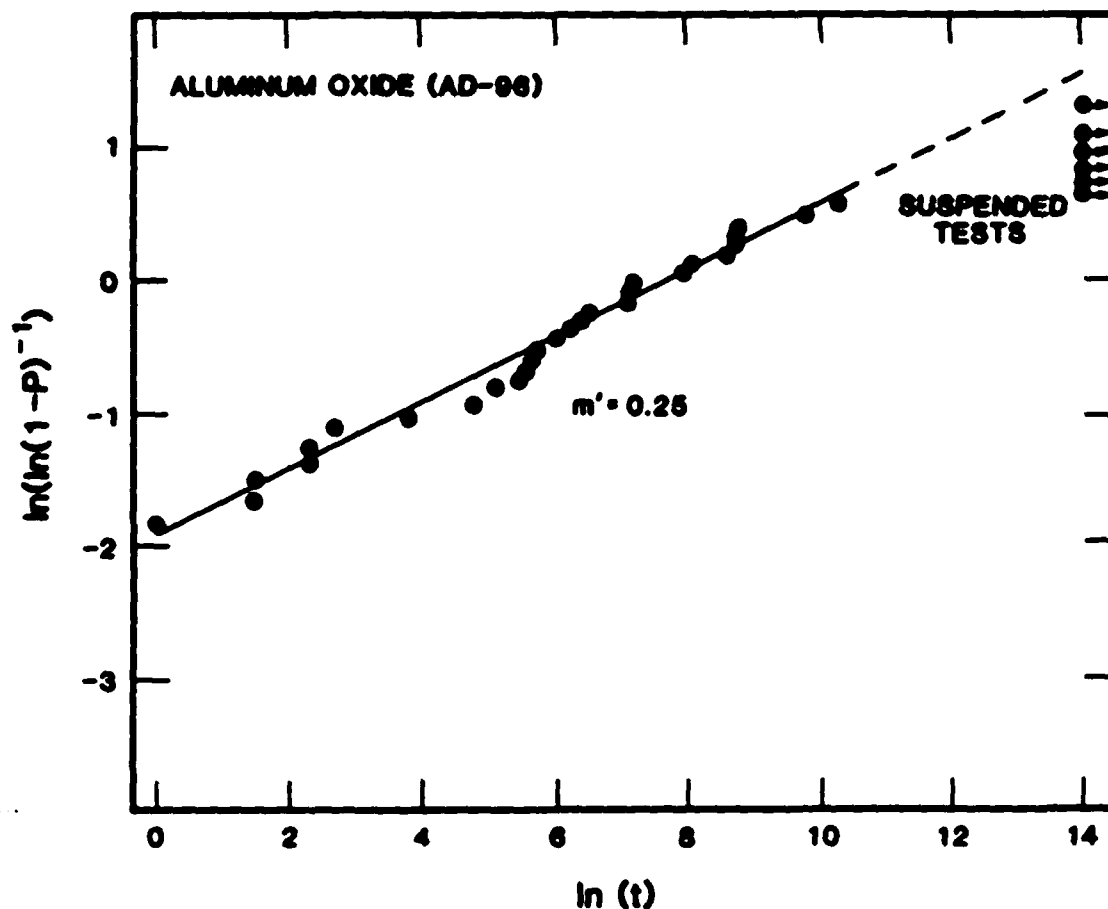
45. G. Grathwohl, in Proceedings of the Second International Conference on Creep and Fracture of Engineering Materials and Structures, Pineridge Press Ltd., pp. (1984) 565-77.
46. S.M. Wiederhorn and N.J. Tighe, J. Mat. Sci. 13 (1978) 1781.
47. A.G. Evans, J. Mat. Sci. and Eng., this issue.
48. E.R. Fuller, Jr., S.M. Wiederhorn, N.J. Tighe and L. Chuck, "Mechanical Behavior of Silicon Carbide at Elevated Temperatures" presented at Ceramics, Jerusalem '84, Jerusalem, Israel, December 10-20, 1984.
49. D.T. Fett and D. Munz, pp. 154-76 in Ref. 15.
50. J.R. Porter, W. Blumenthal and A.G. Evans, Acta Metall. 29 (1981) 1899.
51. C.H. Hseuh and A.G. Evans, Acta Metall. 29 (1981) 1907.
52. A.G. Evans and A.S. Rana, Acta Metall. 28 (1980) 129.
53. R.L. Tsai and R. Raj, Acta Metall. 30 (1982) 1043.
54. S.M. Johnson, B.J. Dalgleish, and A.G. Evans, J. Am. Ceram. Soc. 67 (1984) 759.
55. R. Kossowsky, D.G. Miller, and E.S. Diaz, J. Mat. Sci. 10 (1975) 983.
56. F.C. Monkman and N.J. Grant, Proc. ASTM, 56 (1956) 593.
57. S.M. Wiederhorn, B.J. Hockey, R.F. Krause, Jr. and K. Jakus, J. Mat. Sci., submitted for publication.
58. K. Jakus, S.M. Wiederhorn, B.J. Hockey and R.F. Krause, Jr., J. Mat. Sci., submitted for publication.
59. S.M. Wiederhorn and N.J. Tighe, J. Am. Ceram. Soc. 66 (1983) 884.
60. G.D. Quinn, Cer. Eng. and Sci. Proc. 3 (1982) 77.

Table I. A Comparison of measured flaw sizes and strengths with those predicted from acoustic surface wave measurements [29].

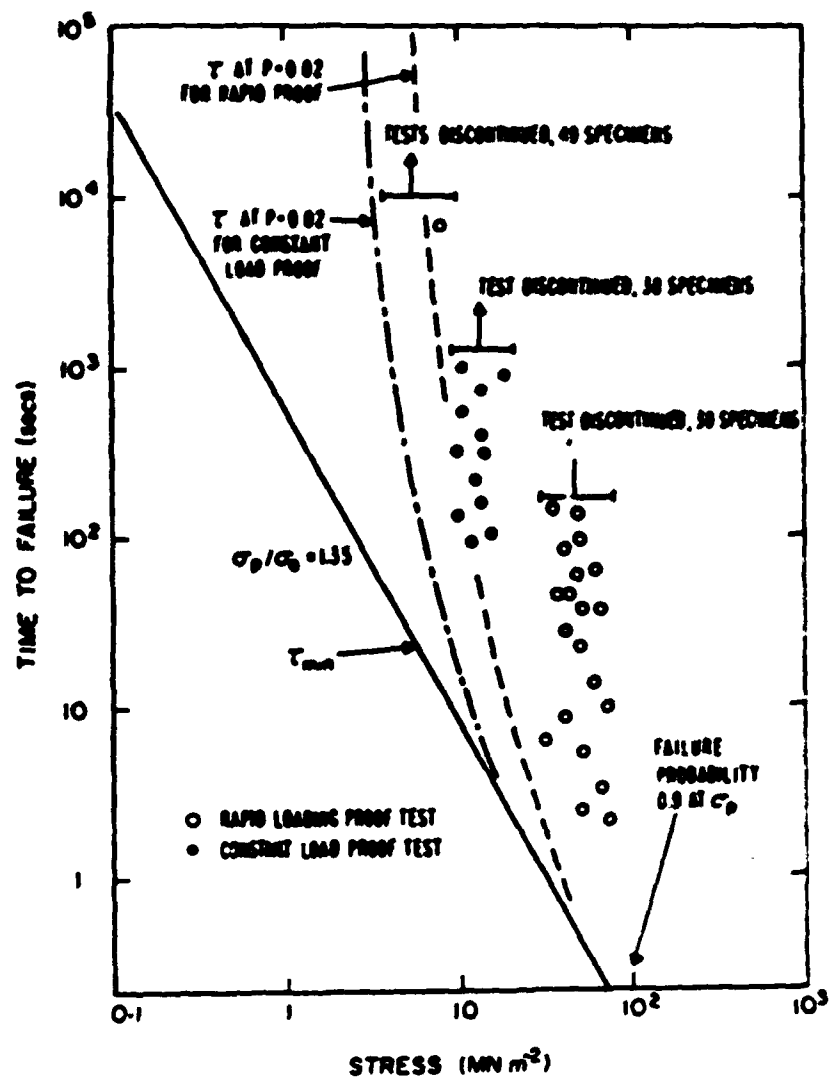
		Initial Flaw Sizes μm		Failure Strength MPa	
		Optical	Acoustic	Measured	Predicted
Indentation Cracks	1	115	97	238	240
	2	118	94	239	243
	3	118	96	242	242
	4	114	111	233	224
Machining Cracks	1	52	46	240	223
	2	35	42	306	233
Surface Scratch		42	36	239	251
Row of Indentations		140	98	140	152



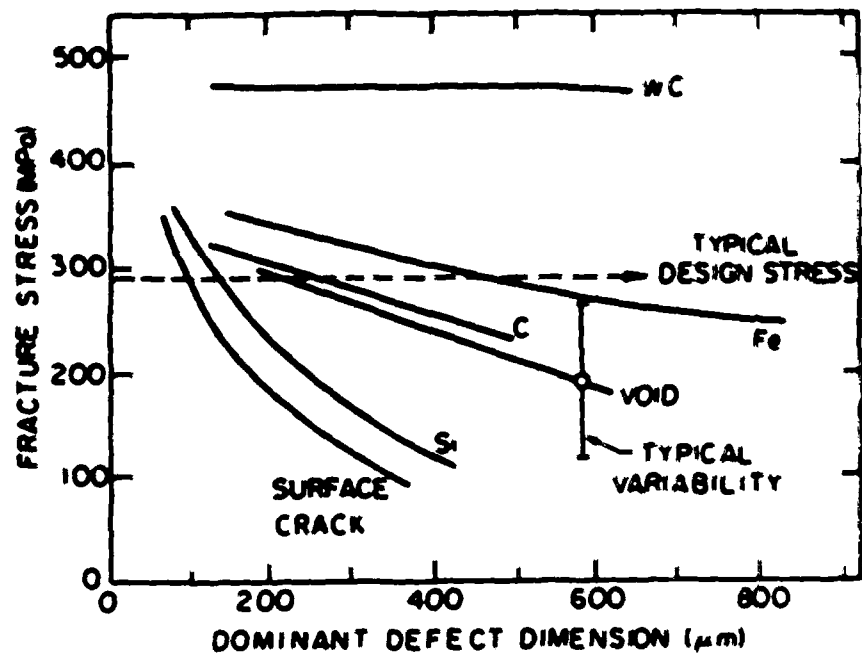
1. Bathtub curve: The hazard rate is plotted as a function of failure time. Note the high rate of failure both during the initial period of use and during wear out. The hazard rate can be defined in terms of the cumulative failure probability P : $h(t) = dP/dt/(1-P)$.



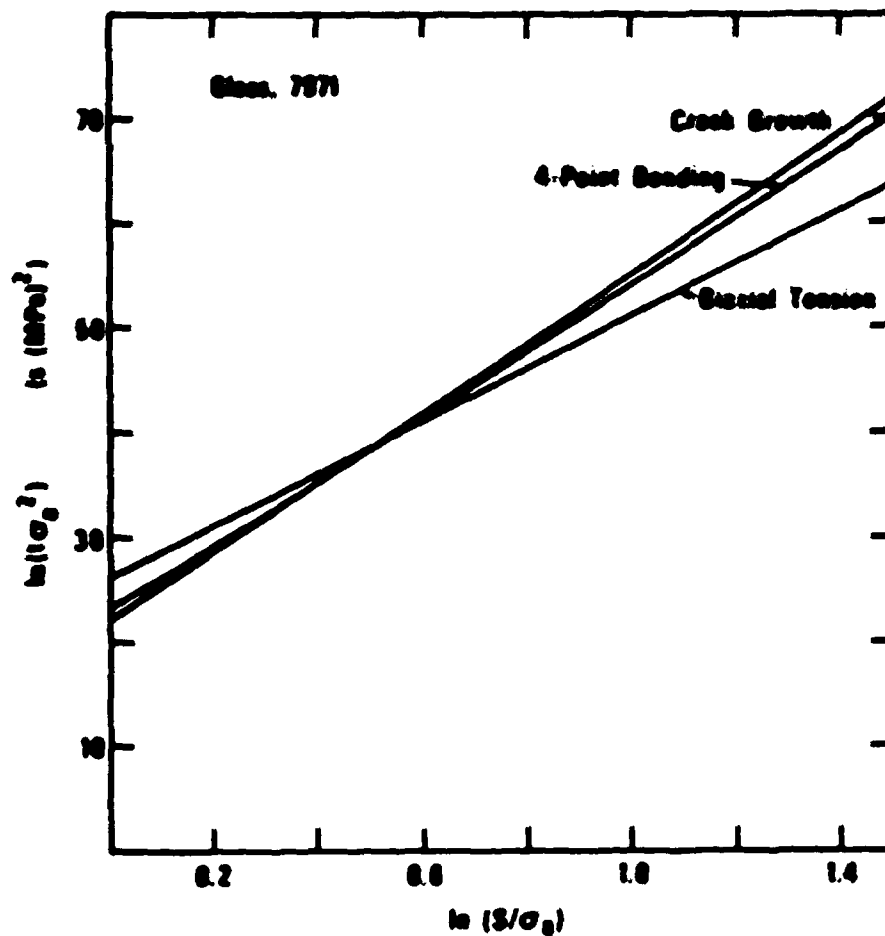
2. Weibull representation of failure times for a grade of vitreous bonded aluminum oxide subjected to a stress of 253 MPa in water. The figure was calculated from data originally reported in reference 15. The polycrystalline value of n determined from static fatigue measurements was 55 while the Weibull shape parameter, m , for this material was 9.8. The scaling parameter S_0 was -420 MPa. The calculated value of m' , 0.18, agrees favorably with the measured value, 0.25. The six tests suspended at 2 weeks all lie below the projected distribution suggesting a fatigue limit of $-(253/450) K_{IC} = 0.56 K_{IC}$.



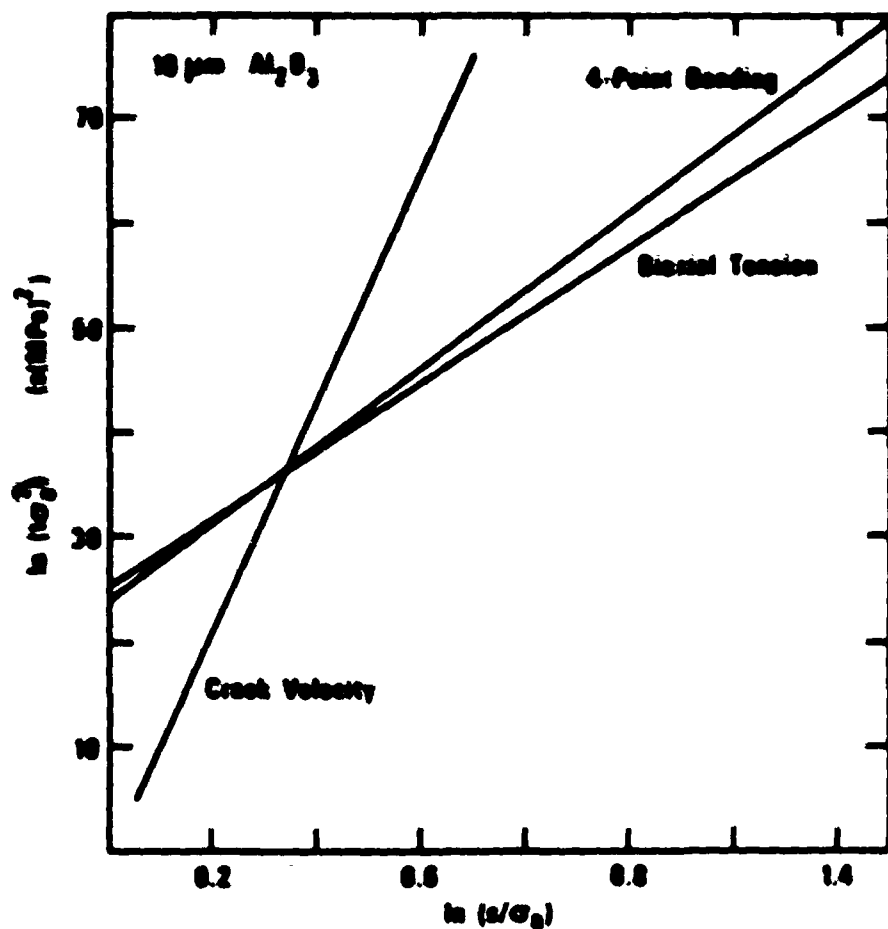
3. A comparison of failure times after proof-testing for surface ground specimens of soda-lime glass in water with the predicted minimum failure time for the system[16].



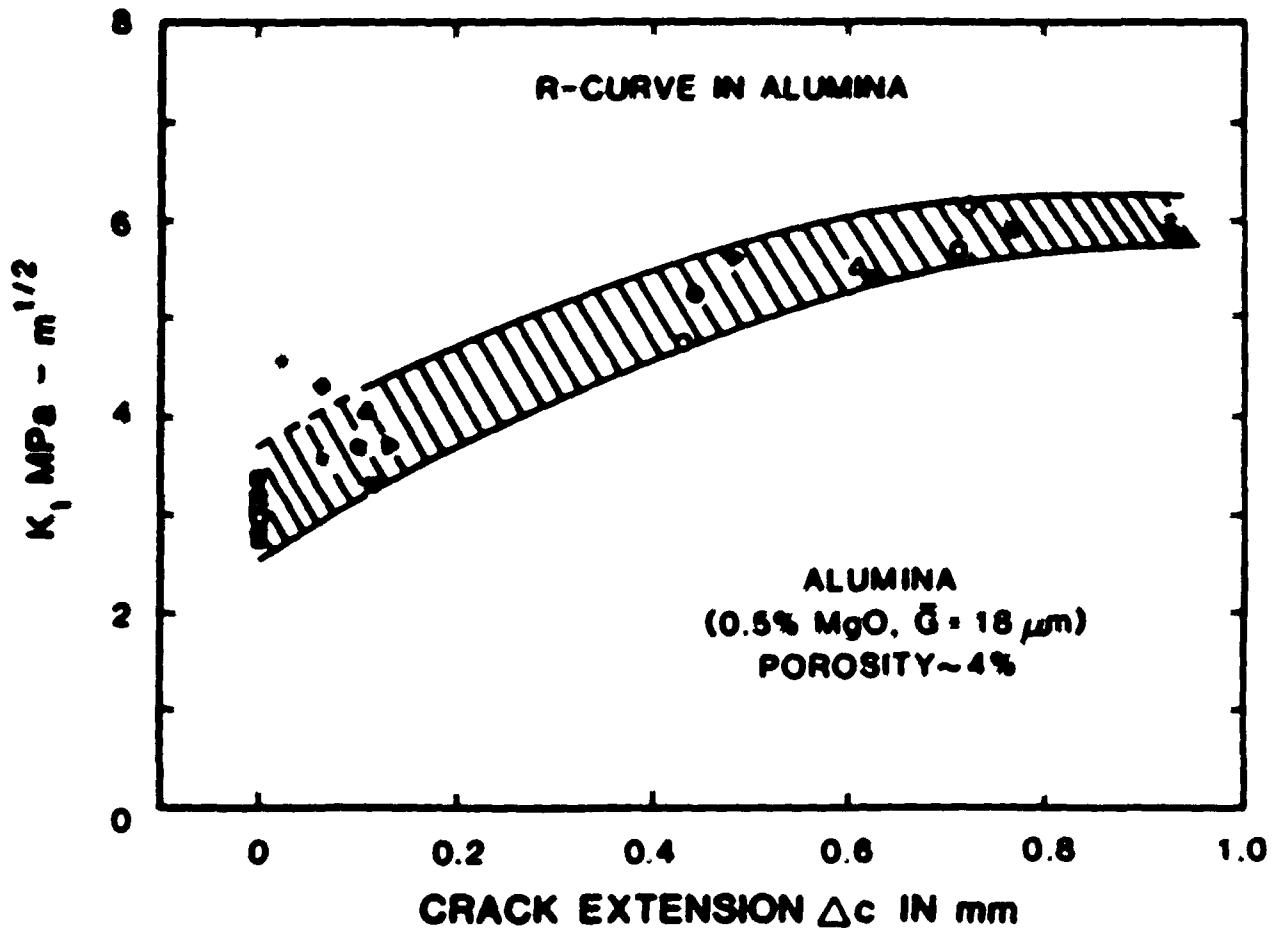
4. Effects of defect type on the fracture strength of hot-pressed, silicon nitride[29].



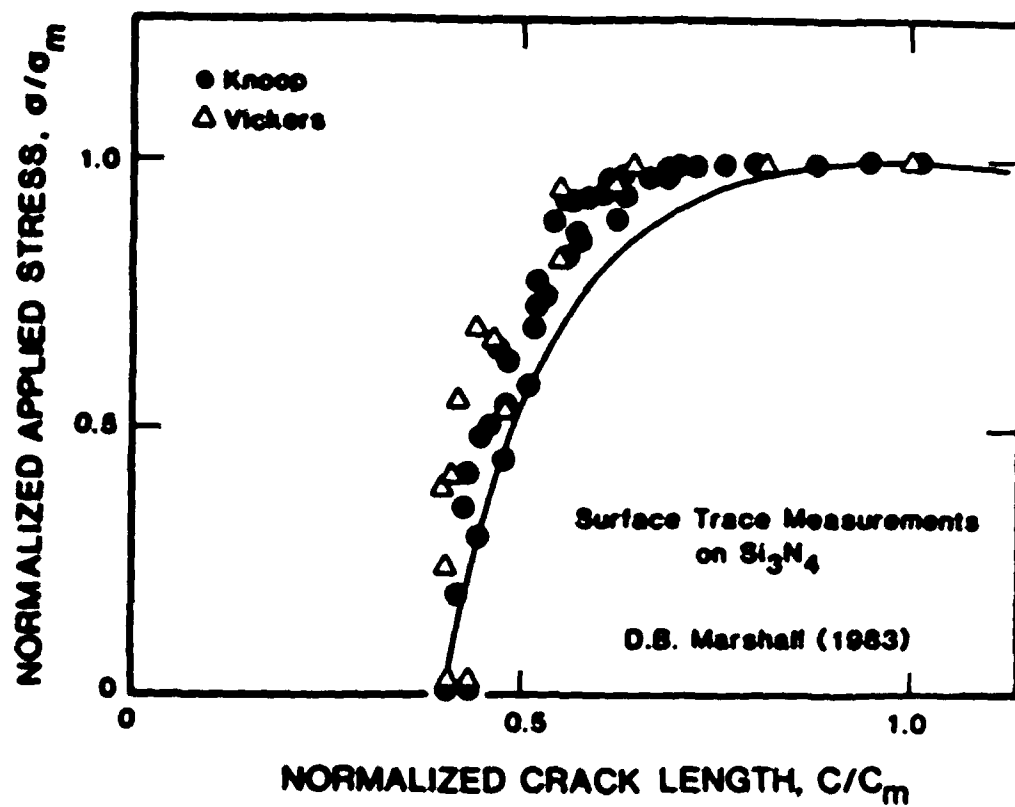
5. Diagram comparing lifetime predictions from fracture mechanics data and strength data for an ultra-low-expansion glass[31]. The slope of these curves is $(n-2)$ and the intercept is $\ln(9)$. The differences between these curves are not statistically significant.



6. Diagram comparing lifetime predictions from fracture mechanics data and strength data for aluminum oxide, with an 18 μm grain size. The constants n and d depend on the technique used to measure them[31].



7. R-curve for an aluminum oxide material, obtained from single-edge notched bend specimens in four point flexure. The rising resistance with crack extension is explained by multiple crack formation and by interference of the fracture surfaces[32].



9. η -curve resulting from the residual stress field associated with an indentation crack system that modifies the strength and crack growth relationship[30].

AD-A159 202

STRUCTURAL RELIABILITY OF BRITTLE MATERIALS AT HIGH
TEMPERATURES.. (U) NATIONAL BUREAU OF STANDARDS
GAITHERSBURG MD INORGANIC MATERI..

3/3

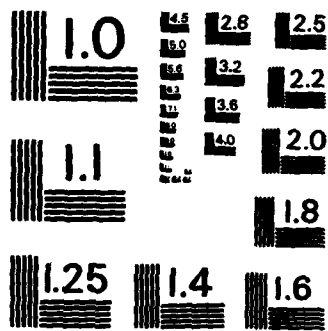
UNCLASSIFIED

S M WIEDERHORN ET AL. 31 DEC 84

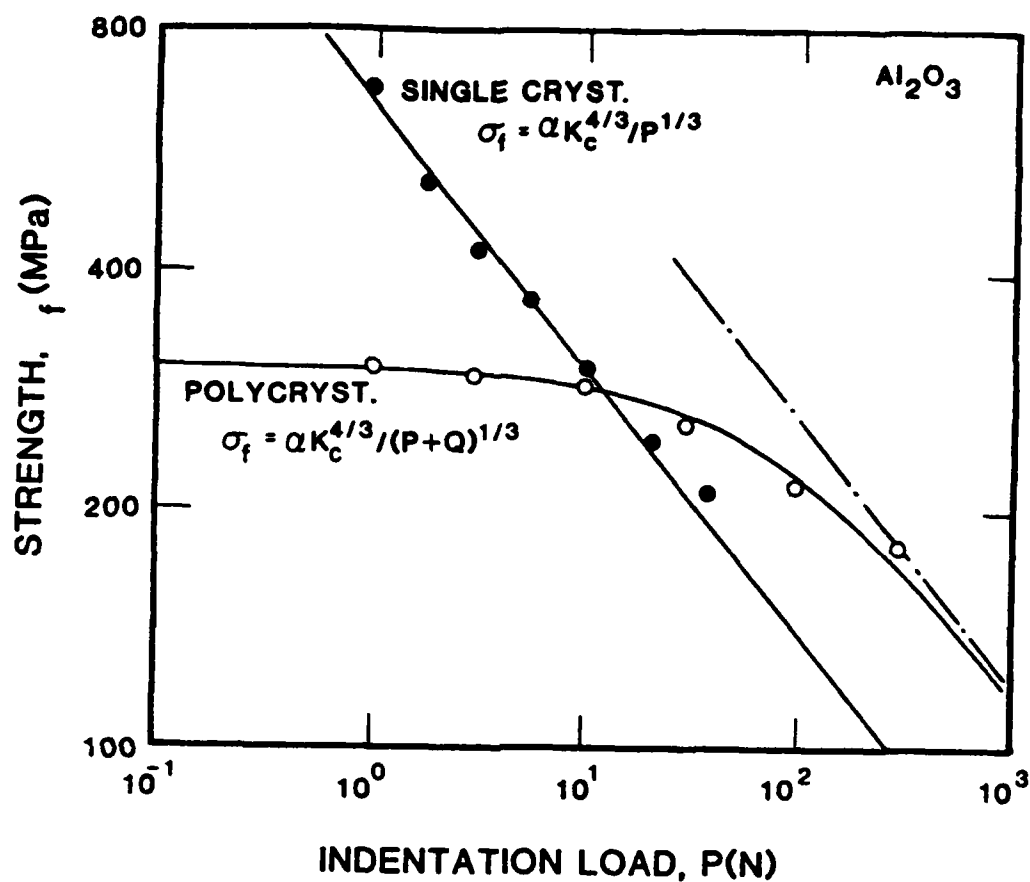
F/G 15/7

NL

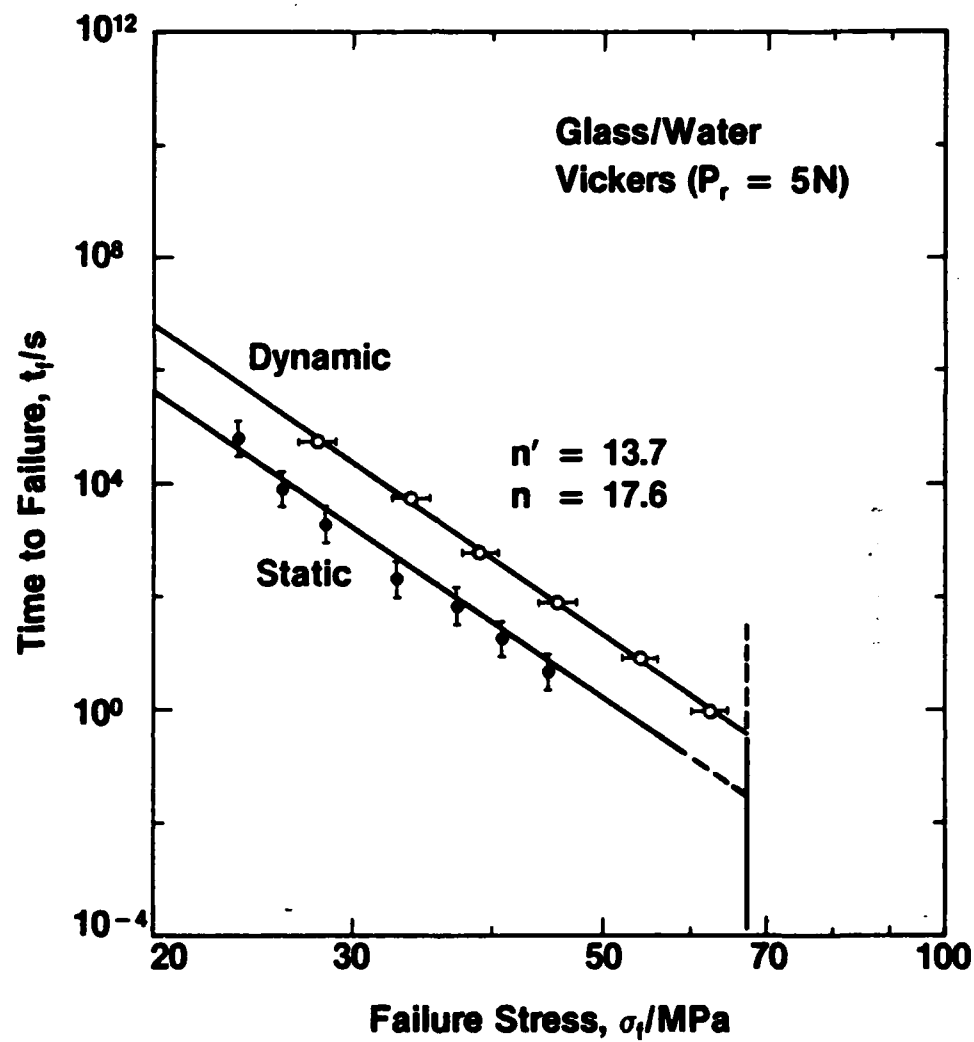




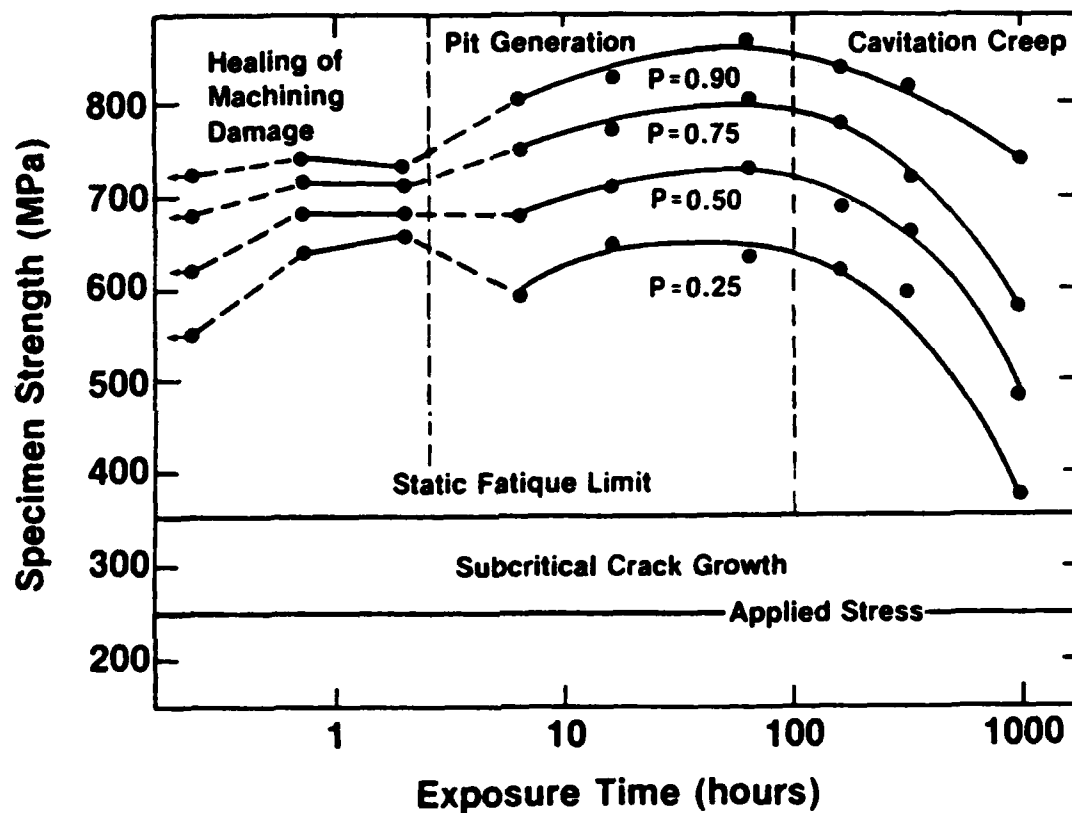
MICROCOPY RESOLUTION TEST CHART
NATIONAL BUREAU OF STANDARDS-1963-A



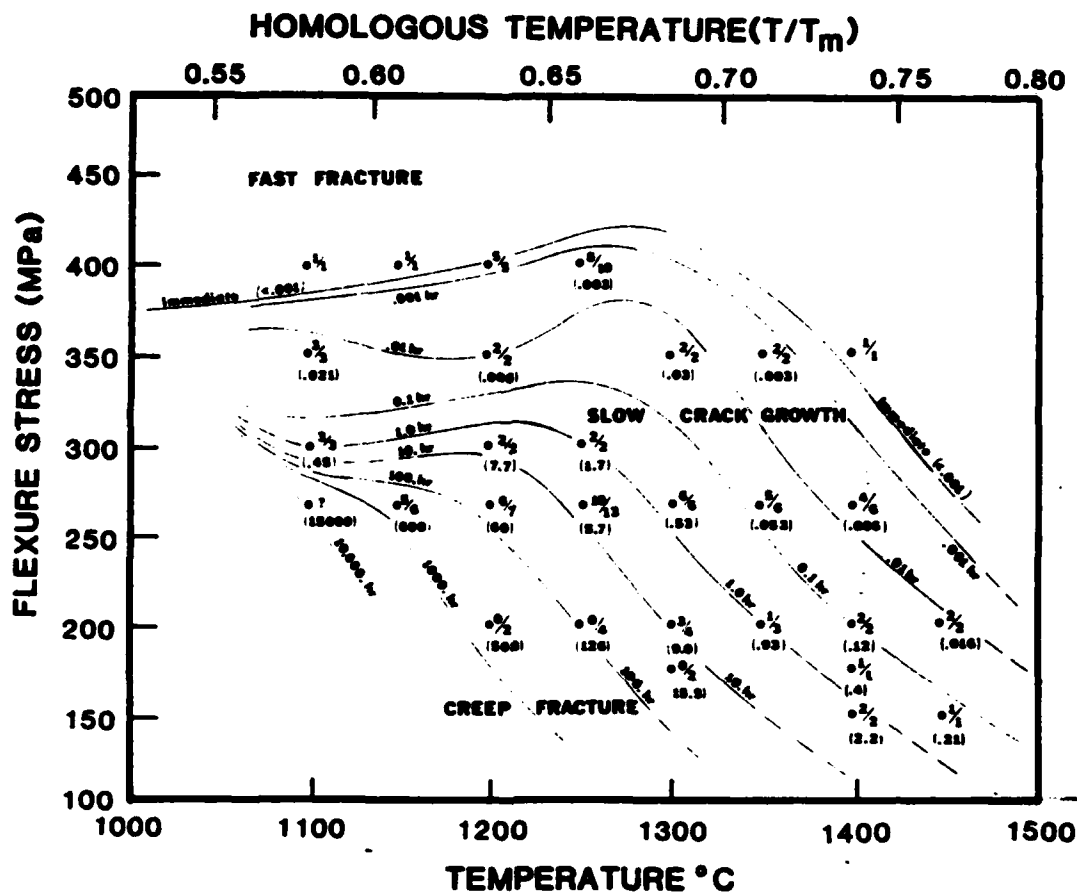
9. Strength of sapphire and aluminum oxide as a function of indentation load, P[39].



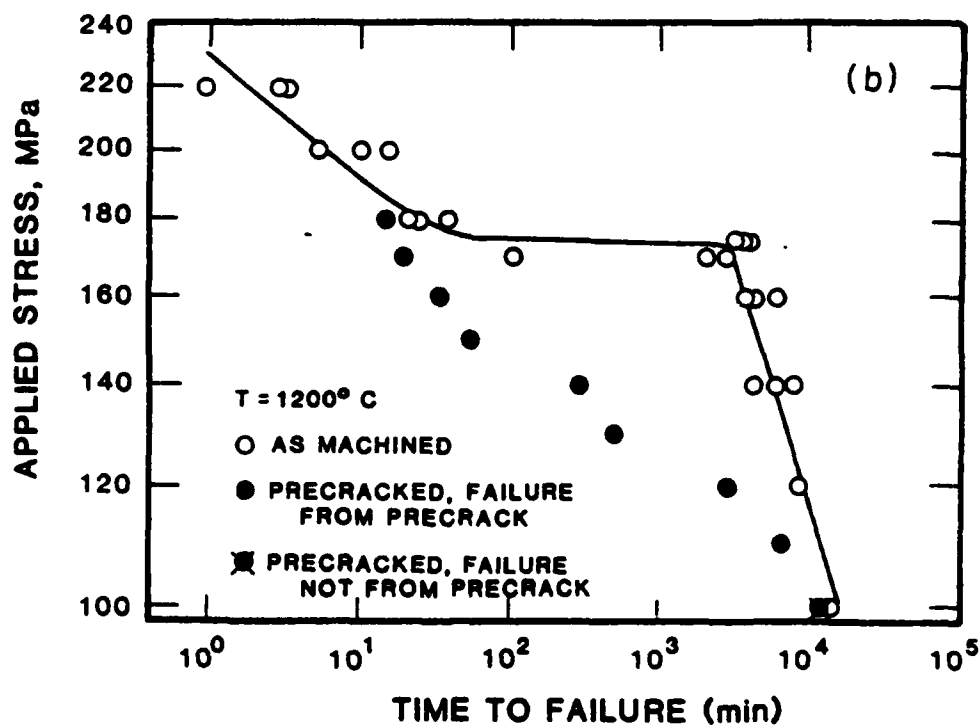
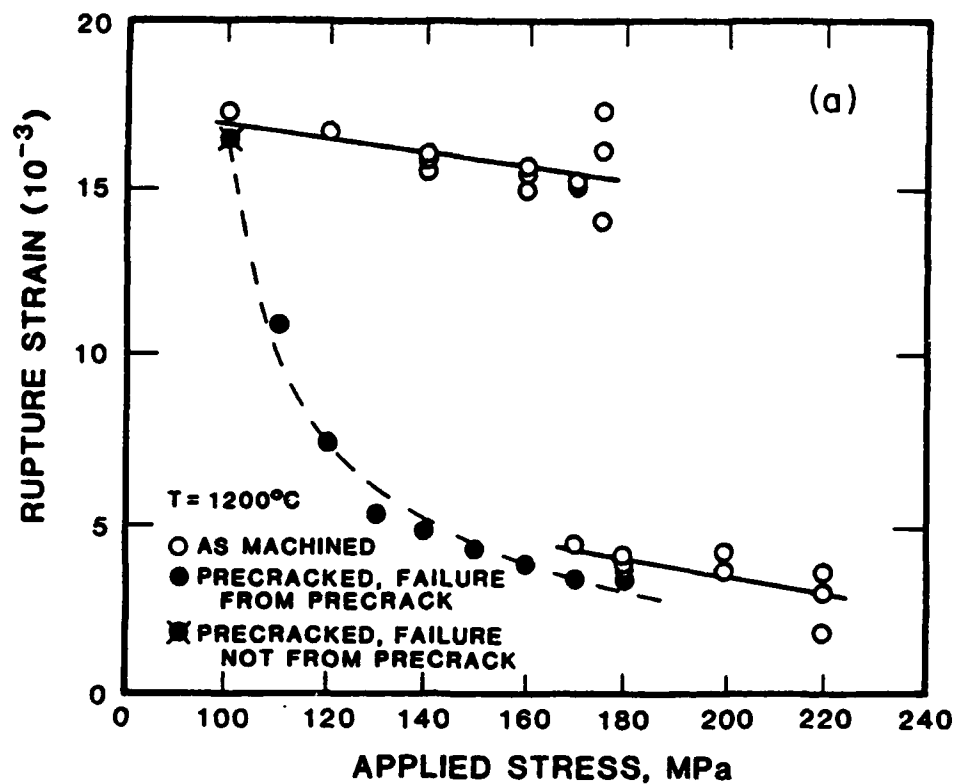
10. Plot comparing static and dynamic fatigue response for soda-lime glass in water using indentation flaws[36]. Error bars give the standard deviation of the measurement.



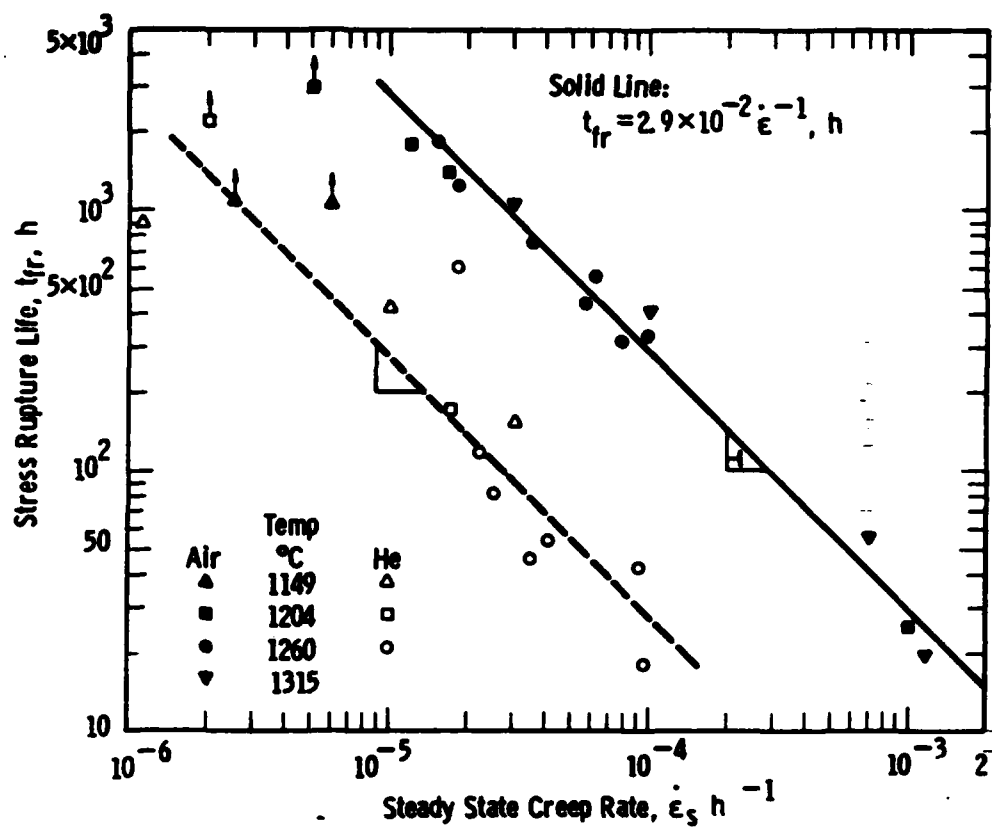
11. Reliability diagram for magnesia-doped, hot-pressed silicon nitride (NC-132). The diagram indicates four regimes of strength controlling for defects this material. Each line on the figure gives the cumulative probability level, P , for fracture at the exposure time specified by the abscissa[43].



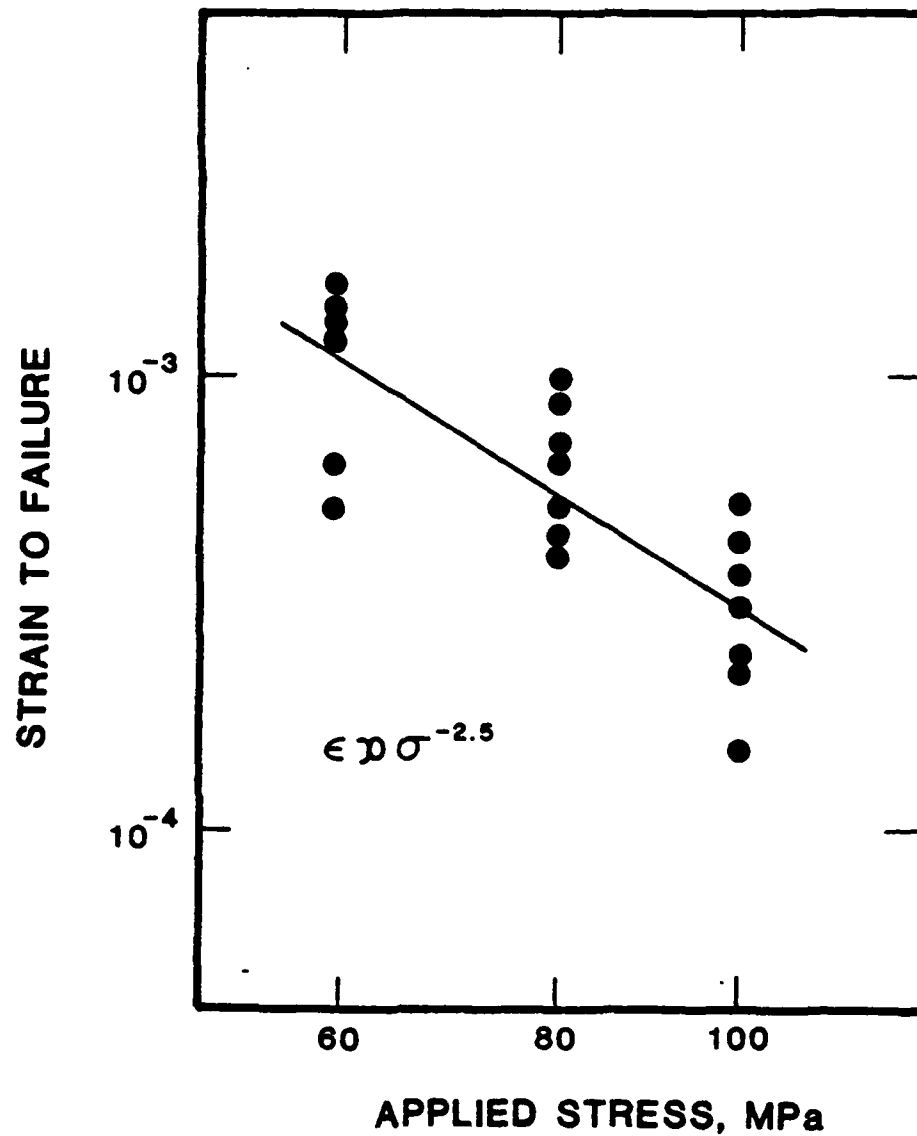
12. Fracture map for flexural stress rupture specimens of hot-pressed silicon nitride (NC-132) with 16N Knoop indentations. The lines represent constant times to failure. The fractions on the figure give the number of specimens that broke from the indentation divided by the total number tested. At any given temperature, subcritical crack growth dominated at high loads, creep-rupture at low loads[44].



13. High temperature (1200°C) creep rupture of hot-pressed, silicon nitride (Annawerk GmbH) specimens that were tested either in an as machined, or a pre-cracked state: (a) rupture strain as a function of applied stress; (b) rupture stress as a function of time to failure[45].



14. Dependence of creep rupture life on the creep rate of hot-pressed silicon nitride (HS-130)[55].



15. Strain to failure in vitreous bonded aluminum oxide (AD-96) tested in the temperature range 980 to 1100°C[57].

END

FILMED

11-85

DTIC